

1 JUICE-MAJIS Earth observations during the 2024 gravity assist: first analysis 2 and comparison with PRISMA data

3

4 Fabrizio Oliva^{1,*}, Emiliano D'Aversa¹, Alessandra Migliorini^{2,1}, Giuseppe Piccioni¹; François Poulet^{3,2};
5 Yves Langevin^{3,2}, Gianrico Filacchione¹, Mauro Ciarniello¹, Sébastien Rodriguez^{3,2}, Benoît
6 Seignovert^{5,3,2}, Alessandro Mura¹, Leigh N. Fletcher⁴, Sandrine Guerlet^{6,7}, Angelo Zinzi^{8,5,3}, Marco
7 Giardino^{8,5,3}, Ettore Lopinto^{8,5,3}, Giuseppe Sindoni^{8,5,3}, Christina Plainaki^{8,1,3}

8 *Correspondence: fabrizio.oliva@inaf.it

9

10 ¹Istituto di Astrofisica e Planetologia Spaziali (IAPS/INAF), Rome, Italy;

11 ² Osservatorio Astronomico di Padova (OAPd/INAF), Padova, Italy;

12 ³Institut d'Astrophysique Spatiale, CNRS/Université Paris-Saclay, 91405 Orsay Cedex, France .

13 ⁴School of Physics and Astronomy, University of Leicester, University Road, Leicester, LE1 7RH, UK.

14 ~~³Agenzia Spaziale Italiana (ASI), Rome, Italy. ¶~~

15 ⁵OSUNA, UAR-3281, LPG UMR-6112, CNRS, Nantes Université, Nantes, France.

16 ^{6,5}Laboratoire de Meteorologie Dynamique, LMD-IPSL, CNRS, Sorbonne Université, Université PSL,
17 Institut Polytechnique, Paris, France

18 ^{7,6}LIRA, Observatoire de Paris, Université PSL, CNRS, Sorbonne Université, Université Paris Cité,
19 92195 Meudon Cedex, France

20 ~~^{8,5,4}Agenzia Spaziale Italiana (ASI), Rome, Italy.~~

21 ~~School of Physics and Astronomy, University of Leicester, University Road, Leicester, LE1 7RH, UK. ¶~~

22

23 Abstract

24

25 The *JU*pter *IC*y moons *E*xplorer spacecraft (JUICE) performed a Lunar-Earth gravity assist
26 maneuver on 20th August 2024, during which the scientific instruments were turned on to
27 test their functionality. In the time of ~~At~~ the Earth flyby, the *Moon and Jupiter Imaging*
28 *Spectrometer* (MAJIS) on board JUICE acquired a sequence of multispectral images over
29 the Western Pacific Ocean at tropical latitudes. In parallel, an observing campaign was also
30 conducted by the Earth-orbiting PRISMA imaging spectrometer, with the purpose of
31 validating MAJIS spectral observations with independent measurements of the same kind.

32 These two datasets are here exploited to investigate and compare several atmospheric and
33 cloud properties, including composition, temperatures, and atmospheric gravity waves. In the
34 MAJIS spectral range, covering the 500-5560 nm wavelengths, we identified major and
35 minor atmospheric gases, including O₂, H₂O, CO₂, O₃, CH₄, N₂O. Since MAJIS observations
36 mostly covered diffuse cloudiness over the ocean, our analysis mainly focused on the
37 discrimination of clouds' properties and altitudes. We verified that ice particles are
38 widespread in the data, allowing for an investigation of their properties (e.g. crystallinity)
39 through different spectral signatures. The only land features identified in MAJIS data are not
40 observed in daylight, hence only a thermal emission analysis is presented. Finally, the
41 coverage of the 4300 nm CO₂ band enables the identification of high altitude structures,
42 revealing the presence of several atmospheric wave packets, likely induced by convective
43 events, or lightning strikes known to have occurred at the time of the flyby. The present
44 analysis demonstrates how MAJIS data can contribute to the scientific investigation of an
45 atmospheric environment, and provide the first benchmark in the analysis of water ice,
46 whose characterization in the Jovian system will be of primary importance for the JUICE
47 mission.

48

49 1. Introduction

50

51 On the 20th of August 2024 the JUICE spacecraft performed a first *Lunar-Earth Gravity*
52 *Assist* (LEGA) and is now headed for a second *Earth Gravity Assist* (EGA) happening in
53 *September 2026*. The JUICE mission is conceived for the investigation of Jupiter's icy
54 satellites' surfaces and interiors, but also for the characterization of the giant planet's
55 atmosphere and magnetosphere. These scientific objectives will be achieved thanks to a
56 payload consisting of several remote sensing and in-situ instruments, including an altimeter,
57 a magnetometer, a gravity experiment, a radio instrument, neutral/energetic particles and
58 plasma detectors and an ultraviolet spectrograph. Moreover, the visible-thermal infrared
59 spectral range will be investigated by a visible camera (JANUS) and by the *Moons and*
60 *Jupiter Imaging Spectrometer* (MAJIS, Poulet et al., 2024a), which in particular will allow the
61 spectroscopic investigation of Jupiter's atmosphere, moons and rings system. On the 20th
62 of August 2024 the JUICE spacecraft performed a first *Lunar-Earth Gravity Assist* (LEGA)
63 and is now headed for a second *Earth Gravity Assist* (EGA) happening in September 2026.
64 In this study we will focus on 2024 the *Earth Gravity Assist* (EGA) data acquired by
65 MAJIS alone which, along with JANUS (see Hueso et al., this issue), during which the *Moons*
66 *and Jupiter Imaging Spectrometer* (MAJIS, Poulet et al., 2024a) was turned on, providing its
67 very first observations of a planetary target (for a general overview of the flyby refer to
68 given in Poulet et al., (this issue), while valuable information about MAJIS operations,
69 functioning and performances is given in Langevin et al. and Seignovert et al., (this issue).
70 During the flyby, different Earth observing spectrometers were coordinated to provide
71 spatially and temporally comparable observations (Poulet et al., this issue). A companion
72 paper by Guerlet et al. (this issue) is focused on MAJIS IR channel's data comparison with
73 co-located acquisitions by the IASI thermal Fourier spectrometer onboard the
74 EUMETSAT/Metop satellite. Among these, we exploit PRISMA spectrometer data as
75 a proxy to compare with MAJIS VISNIR channel observations (Section 2.1), even if the
76 different times and regions of acquisition prevent a direct comparison of the scans (see
77 Section 2). PRISMA (Section 2.2) is a technology demonstrator mission completely funded
78 by the Italian Space Agency (ASI) and devoted to the qualification of a
79 panchromatic/hyperspectral technology for monitoring the Earth at visual-near infrared
80 wavelengths at moderate spectral resolution and high spatial resolution (Pignatti et al.,
81 2013).

82 JUICE flew over Western Pacific Ocean at tropical latitudes, moving approximately from
83 Sumatra to Hawaii islands and spanning local times from about 03:00 to 10:30 (see Table
84 1). The majority of these measurements took place over the ocean, allowing a broad
85 characterization of atmospheric gaseous composition and structure (Section 2.3.2). Land
86 features are only marginally detected in a couple of observations mainly in the thermal range
87 (Section 4.4).

88 Given the widespread presence of clouds and the early local times of acquisition (Section 2),
89 ice is observed in almost all MAJIS scans (Section 4.1), allowing benchmarking of the
90 spectrometer's response to this observable in view of Jupiter's icy satellites investigation.
91 Also atmospheric waves, whose role is fundamental in regulating the middle-atmosphere
92 circulation (e.g. Hamilton, 1996; Fritts and Alexander, 2003), are detected in many MAJIS
93 observations. Such phenomena are either given their linked with orography (Queney 1948;
94 Kim et al. 2003) or with the occurrence of thunderstorms (Taylor and Hapgood, 1988; Dewan

95 et al. 1998). Given that MAJIS EGA observations mainly targeted the ocean, we investigate
96 their waves' connection dependence with strong convective events or lightning strikes
97 (Section 4.4).

98 The manuscript is arranged in sections describing the data (Section 2), the methods for their
99 investigation (Section 3) and the obtained results (Section 4). Such a wide ensemble of
100 atmospheric observable features is finally discussed in the context of Jupiter science in
101 Section 5.

102

103 2. Observations

104

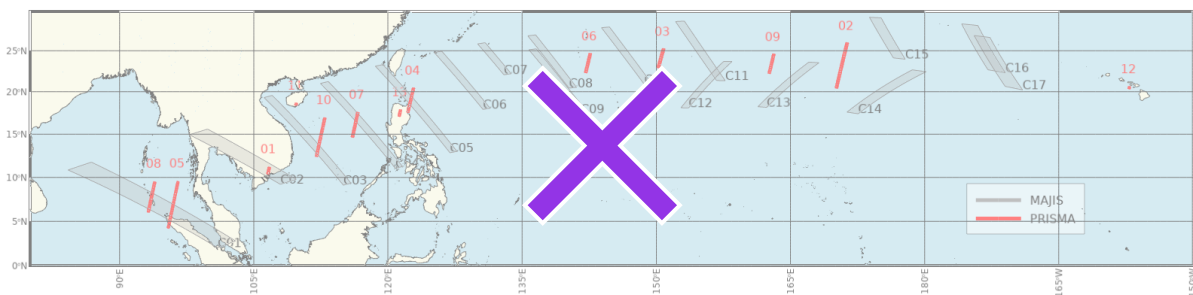
105 2.1. MAJIS EGA Data

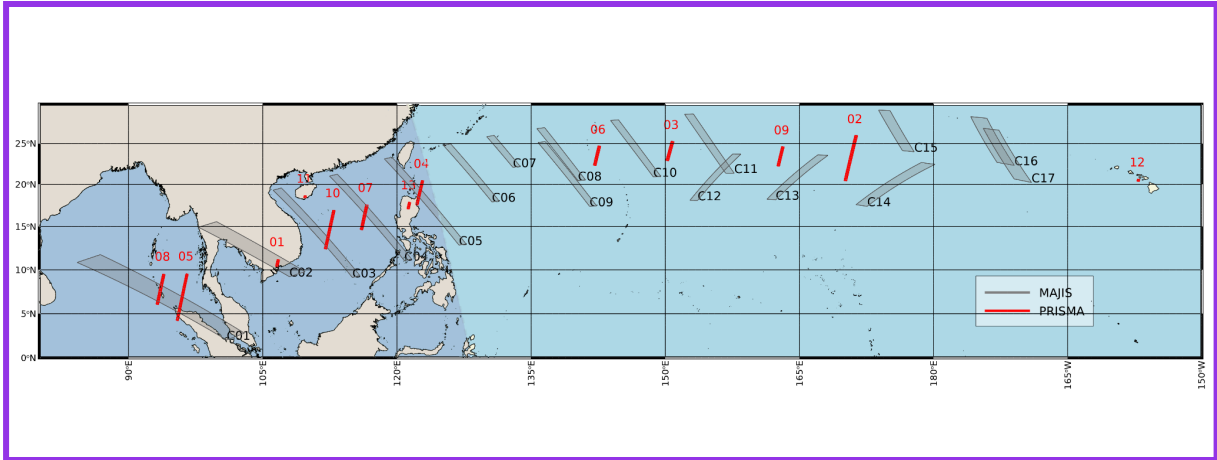
106

107 MAJIS is a dispersion grating imaging spectrometer operating between 500 and 5560 nm by
108 means of two spectral channels (Poulet et al., 2024a). The first channel (VISNIR, 500–2350
109 nm) is characterized by nominal spectral resolution and sampling of 2.9-4.6 nm and 3.5-3.8
110 nm/band respectively, while the second (IR, 2270–5560 nm) works with a spectral resolution
111 of 5.5-7.0 nm and a sampling of 5.9-6.9 nm/band. The nominal instrument's instantaneous
112 field of view (IFOV) is 150 μ rad/pixel. MAJIS concept has been optimized for the
113 characterization of the surface and near-surface environment of Jupiter's icy moons (Poulet
114 et al., 2024a), as well as for the investigation of Jupiter's atmosphere (Fletcher et al., 2023).
115 Detailed descriptions of the instrument functioning, operations and calibration are given in
116 Haffoud et al. (2024), Langevin et al. (2024), Poulet et al. (2024b), Filacchione et al. (2024),
117 Rodriguez et al. (2024), Vincendon et al. (2024), and Stefani et al. (2025). Scene geometry is
118 reconstructed via the SPICE-NAIF toolkit (Acton, 1996; Acton et al., 2018) and kernels
119 provided by ESA ("JUICE SPICE Kernel Dataset," 2019).

120 Figure 1 and Table 1 summarize footprint locations and main basic properties of the 17
121 MAJIS EGA data investigated in this work (see Poulet et al., this issue, for further
122 instrumental parameters). Two additional cubes, targeted off-limb for calibration purposes
123 (Poulet et al., this issue), are not considered here. Each MAJIS acquisition consists of
124 hyperspectral cubes (i.e. 2D spatial frames with a third spectral dimension) collected as
125 pushbroom spectral scans via internal mirror rotation, with different widths and lengths.

126





128

129 **Figure 1:** Geographical coverage of the investigated observations, MAJIS in grey color,
 130 PRISMA in red color. The darker area westward of the Philippines indicates the nightside at
 131 the time of the terminator crossing of MAJIS observations (2024-Aug-20 21:30 UTC). Instead
 132 all PRISMA footprints are in daylight, at local time ~10:30. (Coastlines are data from
 133 OpenStreetMap, available under the Open Database License).

134

135 The first 4 cubes (C1 to C4) pointed to the Earth surface at nighttime and contain a
 136 significant signal only in the thermal part of the spectrum ($\lambda > 3000$ nm). The only exception
 137 is C1, where a lightning emission is identifiable at visible wavelengths (D’Aversa et al., this
 138 issue). C5 is straddling the terminator and is the first cube containing information on the
 139 dayside ocean and clouds. Some coastlines are identifiable in C4 and C5 at thermal
 140 wavelengths, as it will be discussed in Section 4.4. All the subsequent cubes (C6 to C17) are
 141 acquired in daylight and hence the full spectrum can be investigated, even if they only cover
 142 the ocean surface mostly under cloudy/stormy conditions.

143 Cubes from C11, C12 and C13 on have been acquired with longer integration times, with the
 144 purpose of testing the instrument response. This leads to signal saturation in many regions
 145 (especially at visual wavelengths over clouds, see Section 2.3.1), that have been removed
 146 from our analysis. The spatial resolution in this dataset is quite stable (about 1.4 km per
 147 pixel, slightly affected by motion smearing) and is suited for the investigation of both
 148 homogeneous and localized cloud structures. On the other hand, the IFOV is affected by
 149 unresolved cloudiness (likely widespread) which dilutes the low reflectivity of deep water
 150 hence preventing the acquisition of clear-sky ocean (Section 2.3.1, Figure 2).

151

152 **Table 1:** MAJIS observing parameters during EGA. Phase angle is always close to 90° .

	ID	target	incidence angle ($^\circ$)	emission angle ($^\circ$)	local time (h)	instantaneous resolution (km/px)
C1	20240820212509	surface night	115-130	28-42	03:00 – 04:18	1.80
C2	20240820212818	surface night	106-116	17-27	03:54 – 04:48	1.55
C3	20240820213029	surface night	100-106	12-19	04:30 – 05:12	1.50
C4	20240820213208	surface night	93-100	6-13	05:00 – 05:36	1.45
C5	20240820213347	surface terminator	87-93	0-11	05:24 – 06:00	1.40
C6	20240820213530	surface day	82-87	6-11	05:54 – 06:18	1.35

C7	20240820213644	surface day	79-82	11-14	06:12 – 06:30	1.30
C8	20240820213731	surface day	72-77	17-20	06:36 – 07:00	1.30
C9	20240820213840	surface day	71-76	14-20	06:36 – 07:06	1.30
C10	20240820214003	surface day	64-69	24-27	07:12 – 07:36	1.30
C11	20240820214117	surface day	56-61	32-37	07:48 – 08:12	1.30
C12	20240820214231	surface day	55-60	29-34	07:48 – 08:12	1.25
C13	20240820214350	surface day	46-52	39-45	08:24 – 08:54	1.30
C14	20240820214509	surface day	34-42	50-58	09:06 – 09:42	1.35
C15	20240820214628	surface day	36-41	49-53	09:18 – 09:36	1.30
C16	20240820214720	surface day	26-32	60-65	10:00 – 10:18	1.40
C17	20240820214813	surface day	23-31	60-66	10:06 – 10:30	1.40

153

154

2.2. PRISMA data

155

156 An observing campaign coordinated to the EGA was conducted by the mission PRISMA
157 (PRecursore IperSpettrale della Missione Applicativa), managed by the Italian Space
158 Agency. The mission hosts a visible and near-infrared imaging spectrometer, covering a
159 range (400-2500 nm) compatible with the MAJIS-VISNIR channel but having a coarser
160 spectral resolution (~12 nm) in turn compensated by a higher spatial resolution (~30
161 m/pixel). Details about the instrument and the mission can be found in Pignatti et al. (2013),
162 while mission characteristics, access, products, calibration, geometry navigation and data
163 policy are fully described in Lopinto et al. (2021).

164 PRISMA sequences (13 in total, red rectangles in Figure 1, main parameters summarized in
165 Table 2) consist of a variable number of 30 x 30 km hyperspectral cubes, each composed of
166 1000 x 1000 spatial pixels. Due to the PRISMA orbit (Sun-Synchronous-Low-Earth-Orbit),
167 observations are acquired at a fixed solar local time (~10:30), making it impossible to
168 achieve spatial/temporal coincidence with MAJIS ones (see next section).

169

170 Table 2: PRISMA observations acquired in coordination with JUICE.

PRISMA sequence	Num cubes	Start UTC	Solar zenith angle (°)	Emission angle (°)	Cloud coverage (%)	Δt (h) (PRISMA-MAJIS)
01	3	2024-08-17 03:34	20.3	14.6	14	-90.9
02	21	2024-08-18 23:13	23.4	17.1	8	-46.45
03	9	2024-08-19 00:50	20.6	20.7	9	-44.83
04	11	2024-08-19 02:22	21.4	4.2	100	-43.19
05	21	2024-08-19 04:08	22.7	1.2	73	-41.52
06	9	2024-08-20 01:07	23.6	16.6	2	-20.55

07	11	2024-08-20 02:46	22.5	18.4	18	-18.90
08	13	2024-08-20 04:25	21.0	16.0	98	-17.24
09	9	2024-08-20 23:46	23.2	12.3	1	2.11
10	17	2024-08-21 03:03	22.0	12.0	5	5.39
11	3	2024-08-22 03:19	21.7	5.6	20	29.66
12	1	2024-08-22 21:07	22.2	7.6	16	47.45
13	3	2024-08-25 02:32	21.6	4.3	7	100.88

171

172

2.3. General comparison overview

173

174 Both MAJIS and PRISMA acquired multispectral data covering the same kinds of structures,
 175 offering a useful benchmark for checking MAJIS capabilities in detecting and analyzing
 176 specific features of scientific interest. In the following section we investigate how the spectral
 177 signatures of the main atmospheric gases and of clouds are affected by the different
 178 spatial/spectral resolutions and observing conditions. When reflectances are discussed,
 179 they are obtained for both instruments as I/F , where I is the observed by converting spectral
 180 radiances and F is by using the Kurucz solar spectral radiance spectrum (Kurucz et al., 1984;
 181 Kurucz, 1995 “newkur”) available in the MODTRAN radiative transfer package (Berk et al.,
 182 2014) and available at the website
 183 <https://earth.gsfc.nasa.gov/climate/projects/solar-irradiance/data> (accessed February, 10,
 184 2026). From now, for readability, in the following we will refer to spectral radiance simply as
 185 radiance.

186

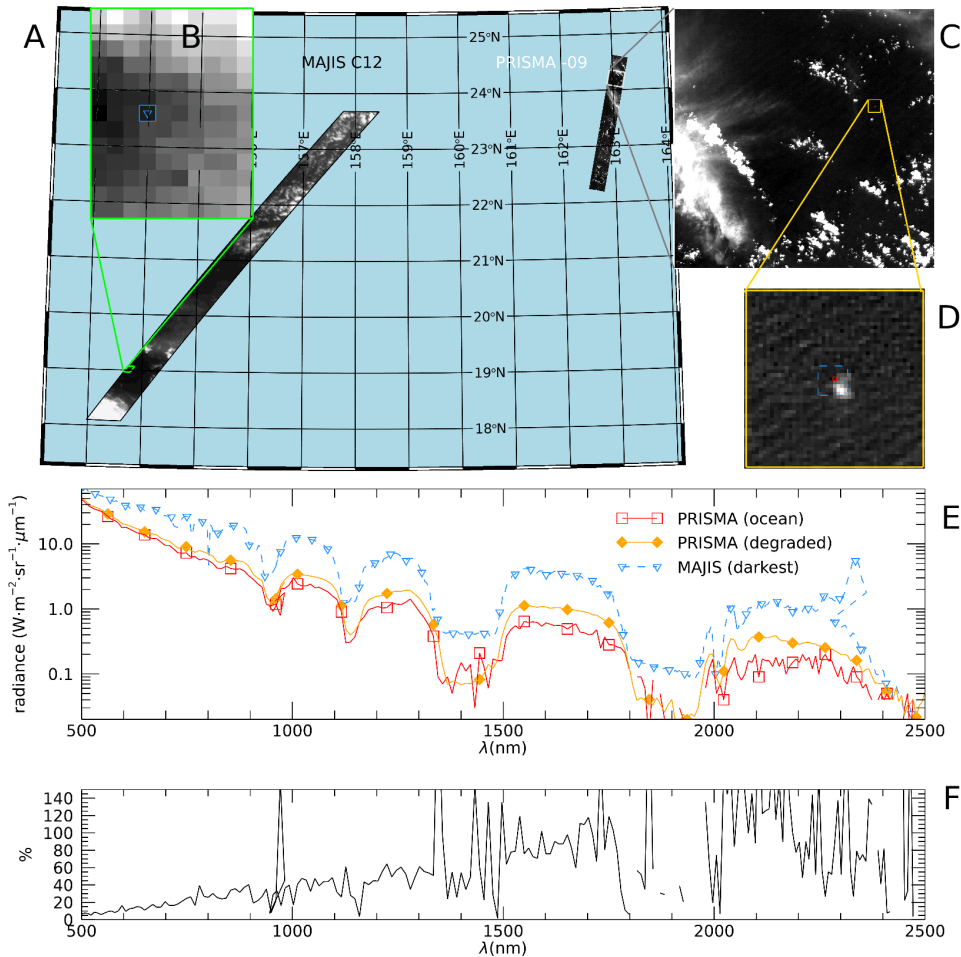
187

2.3.1. Ocean/clouds spectra first comparison

188

189 Figure 2 shows the two closest PRISMA and MAJIS cubes that are closest from both a
 190 spatial and temporal point of view (~550 km and ~2 h apart), covering open ocean areas
 191 overlaid by a different amount of clouds. In this framework, the most robust spectral radiance
 192 comparison should consider ocean cloud-free spectra, expected to be quite stable in space
 193 and time and very dark at visual wavelengths (given the very low ocean albedo, ~4%).
 194 However, the comparison between the two instruments (Figure 2E) highlights that the
 195 darkest MAJIS signals are still brighter than those from PRISMA, possibly suggesting
 196 enhanced cloud/aerosol content. Indeed, the higher spatial resolution of PRISMA data
 197 reveals a number of small-scale structures, likely unresolved by MAJIS, yet affecting its
 198 signal. For instance, the small bright feature imaged by PRISMA in Figure 2D, covering only
 199 a portion of a MAJIS pixel footprint, may induce spectral variations of the ocean spectrum up
 200 to 50% (Figure 2F) once observed at the MAJIS resolution scale.

201



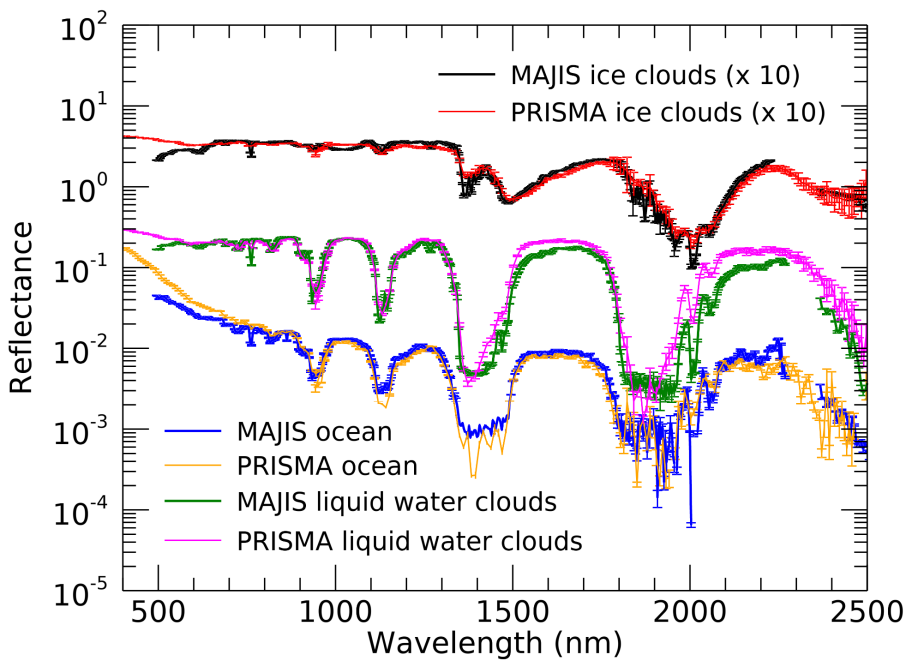
202

203 **Figure 2:** **A)** MAJIS observation C12 and PRISMA sequence P09 (~2h apart) shown at 875
 204 nm in an equal-area projection. **B)** Blow-up of the darkest area in the MAJIS image,
 205 highlighting individual pixels' size. **C)** The second cube of the PRISMA sequence is shown in
 206 its full extension of 1000x1000 pixels. **D)** Blow-up of an area of PRISMA data encompassing
 207 a small bright cloud. The blue dashed box shows the approximate size of a MAJIS pixel. **E)**
 208 Single-pixel spectra from the darkest pixels of MAJIS (blue color, triangle symbol in B) and
 209 PRISMA (red curve, red square in D). The orange curve represents a PRISMA spectrum
 210 degraded to MAJIS spatial resolution (average inside the blue box of panel D). The MAJIS
 211 spectrum is multiplied by the ratio of solar incidence cosines (=1.82) to achieve a radiance
 212 level comparable with PRISMA. **F)** Spectral effect of the spatial spectral degradation in
 213 PRISMA data, shown as the relative difference between the red and orange curves of panel
 214 E.

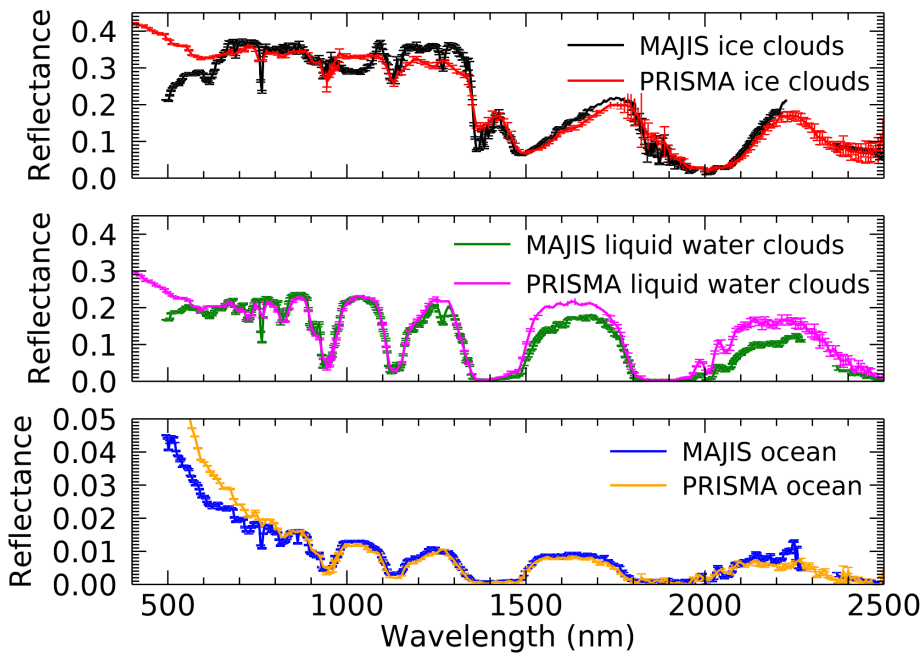
215

216 Most of the spectral variability in both datasets is driven by changes in the H₂O absorption
 217 bands. Besides the general low reflectivity, ocean spectra are characterized by the presence
 218 of large and often saturated water absorption bands. On the other hand, H₂O clouds (either
 219 composed of liquid droplets, ice crystals or a mixture) can easily be identified through RGB
 220 imaging from both datasets due to their bright appearance (Section 3.1). H₂O bands are less
 221 saturated over clouds, where light scattering prevents photons from reaching the
 222 underneath, more absorbing, atmospheric layers. Ice clouds' discrimination is basically
 223 driven by the spectral shift of absorption bands between solid and liquid H₂O phase (Section

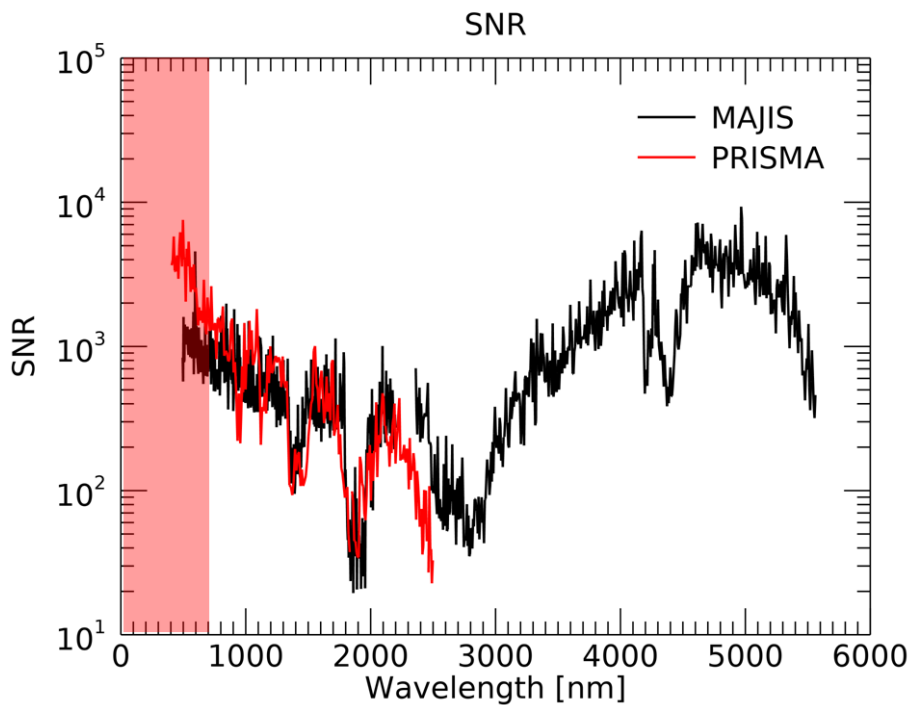
224 3.1). The comparison of spectral signatures related to the ocean and clouds (main spectral
 225 endmembers for both instruments) is shown in Figure 3A-B in log and linear scale
 226 respectively (refer to Figures 4 and 5 for the gaseous features identification). This should be
 227 considered as qualitative, since spectra acquired at different locations, geometries and local
 228 times are considered (see Tables 1 and 2). Therefore, clouds are likely characterized by
 229 different vertical distributions and microphysical properties, driven by a radiative forcing that
 230 is changing between early and mid-morning. Also, differential sun-glint effects (dependent on
 231 geometry and wind strength) could produce differences in the overall reflectivity of the ocean
 232 (Cox and Munk, 1954). All these effects (straylight could also have an impact here, see
 233 Langevin et al, this issue) are likely to contribute to non-linear offsets in the continuum below
 234 about 700 nm (e.g. Zinner et al., 2016)(straylight could also have an impact here, see
 235 Langevin et al, this issue), and slightly different depth and shape of water absorption bands,
 236 not ascribable solely to differences in spectral resolution.
 237



238 A



239 B



240 C

241 **Figure 3:** comparison between MAJIS and PRISMA reflectances in log (A) and linear (B)
 242 scales related to ocean, liquid water clouds and ice water clouds (the latter multiplied by 10
 243 for clarity in panel A). PRISMA spectra are selected from two orbits in session 7, MAJIS
 244 ones from orbits C7 (ice clouds) and C10 (ocean and liquid water clouds). Panel C shows
 245 the SNR estimated for the two instruments (cube C15 for MAJIS, one cube of session 07 for
 246 PRISMA) as described in Section 2.3.1. The red shaded area indicates the spectral region
 247 possibly affected by straylight contamination, not yet fully assessed in both datasets.

248

249 The three endmembers in Figure 3 show similar trends in reflectivity, with the main
250 absorption bands' shape correctly reproduced, even if the probed atmospheric structure is
251 probably not the same. For example, MAJIS liquid water clouds spectrum shows wider wings
252 and a flatter bottom for the bands at 1400 and 1900 nm, suggesting different scattering
253 properties in the atmospheric column for the two cases (see Section 4.2.4). A slightly flatter
254 bands' bottom is also observed in the ocean spectrum (blue compared to the orange
255 PRISMA spectrum). On one side, this could indicate that early-morning thin clouds in the
256 mid-high troposphere are mixed in MAJIS footprint, preventing the formation of the narrower
257 water lines inside the bands (MAJIS spectrum refers to 7:30 local time, when the presence of
258 unresolved hazes is likely). On the other hand, such low signals could reach the instrument
259 noise equivalent spectral radiance (NESR), hence explaining the featureless bands' bottom.
260 We derived an upper limit for the NESR by investigating the darkest ocean region in the
261 selected MAJIS cube (C10), resulting in about 10^{-3} W/(m² μm sr) at 1900 nm. This value
262 corresponds to reflectances of 10^{-4} , about one order of magnitude below the ocean signal at
263 that wavelength (Figure 3A), hence making the mixed-footprint hypothesis more likely. The
264 occurrence of saturation in some parts of MAJIS spectrum is highlighted in the ice clouds
265 comparison, evident as a broad absorption between 900 and 1100 nm in Figure 3B. MAJIS
266 uncertainties are extensively discussed in the paper by Poulet et al. (this issue), but here we
267 attempt an *a posteriori* estimation of the spectral signal to noise ratios (SNR) for both
268 instruments by performing a statistical analysis of spatial fluctuations computed in 5x5 pixels
269 boxes (Figure 3C). For each wavelength (excluding saturated regions) we select those
270 regions producing the minimum relative error, hence representing both noise statistics and
271 true variations in the observed scene. As a result, the spectral SNRs in Figure 3C refer to
272 wavelength-dependent locations in the respective cubes, rather than to a single region. This
273 means that the high frequency oscillations in the red and black lines are mostly driven by
274 spatial differences between the selected boxes (at the scale covered by the respective
275 cubes). Values below ~700 nm (red shaded area in Figure 3C) could be driven by
276 differences in clouds/aerosols' properties (in turn impacting the intensity of Rayleigh
277 scattering), and are possibly contaminated by the presence of straylight affecting the actual
278 trend of the SNR for both instruments.

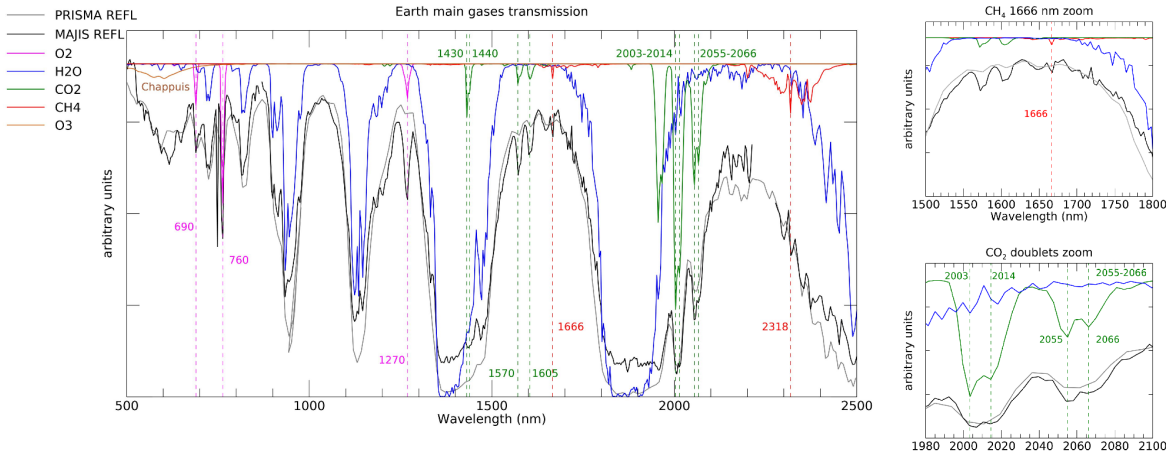
279

280 **2.3.2. Gaseous compounds**

281

282

283 Figure 4 compares sample MAJIS/PRISMA liquid water clouds reflectance spectra with
284 two-way vertical transmission due to O₂, H₂O, CO₂, CH₄, N₂O and CO₃, based on an average
285 vertical structure from Efremenko and Kokahnovsky (2021), calculated through line-by-line
286 method with line parameters from the HITRAN database (Gordon et al., 2022) and from O₃
287 cross sections by Gorshchev et al. (2014) and Serdyuchenko et al. (2014). Finally,
288 transmissions are then convolved at the MAJIS spectral resolution.



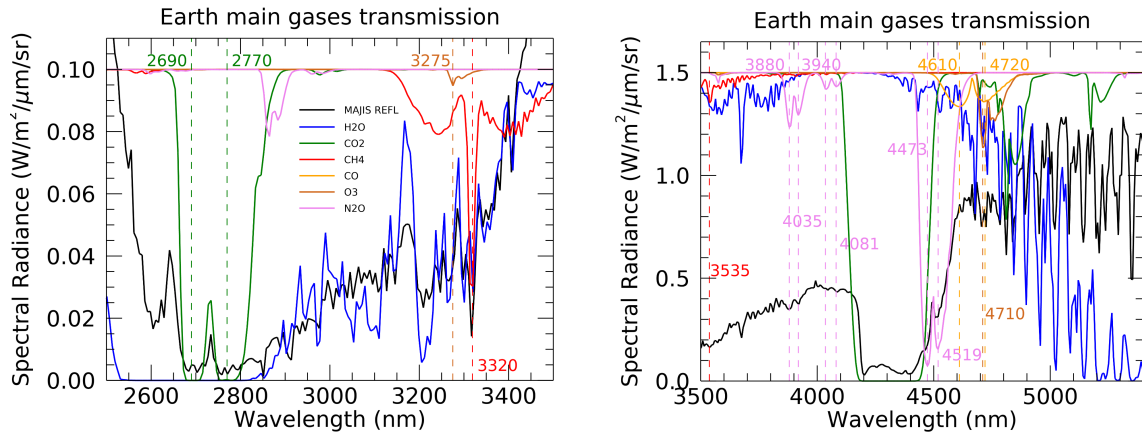
289

290 Figure 4: MAJIS (black, taken from C7) and PRISMA (cyan, taken from session 7)
 291 normalized reflectances (both pertaining to liquid water cloud scenarios) compared to main
 292 Earth's atmospheric gases two-way transmissions convolved on MAJIS spectral grid. Vertical
 293 dashed lines indicate the main non-H₂O molecular lines identifiable in the observations.
 294 Zooms related to the CH₄ 1666 nm absorption line, and the CO₂ doublets at 2003-2014 nm /
 295 2055-2066 nm are shown in the upper and lower right panels respectively.

296

297 In their common spectral range, both instruments allow to identify the main absorption
 298 features of H₂O, O₂ and CO₂ (Figure 4, see also Poulet et al., this issue). The reduced
 299 spectral resolution of PRISMA makes it difficult to resolve narrow features like the methane
 300 absorption at 1666 nm (Figure 4, upper right panel), the close doublets of CO₂ at 2003-2014
 301 nm and 2055-2066 nm (Figure 4, lower right panel), or shallower lines of water. On the other
 302 hand, the PRISMA spatial resolution is expected to reduce the spatial mixing of different
 303 types of surfaces or aerosols, allowing a more robust tracking of localized and transient
 304 phenomena (e.g. smog layers, ice patches, oil spills, CO₂ emissions, etc.). At wavelengths
 305 around 600 nm a broad absorption possibly matching the O₃ Chappuis band appears in both
 306 datasets. In MAJIS, this is enhanced over thick clouds and in particular in grazing
 307 illumination conditions (Section 4.4) in which the atmospheric column above ~20 km is
 308 directly illuminated resulting in a very long photon path length that increases the absorption
 309 from O₃ in the scattered light (most of terrestrial ozone resides between altitudes of 20 and
 310 40 km). Nevertheless, a better quantification requires a more rigorous assessment of the
 311 straylight contamination (Langevin et al., this issue).

312 Besides the better spectral resolution, MAJIS also has the advantage of an extended
 313 spectral range covering wavelengths from 2500 nm up to 5560 nm. In this range, thermal
 314 emission dominates and provides information on the temperature of the sampled
 315 atmospheric layers, or of the ocean and clouds. This interval is characterized by several H₂O
 316 absorption bands (the stronger one centered at about 2700 nm), strong and saturated CO₂
 317 ones at 2690, 2770 and 4300 nm, and weaker CH₄, O₃, CO and N₂O signatures (Figure 5,
 318 see also Guerlet et al., this issue). In particular, the strong CO₂ absorption (and emission) at
 319 4300 nm, can be used exploited for the estimation of the vertical structure of atmospheric
 320 temperatures (see Poulet et al., this issue).



321

322 **Figure 5:** MAJIS (black) ~~spectral radiance~~ ~~reflectance~~ compared to main Earth's
 323 atmospheric gases two-way ~~spectral~~ transmissions (offset for clarity) in the 2500 - 3500 nm
 324 range (left) and 3500-5400 nm range (right). Thermal emission is not considered in the
 325 transmission computation and all spectra are convolved to the MAJIS spectral grid.

326

327 3. Methods

328

329 In this section we describe different methods for investigating the information content in the
 330 data, including surface/cloud features identification (Section 3.1), ice characterization
 331 (Section 3.2), clouds' altitude estimation (Section 3.3) and high-altitude features investigation
 332 (Section 3.4).

333

334 3.1. Surface and clouds identification

335

336 In principle, Earth observations can encompass different types of surfaces, commonly
 337 discriminated spectrally through indices expressed in the formalism of *Normalized Difference*
 338 *spectral Indices* (NDIs, see Wolf, 2010 for a general review). Useful examples are given in
 339 Hurley et al., 2014 (dealing with Rosetta/VIRTIS-M data, Coradini et al., 1999) and in Oliva
 340 et al., 2017 (dealing with both Rosetta and Venus Express/VIRTIS-M data, Drossart et al.,
 341 2004). Table 3 summarizes these indices (derived from spectral endmembers from
 342 Rosetta/VIRTIS-M acquisitions, Figure 6A-B, since MAJIS observations did not cover
 343 surface features in daylight) that we test on PRISMA data (Figure 6C-D) as a benchmark for
 344 the future September 2026 EGA in which Africa observations are planned. A new ocean
 345 index is also defined specifically for MAJIS data, which do not cover all wavelengths of the
 346 nominal ocean NDI. It is worth stressing that the ocean class should not be considered as
 347 representative of clear-sky conditions as it may actually include some amount of aerosol
 348 opacity (Section 2.3.1). No specific index has been adopted for generic clouds identification,
 349 but we rather assign to this class all pixels that do not meet any of the surface classes'
 350 conditions. Indices thresholds can be studied taking advantage of proxy images (e.g. the
 351 PRISMA one shown in Figure 6C, not pertaining to EGA sequence) in which the changing
 352 reflecting structures can be clearly identified. The derived values depend on instrument
 353 features and require specific tuning when switching between different datasets. Figure 6C-D
 354 shows how the different types of spectral classes can be reliably identified, even if, in this
 355 case, no ice clouds are present. Other examples of application of the ocean, clouds and ice
 356 indices from Table 3 to MAJIS and PRISMA data are discussed in Section 4.1. Instead, the

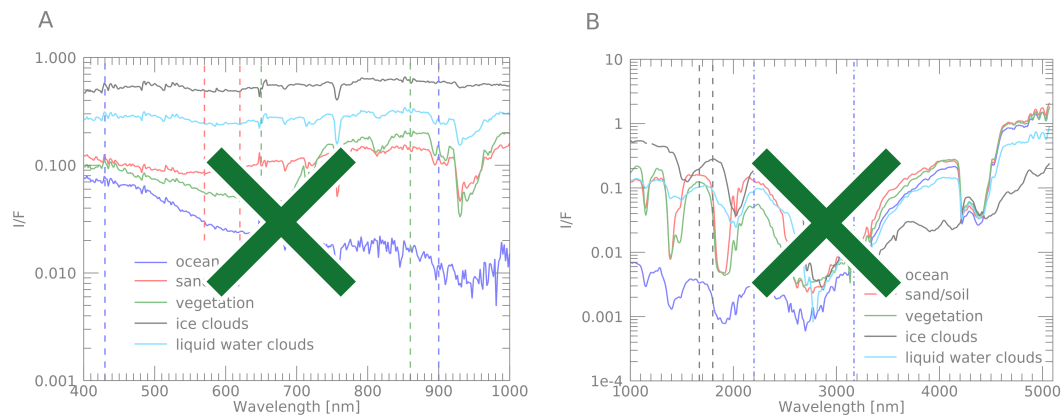
357 application of surface-related indices to MAJIS data did not result in positive identification,
 358 since land features in MAJIS data are not seen in daylight illumination, making NDIs not
 359 applicable.

360

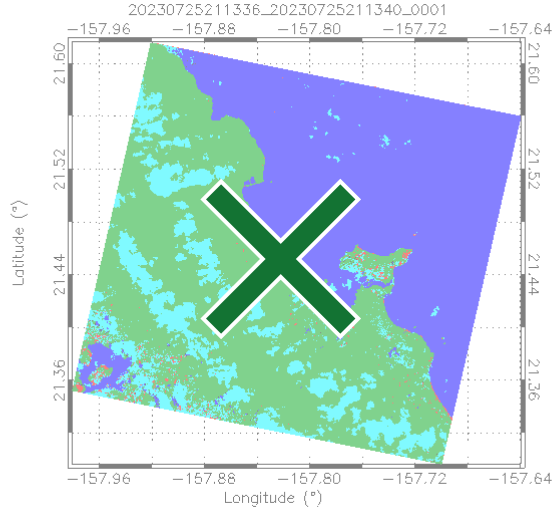
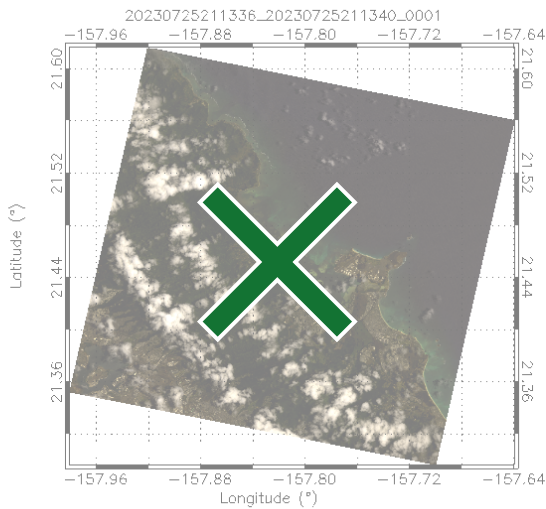
SPECTRAL CLASS	SPECTRAL INDEX	SPECTRAL SIGNATURE	FIGURE
Vegetation	NDVI: $\frac{R_{860} - R_{650}}{R_{860} + R_{650}}$	Chlorophyll absorption in the red band	6D
Sand/Soil	NDSI: $\frac{R_{570} - R_{620}}{R_{570} + R_{620}}$	Enhanced contrast between the red and green bands	6D
Ocean	NDWI: $\frac{R_{430} - R_{900}}{R_{430} + R_{900}}$	Enhanced reflectivity in the blue with respect to NIR wavelengths	6D - 12D
MAJIS Ocean	$\frac{R_{2200}}{R_{3170}}$	Low solar I/F, large thermal emission	12C
Ice Clouds	$\frac{R_{1670}}{R_{1800}}$	Shift of the 1500 nm H ₂ O ice absorption band to longer wavelengths with respect to the liquid phase (different arrangement of hydrogen bonds)	12C - 12D
Cloudy	pixels not assigned to surface types	/	6D - 12C - 12D

361

362 **Table 3.** Spectral indices for the identification of different spectral classes related to surfaces
 363 and clouds. R indicates I/F and the subscript is the wavelength in nanometers.

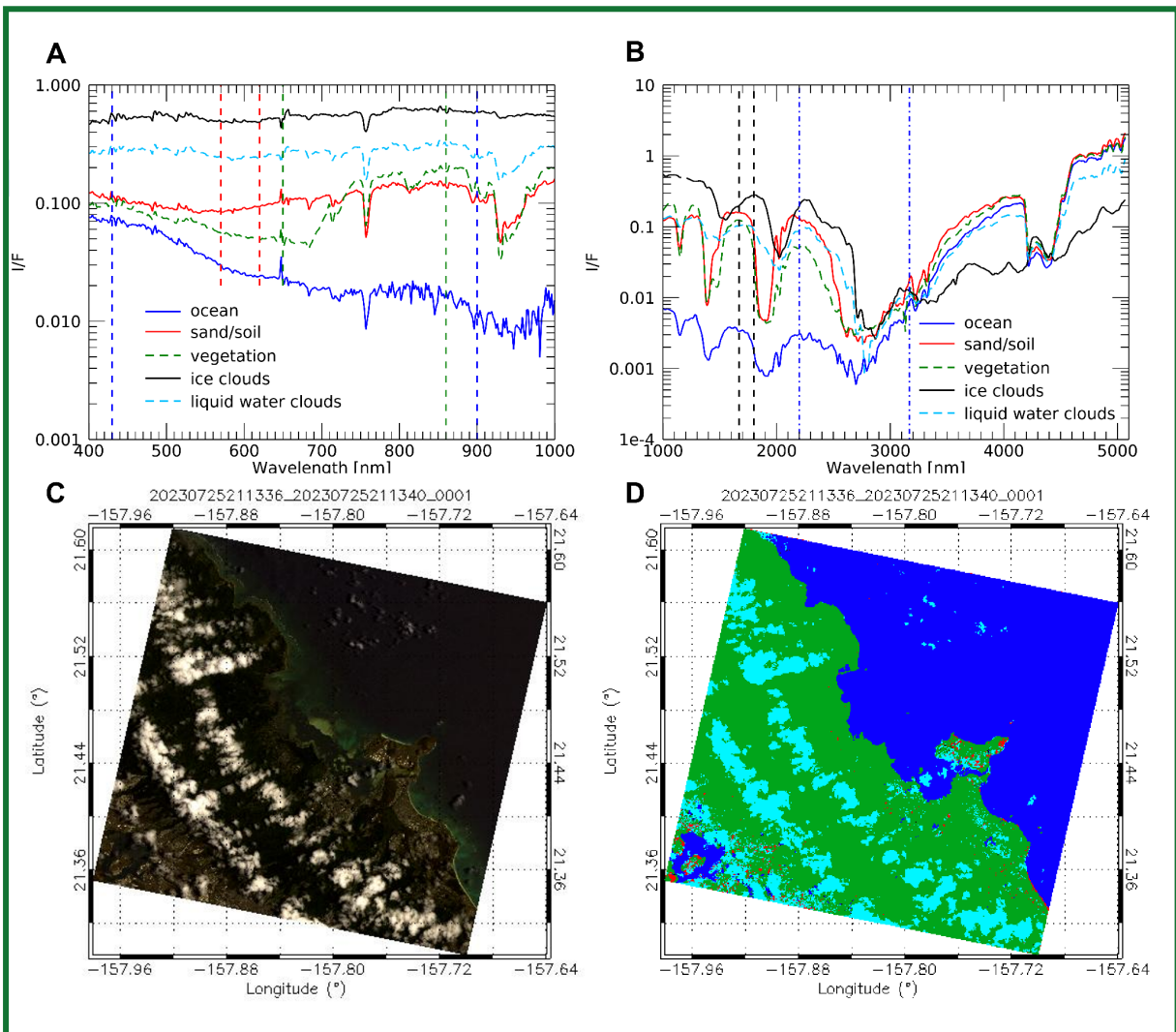


364



365 **E**

D



366

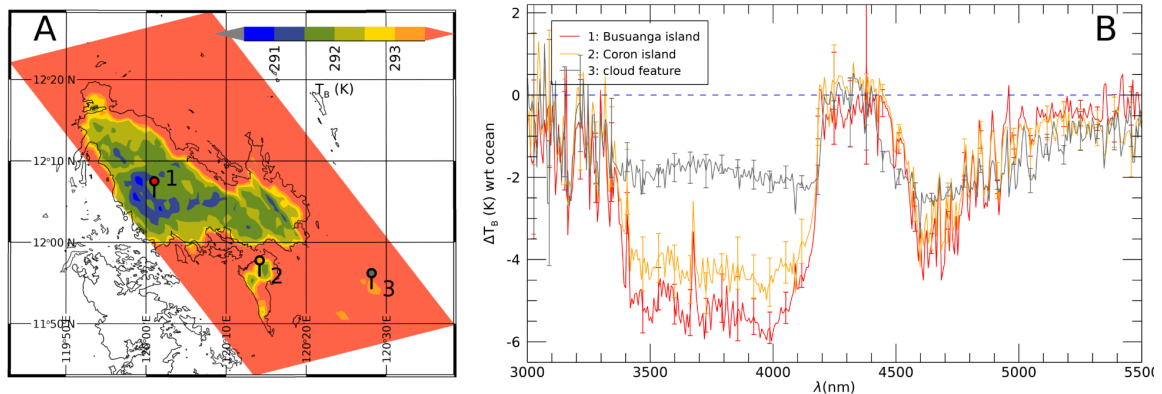
367 **Figure 6:** A: Reflectance endmembers of different classes of surface and clouds, derived
 368 from Rosetta/VIRTIS-M VIS channel Earth observations (Oliva et al., 2017). Vertical dashed
 369 lines share the color of the corresponding spectral endmember and identify the wavelengths
 370 adopted in the index definition (blue ones refer to the NDWI). B: same as in A but I/F spectra
 371 are from the NIR channel of VIRTIS-M are shown (blue dashed-dotted lines refer to the
 372 MAJIS ocean index). C: Example of a PRISMA RGB image covering different surface types

373 (data cube 2023072521336_20230725213340) targeting the eastern coastal line of Honolulu
 374 island ($R=680$ nm; $G=570$ nm, $B=440$ nm). **D**: distribution of spectral classes obtained from
 375 the spectral indices in Table 3. Green pixels indicate vegetation, red ones are sand, cyan
 376 ones are clouds, blue ones indicate ocean/water (no ice clouds present).

377

378 In the specific conditions of MAJIS EGA sequence, the most robust land identification must
 379 rely on soil/ocean contrast in thermal emission (Section 4.4), triggered by the different
 380 thermal inertia of the two classes. However, also the presence of clouds in the line of sight
 381 induces a decrease of the observed brightness temperature (T_B), hence land identification
 382 requires matching the shapes of low T_B regions within known coastlines. The largest land
 383 region emerging in this way is shown in Figure 7 (cube C4), (Philippines's Busuanga and
 384 Coron islands in cube C4), whose identification also allows a refinement of MAJIS pointing
 385 reconstruction (Seignovert et al., this issue). The largest brightness temperature contrast for
 386 both land/ocean and cloud/ocean cases occurs in the 3500-4000 nm and 4600-4800 nm
 387 spectral ranges, which are less absorbed by atmospheric H_2O and CO_2 . The application of
 388 this method to other MAJIS data is illustrated in more detail in Section 4.4.

389



390

391 **Figure 7:** Land detection obtained by comparing the shapes of low brightness temperature
 392 (T_B) regions in MAJIS cube C4 with known coastlines. **A)** Identification of Busuanga and
 393 Coron islands (markers 1 and 2 respectively), colder than the surrounding ocean, as well as
 394 clouds (marker 3). **B)** Spectral contrast in brightness temperature (T_B) with respect to the
 395 ocean spectrum, measured over the islands (Busuanga in red, Coron in orange) and over a
 396 thin cloud (grey curve). Coastlines data from OpenStreetMap, available under the Open
 397 Database License.

398

399 3.2. Ice characterization

400

401 MAJIS and PRISMA data allow investigating the distribution of physical properties of ice and
 402 how they relate, for example, to the altitude of the clouds where it is identified (see Sections
 403 4.1 and 4.2). The temperature, crystallinity, grain size, purity, and density affect the shape of
 404 ice absorption bands (in particular the main ones at 1500 nm and 1900 nm) and of the
 405 continuum. Since the long wavelength shoulder of the 1900 nm band encompasses the
 406 noisy junction between the VISNIR and IR channels of MAJIS, we focus on the 1500 nm
 407 band, spectrally well resolved in both MAJIS and PRISMA datasets. This band has a
 408 characteristic asymmetry (due to its differential intensity with respect to the 1900 nm one,
 409 e.g. Stephan et al., 2021) affecting the position and shape of the in-between transmission
 410 window peak (~1700 nm) and has been used exploited for the definition of the ice index in

411 Table 3. Within the 1500 nm band, the weaker 1650 nm absorption is present. Its strength is
 412 a proxy for the degree of the ice crystallinity and temperature (Fink and Larson, 1975;
 413 Filacchione et al., 2016). It is also observable in PRISMA, even if shallower and noisier due
 414 to the lower spectral resolution (see zooms in Figure 8A and B).

415 The 3000 - 4000 nm wavelength range, not accessible to PRISMA, hosts two ice reflection
 416 peaks at around 3100 nm (the Fresnel peak) and 3700 nm (Figure 8C). The former varies in
 417 shape and intensity as a function of the ice crystallinity (Cartwright et al., 2025) while the
 418 latter shifts to longer wavelengths as temperature increases (e.g. Filacchione et al., 2016,
 419 see Section 3.3.3). Fresnel peak position variations are estimated in the data through
 420 cross-correlating each ice spectrum with a constant shape (average peak shape in each
 421 cube) which is rigidly shifted with a 0.1 nm sampling (hence allowing the estimation of the
 422 peak with a sampling better than the nominal MAJIS one). On the other hand, the 3700 nm
 423 peak position is obtained through fitting with a Gaussian function, reliably reproducing its
 424 shape.

425 Another proxy of the ice temperature is the intensity of its thermal emission, becoming
 426 significant at wavelengths larger than 4500 nm (Figure 8D). However, in this range the
 427 emitted radiance is absorbed by a plethora of narrow bands of gaseous water, and therefore
 428 only a narrow transmission window around 4600 nm is suitable for this purpose. Table 4
 429 summarizes these ice spectral features, identifiable in MAJIS and PRISMA data. The
 430 average uncertainties Δ are propagated taking into account the SNR estimates described in
 431 Section 2.3.1.

432

433

ICE PARAMETER	Δ MAJIS	Δ PRISMA	ICE PROPERTIES
1500 nm band depth	< 1 %	< 1 %	number density / grain size
1500 nm band asymmetry	< 2 %	< 3 %	grain size / crystallinity
1650 nm band depth	10 %	20 %	crystallinity
<i>Fresnel peak position</i> <i>Fresnel peak intensity</i>	<i>2 nm</i> <i>< 1 %</i>	<i>/</i>	<i>temperature / crystallinity</i>
<i>3700 nm peak position</i> <i>3700 nm peak intensity</i>	<i>0.2 nm</i> <i>< 1 %</i>	<i>/</i>	<i>temperature / crystallinity</i>
<i>4600 nm thermal intensity</i>	<i>< 1 %</i>	<i>/</i>	<i>temperature</i>

434 Table 4: investigated ice parameters and related average uncertainties (Δ) and ice
 435 properties. Cells in light blue indicate parameters that Entries in italic only refer to MAJIS
 436 dataset.

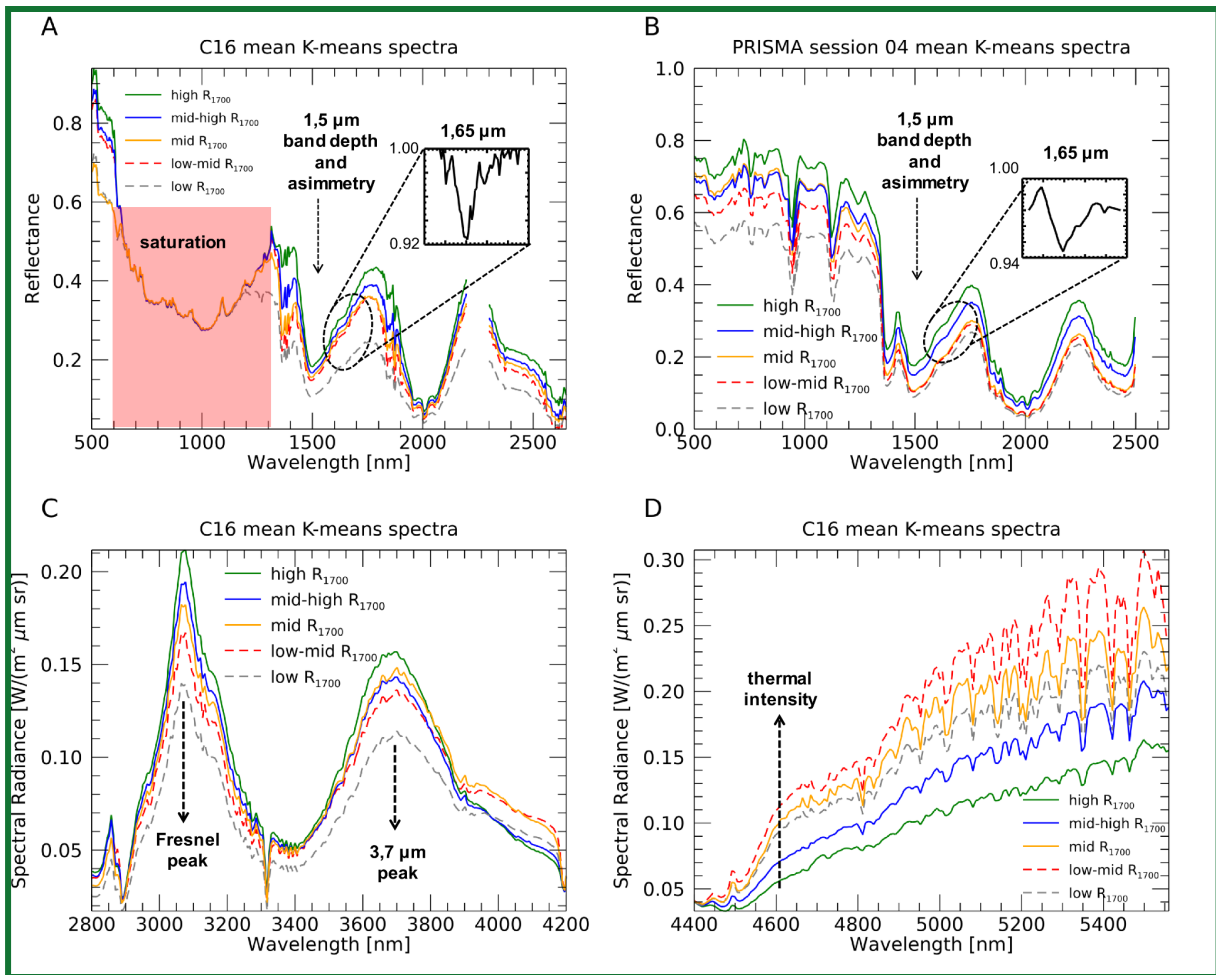
437

438 As a first investigation of the ice spectral variability in MAJIS and PRISMA observations we
 439 take advantage exploit of the unsupervised K-means classification algorithm included in the
 440 ENVI software package, version 6.0 (Exelis Visual Information Solutions, Boulder, CO, USA,
 441 <https://www.nv5geospatialsoftware.com/Products/ENVI>, accessed on 15 December, 15,
 442 2025). This algorithm is capable of grouping the observations data into an ensemble of "K"
 443 non-overlapping clusters, of observations driven by spectral similarity, whose average
 444 spectra are and with "K" average spectra, representative of the main signatures in the

445 dataset. This is done through an iterative minimum distance technique whose details are
446 described in (Tou and Gonzalez, (1974). In Given the qualitative approach of this preliminary
447 analysis, we arbitrarily set the algorithm to produce K=5 output average spectra, which is
448 enough clusters for visualizing discussing the variability of the main ice diagnostic spectral
449 features. It must be noted that, since we are also interested in features pertaining to near-
450 infrared wavelengths, in MAJIS case the full VISNIR+IR spectral range is considered, and
451 wavelengths longward of 2500 nm contribute to the clustering as well. As we will see in
452 Section 4.1, this also has an impact on the spatial distribution of the clusters. The resulting
453 average spectra in the solar range are shown highlighted in different ranges in Figure 8A and
454 Figure 8B for MAJIS cube C16 and one of PRISMA session 04 cubes respectively. These
455 spectra clusters result to be mainly driven by the changing intensity of the continuum at visible
456 wavelengths, in turn providing information related about to the opacity of the ice clouds.
457 However, it must be noted that since we are also interested in features pertaining to near-
458 infrared wavelengths, in MAJIS case the full spectral range is considered, and wavelengths
459 longward of 2500 nm contribute to the clustering as well. As we will see in Section 4.1, this
460 also has an impact on the spatial distribution of the clusters. The color scale is associated
461 with increasing reflectance of the transmission window at 1700 nm (dashed grey, cyan,
462 dashed red, orange, blue and green from low to high, indicating increasing opacity and
463 variable crystal sizes). The same color scheme is retained for the intensity of Fresnel peak at
464 3100 nm in MAJIS data (Figure 8C), diagnostic of the ice crystallinity. Instead, spectra with
465 intermediate reflectances at 1700 nm switch order within the 3700 nm ice reflectivity peak
466 (dashed red to blue to orange from low to high, Figure 8C) indicating the increased weight of
467 thermal emission on the overall signal in this range. At MAJIS wavelengths larger than $\lambda >$
468 4500 nm (Figure 8D) the initial color scheme is totally disrupted, due to the mixing of
469 information about cloud emissivity, cloud temperature (i.e. the altitude) and gaseous opacity.
470 The combination of high NIR reflectances and low thermal emission (green spectrum cluster)
471 suggests the presence of optically thick high-altitude clouds, as confirmed by the shallower
472 water absorption bands longward of 4900 nm. On the other hand, large thermal radiance
473 and deep water bands associated with intermediate NIR reflectance (dashed red
474 spectrum cluster) indicate a population of moderate opacity clouds at quite low altitudes. The
475 other spectra clusters present intermediate properties in the thermal range, not strongly
476 correlated with the NIR reflectance, calling for mixed-phase clouds of variable microphysical
477 properties and vertical structure.

478

479



480

481 **Figure 8:** **A:** mean reflectance spectra from the K-means clustering algorithm for MAJIS
 482 cube C16 ($\lambda < 2500$ nm). The red shaded area indicates ($\lambda < 2500$ nm, wavelengths that are
 483 saturated due to the high reflectivity of clouds are highlighted by the red shaded area).
 484 Colors indicate different regimes of the continuum reflectance, are ordered with increasing
 485 taken as reference reflectance at of the 1700 nm transmission window (R_{1700}). (from cyan to
 486 green) **B:** same as in A but for PRISMA session 04 (full spectral range). The insets in **A** and
 487 **B** zoom between 1570 and 1780 nm to show the average 1650 nm band normalized to the
 488 continuum. **C:** MAJIS radiances in the $2800 < \lambda < 4200$ nm range, zooming on the Fresnel
 489 and 3700 nm ice reflectivity peaks. **D:** thermal part of the spectrum longward of 4400 nm. In
 490 all panels, dashed arrows highlight diagnostic spectral features of the ice.

491

492 3.3. Estimation of clouds' altitude

493

494 The most straightforward method for evaluating cloud altitudes involves the correlation of the
 495 brightness temperature at a given wavelength (e.g. 4610 nm, less affected by gaseous
 496 absorption in the MAJIS range) with a known vertical temperature profile. For ice clouds,
 497 temperatures can be derived from the 3700 nm peak position (Section 3.3.3). Other methods
 498 that we consider here are based on O_2 absorption bands' variability and on the analysis of
 499 clouds' shadows (Sections 3.3.1 and 3.3.2). In this study, we rely on a fixed average
 500 temperature profile (Efremenko and Kokhanovsky, 2021), which may be not representative
 501 of the actual thermodynamic conditions of the atmosphere during the observations. As a
 502 consequence, all the methods that we adopt yield a range of results, each affected by their

503 own intrinsic limitations. Although they appear quite consistent with each other, more
504 quantitative investigations are postponed to future analyses.

505

506

3.3.1. O₂ band depth variability

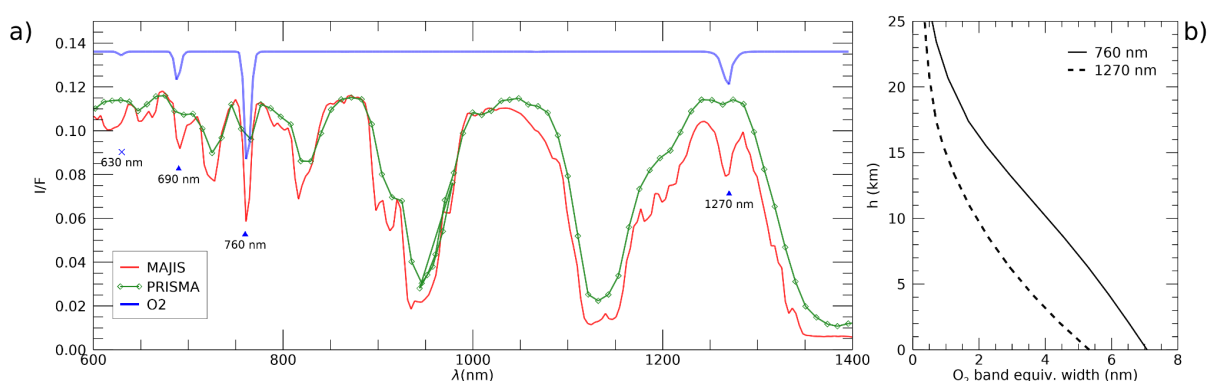
507

508 The O₂ spectral features covered by both MAJIS and PRISMA observations consist of the
509 absorption bands at 630 nm, 690 nm, 760 nm and 1270 nm (Newnham & Ballard, 1998;
510 Smith & Newnham, 1999). As we can see in Figure 9A, MAJIS can resolve all bands except
511 the 630 nm one, while PRISMA data can only partially resolve the 760 nm one. The
512 strongest 760 nm band is the most used from satellite measurements in the near-infrared
513 (e.g. GOSAT, Butz et al., 2011; SCIAMACHY, Bovensmann et al., 1999; TROPOMI, Veeffkind
514 et al., 2012; OCO-2/3, Eldering et al., 2019) for inferring bulk atmospheric quantities like
515 temperature profile, airmass (Stevens et al., 2017), aerosol and clouds properties (Geddes &
516 Bösch, 2015). O₂ is a well-mixed component of the atmosphere, hence the curves of growth
517 of its absorption bands with altitude in the presence of optically thick clouds can be
518 translated into the altitude of the cloud top (e.g. Wei et al., 2024).

519 In our analysis we applied a simplified scheme for retrieving cloud top altitudes from the 760
520 nm band in the PRISMA case and from both 760 and 1270 nm O₂ bands for MAJIS data.
521 The different strength of the two bands implies a bit different curve of growth with altitude
522 (Figure 9B), with the 1270 nm one less sensitive to higher clouds but more suitable for
523 characterizing lower structures. The 630 and 690 nm bands, intrinsically weaker and more
524 sensitive toward the surface, are not used in this analysis.

525 The comparison of a measured O₂ band depth with its theoretical curve of growth, evaluated
526 for the actual airmass, allows us to directly retrieve the cloud top altitude (Section 4.2.1). It is
527 worth stressing that although altitude, pressure and temperature of the cloud top are
528 important atmospheric parameters (Nakajima et al., 2019), our simplified scheme neglects
529 details of vertical distributions and scattering properties, introducing possible biases in the
530 retrieved absolute values. Propagating the MAJIS uncertainties previously discussed
531 (Section 2.3.1) and assuming suitable model ones (~10% on the oxygen vertical profile
532 induced by local changes in gaseous temperature, density, humidity), errors on cloud top
533 altitude average to values of ~1 km, for both the 760 and 1270 nm bands. In addition, the
534 1270 nm band is known to contain a significant airglow emission feature that can alter the
535 band depth and introduce further biases in the oxygen absorption evaluation (Kuang et al.,
536 2002).

537



538

539 Figure 9: **A)** Typical appearance of O₂ features in the spectra of MAJIS (red) and PRISMA
540 (green). Modeled spectral transmittance (in blue) highlights location and shape of the O₂
541 bands at 630, 690, 760, and 1270 nm. Only the last three can be detected/appreciated in

542 MAJIS spectra (red curve), while only the strongest 760 nm band is identifiable in PRISMA
543 spectra (red curve). **B):** Examples of curves of growth of the O₂ absorption bands at 760
544 (solid curve) and 1270 nm (dashed curve) in the standard clear-sky atmospheric column
545 adopted in this work. The absorption is shown as band equivalent width for a 2-ways path
546 with generic incidence and emission angles of 30°.

547

548 3.3.2. Cloud shadows analysis

549

550 The length of projected clouds shadows gives an estimate of their altitude, provided that the
551 illumination geometry is well known. Significant lengths of projected shadows are more
552 easily seen in the case of tall convective clouds in slant solar illumination. In the MAJIS case,
553 clear shadows have been identified for strong convective events surrounded by widespread
554 background clouds, hence their length can only give hints on relative altitudes (see Section
555 4.2.2). Here we adopted the simplest assumption of homogeneous cylindrical cloud shapes,
556 without accounting for the actual three-dimensional cloud density distribution, to estimate the
557 height of clouds' top with purely geometrical considerations. Under these hypotheses the
558 associated uncertainties in this kind of measurements are mainly driven by errors in edge
559 detection (for both cloud and shadow edges), in the assumption on the cloud's three-
560 dimensional shape and how this is horizontally and vertically distributed and, as a
561 consequence, are limited by the spatial resolution. Errors on solar incidence angle may also
562 play a role in very slant illumination, and the total relative uncertainties estimated in the
563 conditions of MAJIS observations range between 6 and 10%. The application of the method
564 is shown. In order to simplify the method, we assume a cylindrical shape for the convective
565 tower investigated in Section 4.2.2.

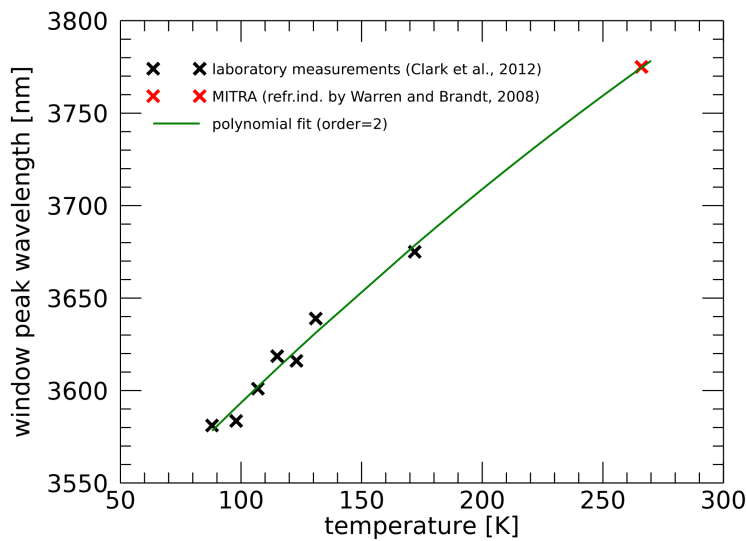
566

567 3.3.3. Derivation of clouds' altitude with the ice temperature

568

569 We apply to Earth's icy clouds the same method by Filacchione et al. (2016), who estimated
570 the temperatures of Saturn's icy satellites surfaces from the displacement of the 3700 nm ice
571 peak, deriving from a shift of the imaginary part of the ice refractive (Mastrapa et al., 2009).
572 In that method, temperature-dependent peak reflectivities were derived from laboratory
573 measurements by Clark et al. (2012), spanning between 88 and 172 K, a range too low to
574 describe Earth troposphere where clouds are commonly observed. We extrapolate the
575 peak-temperature dependence by also simulating the ice reflectivity at 266 K, i.e. the
576 temperature of the optical constants by Warren and Brandt (2008). Since the ice grain size
577 has little effect on the peak position (Filacchione et al., 2012) we assume an effective radius
578 of 20 μm, representative of cirrus clouds (LeMone, 1988). The resulting trend covering from
579 88 to 266 K is shown in Figure 10 (black and red crosses). It is reliably fit with a
580 second-degree polynomial (green line) and can be used for a qualitative estimation of the ice
581 temperature in MAJIS observations (Section 4.2.3).

582



583

584 **Figure 10:** correlation between ice temperature and 3700 nm reflectivity peak position. Black
 585 crosses represent laboratory measurements by Clark et al. (2012), the red cross indicates an
 586 RT simulation performed with ice grain size of 20 μm and optical constants by Warren and
 587 Brandt (2008), and the green line represents a second degree polynomial fit of all data (see
 588 Section 3.3.3).

589

590

3.3.4. Forward RT modeling on liquid and ice H₂O clouds;

591

592 The most accurate method for determining clouds' vertical distribution is through full RT
 593 modeling. However, this would require a time-consuming retrieval of physical quantities that
 594 is beyond the scope of this paper. Instead of spectral inversion, we here perform a
 595 comparison of selected observations (those in Figure 3) with forward RT models obtained by
 596 manually tuning aerosols' physical parameters. The derived quantities are to be considered
 597 as orders of magnitude of the altitude and microphysical properties of Earth's clouds and
 598 aerosols. Forward models are produced with the MITRA RT tool (Oliva et al., 2016; 2018;
 599 Sindoni et al., 2017; D'Aversa et al., 2022), ~~adopting~~exploiting the optical constants from
 600 Hale and Querry (1973), Warren and Brandt (2008) and Kitamura et al. (2007) for computing
 601 the scattering properties of liquid water, water ice and silicate minerals (assumed as
 602 background aerosol), respectively. The spectral albedo of the ocean is taken from the
 603 ASTER spectral library (Baldrige et al., 2009). In this simplified scheme, we neglect thermal
 604 emission, discarding measurements longwards 3000 nm.

605 It is interesting to note that, even if beyond the scope of this paper, more accurate RT
 606 modeling could also be ~~considered~~exploited for the evaluation of straylight contamination
 607 (studied for MAJIS in Langevin et al., this issue), as it offers the possibility to extrapolate
 608 information from the NIR part of the spectrum to visible wavelengths.

609

610

3.4. High altitude emissions and atmospheric waves identification

611

612 Among the many gaseous features observable in the 4000-5500 nm MAJIS range, two are
 613 particularly interesting, being observed as emission bands: the CO₂ double-peak at the
 614 bottom of the main 4300 nm band and an O₃ signature around 4700 nm. Both are evident

615 above optically thick clouds at high altitudes, blocking the thermal contribution from the
616 surface and lower (hotter) atmospheric layers. The CO₂ peak is radiometrically much more
617 stable than other spectral features against variation of atmospheric structures (see Poulet et
618 al., this issue). It is known to result from the combination of a LTE component induced by
619 temperature increase in the stratosphere, and a non-LTE one due to the CO₂ excitation
620 primarily induced by direct solar pumping occurring at even higher altitudes (where
621 collisional quenching is no longer efficient, e.g. Cassini et al., 2025). The detailed analysis of
622 this emission feature in MAJIS data, implying the evaluation of CO₂ vibrational temperature
623 vertical profiles, is far beyond the purpose of this work. In any case, the spatial distribution of
624 the CO₂ emission intensity can provide interesting insights about the probed layers, and we
625 can indeed use it for detecting atmospheric waves and provide hints about their altitude and
626 propagation (see Section 4.3.1). CO₂ emission can be identified already in MAJIS
627 monochromatic frames at 4270 nm (i.e. the position of the main peak of the emission) but
628 the integration of the band in a narrow spectral range is useful for reducing noise and
629 enhancing the contrast in waves' investigation (Section 4.3). For the integration we consider
630 wavelengths between 4254 and 4333 nm, which probe high altitudes in the atmosphere and
631 are not affected by the thermal contribution from lower ones. Considering the SNR estimated
632 at these wavelengths (Figure 3C), we are able to detect waves whose relative intensity
633 between crests and troughs is about 1%, assuming a 3-sigma uncertainty for the radiance at
634 4270 nm.

635 On Earth ozone has a maximum density in the lower stratosphere but its vertical distribution
636 strongly depends on latitude (see for example Bekki and Lefevre, 2009). It is produced
637 through a very fast and exothermic 3-body recombination reaction that includes O and O₂ in
638 the presence of a catalytic species (either N₂ or O₂). Aside from diagnostic bands at UV
639 (outside MAJIS domain) and VIS wavelengths (the Chappuis band discussed in Section
640 2.3.2), the 4700 nm one is the strongest feature clearly detectable within the MAJIS range.
641 This O₃ band is seen as either an absorption or emission feature in MAJIS nadir-looking
642 observations, depending on the overall thermal emission of the atmospheric column. In clear
643 sky conditions, when the emission from lower warmer layers is dominant, the O₃ 4700 nm
644 band is hardly detectable, being overcome by water absorption (as shown in Poulet et al.,
645 (this issue), unless radiative transfer modeling is performed on the data (e.g. Guerlet et al.,
646 this issue). In the presence of mid-altitude clouds, a shallow O₃ band appears in absorption,
647 while the obstruction of the densest part of the atmospheric column due to high-altitude
648 clouds makes the O₃ band appear in emission. Given this phenomenology, in this preliminary
649 study we investigate the O₃ emission amplitude through the difference between brightness
650 temperatures estimated at 4717 nm (strongest O₃ line) and 4660 nm (outside O₃ band). Such
651 a difference is positive when the O₃ is spectrally observed in emission, negative otherwise.

652

653

654

3.4.1. Atmospheric waves characterization

655

656 Atmospheric gravity waves are observed in almost all the MAJIS acquisitions (see examples
657 in Section 4.3.1) at the wavelengths of the central peak of the 4300 nm CO₂ band. Due to the
658 limited field of view, wave packets are usually not visible in their entirety and it is not possible
659 to identify the same wavy structures from one image to the other due to the large coverage
660 gaps, preventing the study of the wave speed propagation. Nevertheless, we attempt to
661 quantify wave properties and provide some hints on their altitude. ~~We investigated the~~
662 ~~horizontal wavelength, the total length of the packet, the azimuth angle of the direction of~~

663 propagation (anticlockwise), and the extension of the observed wavefront (packet width).
 664 The wave parameters—horizontal wavelength, total packet length, azimuthal extent, and
 665 packet width—are determined through visually processing manually for each image.
 666 Automated methods were not possible because of the variability in image appearance. After
 667 appropriate image stretching, the wavefronts are identified by and traced by drawing lines
 668 along the crests lines. The horizontal wavelength is defined as the average distance
 669 between consecutive crests within each wave packet. The total packet length is measured
 670 as the distance between the first and last identified crests. The azimuthal extent is derived
 671 from the common orientation of the crests counted counterclockwise, while the packet width
 672 is defined as the maximum crest length among those identified. Taking into account spatial
 673 resolution and signal contrast, uncertainties in size estimation are of about 7 km, while those
 674 on wavelengths are less than about 11 km.

675 Circular-wave patterns have been observed in some MAJIS images, likely resulting from the
 676 breaking of upward-propagating waves originating in sufficiently strong convective
 677 thunderstorms. Under this assumption, we attempt to infer the time delay between the
 678 wave-triggering event and its observation (Taylor and Hapgood, 1988; Dewan et al., 1998;
 679 see Section 4.3.1). This is done neglecting wind transport and assuming a simplified
 680 isothermal dispersion relation (Hines, 1960) in which the wave speed is negligible with
 681 respect to the speed of sound. For circular waves we also measured maximum radius and
 682 expansion speed. The latter depends on the measured length and period, as well as on the
 683 buoyancy period τ_B , for which a value of 5 min can be assumed as a good approximation at
 684 stratospheric altitudes (Dewan and Good, 1986). ¶

685 Because only a portion of the circle is visible in the images, the wave radius is inferred from
 686 the length of sagitta and chord, using the following formula:

$$687 \quad r = f/2 + c^2/8f \quad (1)$$

688 where f is the sagitta and c is the chord, observed in the images in pixels and converted to
 689 km using the instantaneous resolution in km/px reported in Table 1. The waves are assumed
 690 to occur at 15 km height, based on estimations the use of the brightness temperature of CO2
 691 emission at 4300 nm, used as a proxy for these features. Following the formulation in Taylor
 692 and Hapgood (1988) and Dewan et al. (1998), the wave period τ and expansion speed can
 693 be obtained using the following formulas:

$$694 \quad r^2 = \tau_B^2 [(1 + 1/(\tan \phi)^2)] \quad (2)$$

$$695 \quad v_{gx} = (\lambda_x / \tau) [1 - (\tau_B / \tau)^2] \quad (3)$$

696 with ϕ being the elevation angle identified by the wave propagation direction, $\lambda_x =$
 697 wavelength of the propagating wave, and τ_B =buoyancy period, the latter assumed to be
 698 equal to 5 min, which is a good approximation at stratospheric altitude (Dewan and Good,
 699 1986).

700

701 4. Results and discussion

702

703 We now present the results we obtain through the application of the methods discussed in
 704 Section 3. Section 4.1 provides a discussion on ice properties, Section 4.2 focuses on the

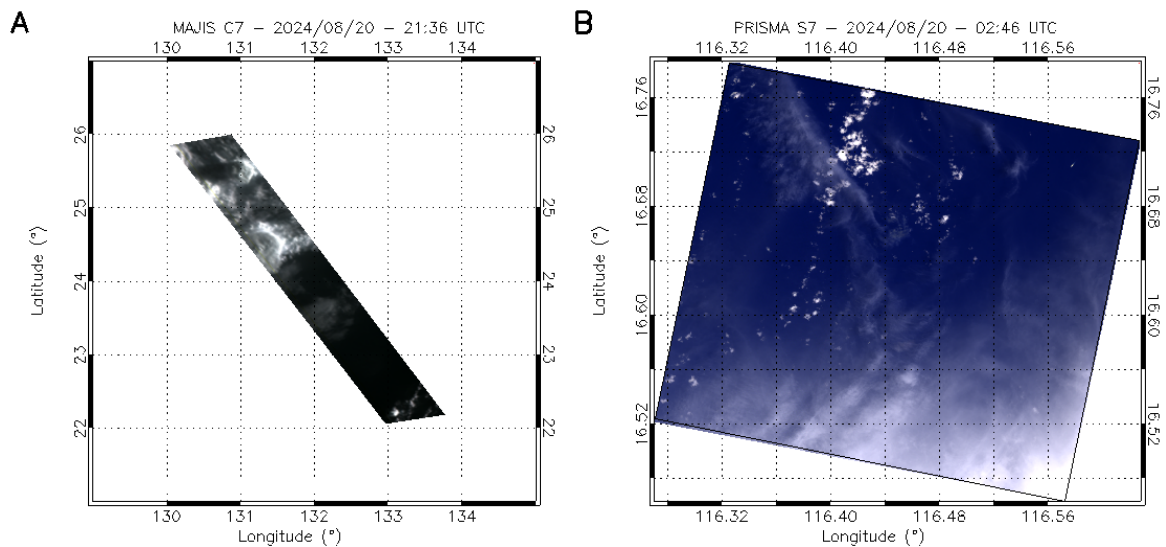
705 clouds' altitudes, Section 4.3 is devoted to high altitude features and Section 4.4 presents
706 results on land features identification.

707

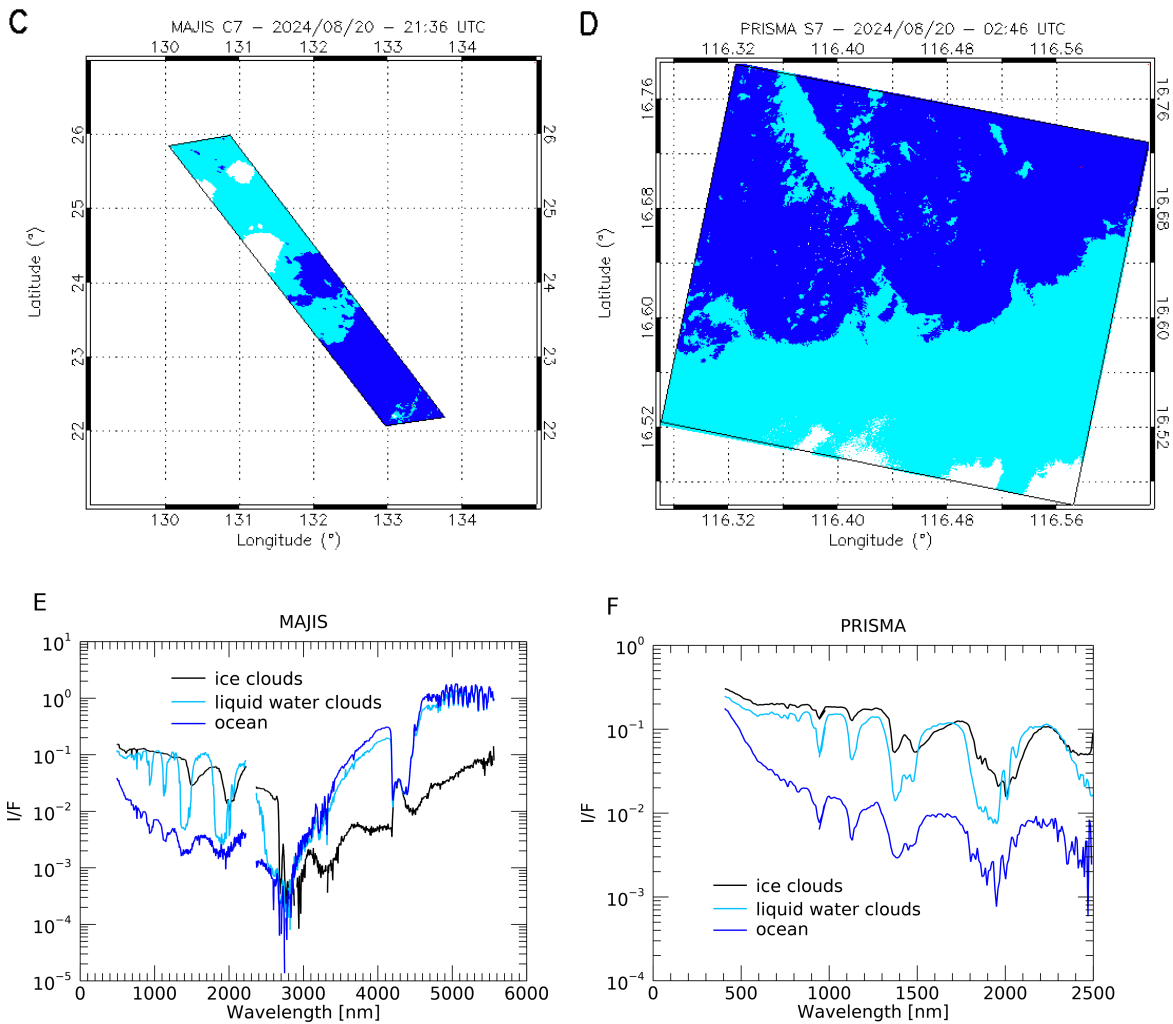
708 4.1. Icy clouds properties

709

710 Examples of two MAJIS and PRISMA cubes containing ice clouds, identified through the ice
711 spectral index in Table 3 (threshold < 1), are given in Figure 11. In the MAJIS case, ice is
712 found in localized convective clouds (Figure 11A and C), so high with respect to the
713 background structures that they even cast well detectable shadows (see Section 4.2.2).
714 Instead, in the PRISMA observation ice is detected both in diffuse bright clouds (e.g. at the
715 southern east corner of Figure 11B and D) and in thinner and less contrasted structures
716 (probably identifiable as high altitude cirrus clouds, e.g. the white regions around longitude
717 116.4° - latitude 16.5° , Figure 11B and D) hence proving the effectiveness of the index with
718 different regimes of ice optical depth. Sample spectra from the identified classes are shown
719 in Figure 11E and F for MAJIS and PRISMA respectively. It must be noted that the very low
720 albedo of the ocean in MAJIS spectrum at visual wavelengths ($< 1\%$) is due to the very slant
721 illumination conditions for the selected observation (incidence angle of about 80° for cube
722 C7, see Table 1). On the other hand, the spectra in the thermal range show consistency with
723 the expected temperature regimes, with very cold ice clouds and the ocean hotter than liquid
724 water clouds.



725



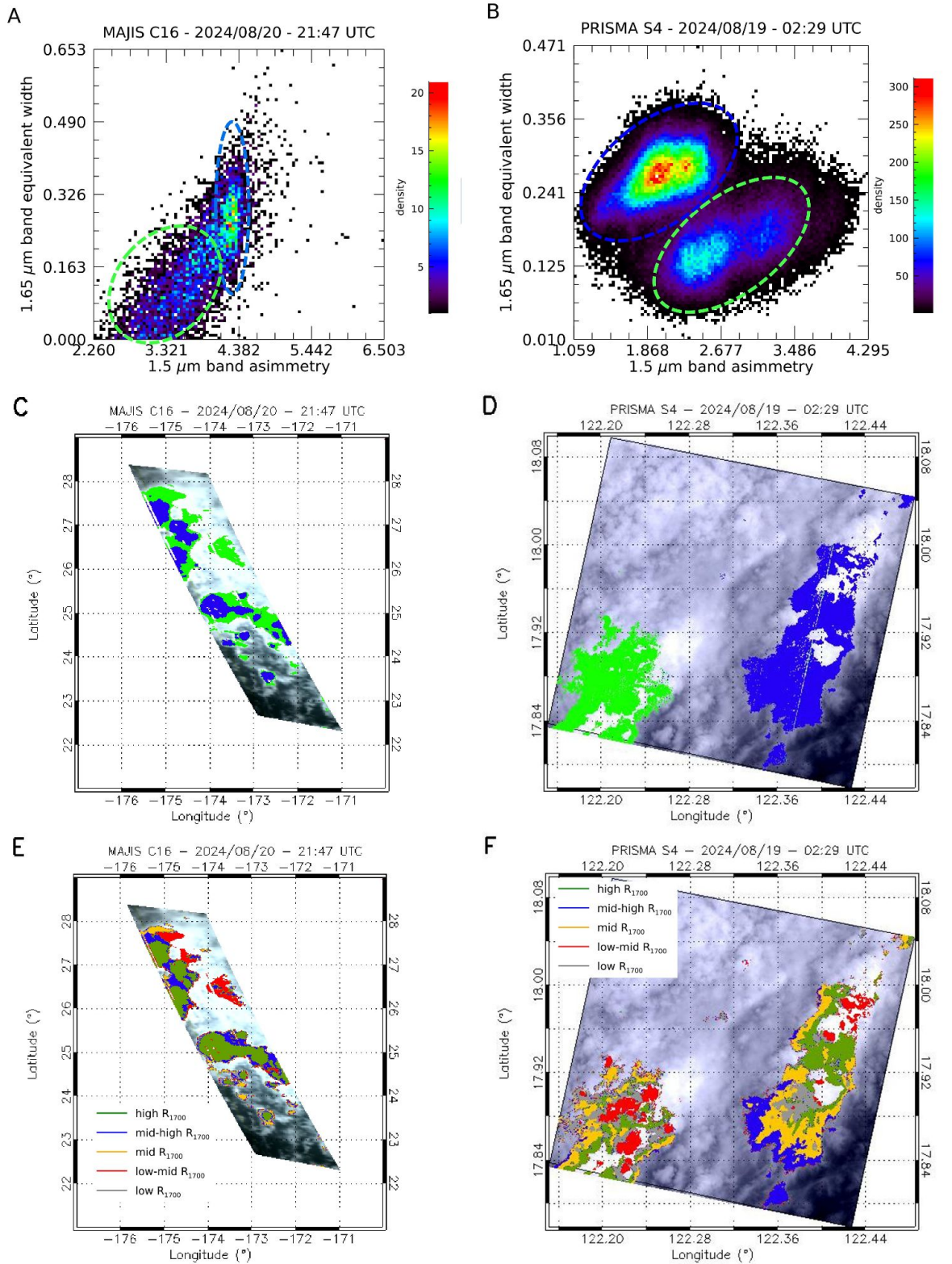
726

727

728 **Figure 11:** Panels A and B refer to MAJIS cube C7 and one of the PRISMA cubes from
 729 session 07, respectively, displayed in RGB. Panels C and D show the masks for the
 730 detection of ocean (blue), liquid water clouds (cyan, from the “cloudy” condition in Table 3)
 731 and ice clouds (white) pixels related to the two cubes. Panels E and F display sample
 732 spectra related to the different classes identified in MAJIS and PRISMA observations.

733

734 Ice is similarly widespread in other MAJIS and PRISMA data, so that some considerations
 735 on its distribution and correlations of its parameters can be made (Figure 12). We compute
 736 the 1500 nm band asymmetry as a ratio of slopes, the first considered between 1415 and
 737 1500 nm (left wing) and the second between 1500 and 1790 nm (right wing). The asymmetry
 738 correlates with the strength of the 1650nm band (quantified as equivalent width, Figure 12A
 739 and B), with higher values indicating increasingly crystalline ice (Mastrapa, 2008; Stephan et
 740 al. 2021; Grundy & Schmitt 1998). Different regimes of these two parameters map localized
 741 structures in MAJIS and PRISMA observations, as shown in Figure 12C and D respectively
 742 where green and blue pixels refer to clusters contained within dashed ellipses sharing the
 743 same color in Figure 12A and B. In MAJIS case, the blue cluster is characterized by an
 744 increasing 1650 nm equivalent width at constant 1500 nm band asymmetry. The green
 745 cluster, instead, shows a common trend of growth for the two parameters. On the other
 746 hand, the PRISMA ellipses identify well separated clusters of points within the two
 747 parameters’ space.



748

749

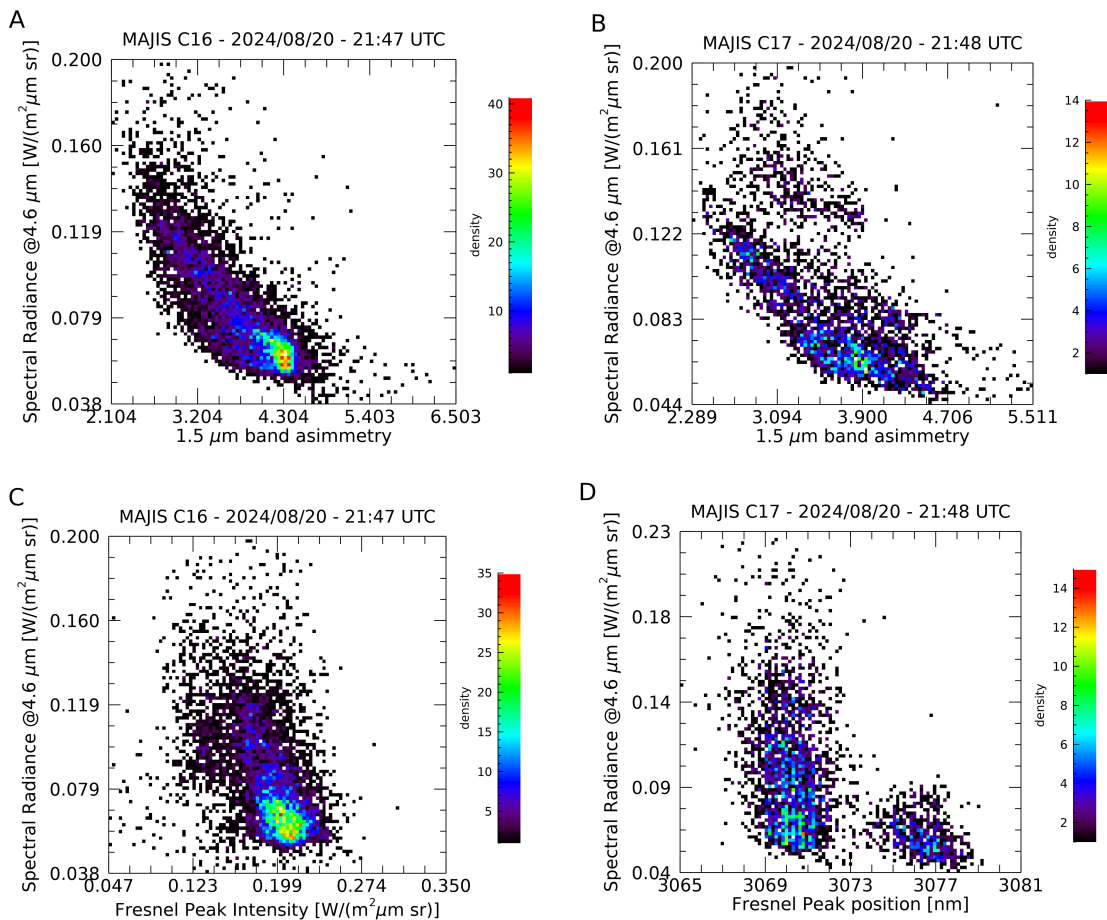
750 Figure 12: **A-B**: scatterplots of the 1500 nm band asymmetry and the 1650 nm band
 751 equivalent width for MAJIS reflectance cube C16 and one of the PRISMA reflectance cubes
 752 from session 04. The colored-dashed ellipses separate different regimes of the two
 753 parameters (see Section 3.5). **C-D**: green and blue pixels map the clusters contained within
 754 the respective ellipses in panels A and B. **E-F**: clustering of ice observations, obtained

755 through the K-means classification algorithm (see Section 3.2), grouped on the basis of the
756 intensity of the reflectance at 1700 nm (R_{1700}).

757

758 It is interesting to note that the correlation between these clusters and those obtained from
759 the K-means classification discussed in Section 3.2 (Figure 12E-F) is not straightforward. For
760 MAJIS, ice spectra with high reflectivity in the solar part of the spectrum (green in Figure
761 12E) are mostly correlated with the blue cluster in Figure 12C. This trend is not observed in
762 PRISMA, where all K-means clusters are equally distributed over both the blue and green
763 clusters shown in Figure 12D, suggesting variable ice densities and grain sizes within the
764 same regimes of crystallinity. This difference derives from the fact that, as explained in
765 Section 3.2, for MAJIS the thermal wavelengths contribute to the K-means classification of
766 the spectra, hence providing information also on the temperature of the ice (see also Section
767 4.2.3). This is verified by the trend of the 1500 nm band asymmetry with the radiance in the
768 thermal part of the spectrum, shown for MAJIS cubes C16 and C17 in Figure 13A-B: more
769 crystalline ice (larger asymmetry) is correlated with lower radiances (i.e. temperatures) at
770 thermal wavelengths. In particular, orbit C17 also shows a detached cluster in the distribution
771 of the thermal radiance suggesting different regimes of temperature (hence different clouds'
772 altitude). Finally, we show the correlation between the ice crystallinity and its temperature in
773 Figure 13C-D, where the intensity and wavelength of the Fresnel peak are compared to
774 MAJIS thermal radiances. Consistently with previous studies (e.g. Stephan et al., 2021), the
775 intensity of Fresnel peak is higher when the temperature is low (Figure 13C), indicating
776 enhanced crystallinity (see also Poulet et al., this issue). The comparison in Figure 13D
777 shows two distinct regimes of the peak position, with the short wavelength cluster
778 characterized by a larger spread of the thermal radiance (suggesting an enhanced
779 temperature variability for a less crystalline ice, e.g. Stephan et al., 2021).

780



781

782

783 **Figure 13: A-B:** scatterplots of the 1500 nm band asymmetry and thermal radiances at 4600
 784 nm for MAJIS orbit C16 and C17 respectively. **C:** scatterplot of the Fresnel peak intensity
 785 with the thermal radiance at 4600 nm for MAJIS orbit C16. **D:** scatterplot of the Fresnel peak
 786 wavelength with the thermal radiance at 4600 nm for MAJIS orbit C17.

787

788 4.2. Clouds' altitude

789

790 We now discuss the altitudes of clouds derived with the different methods presented in
 791 Section 3.3.

792

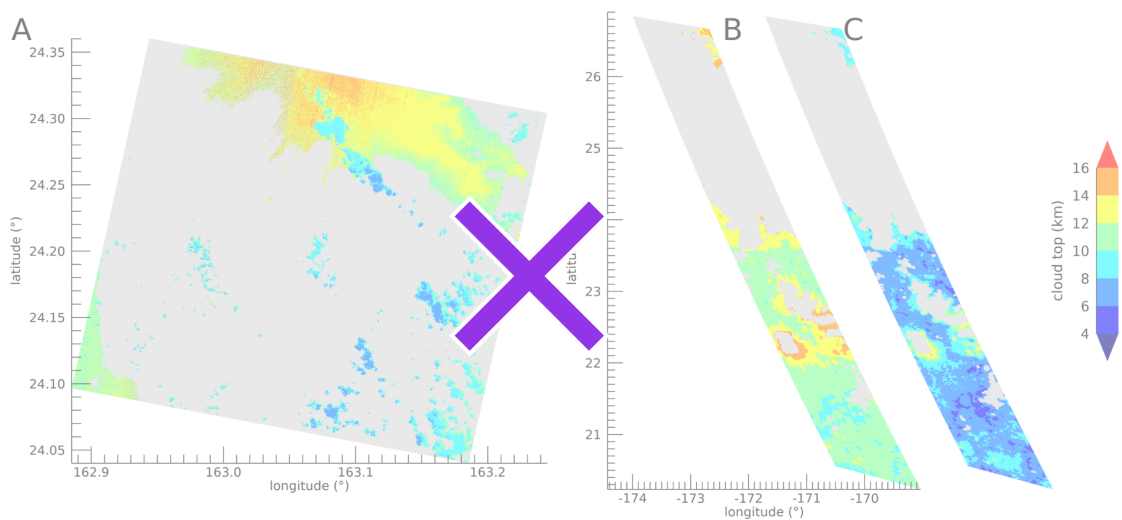
793 4.2.1. Altitudes from O₂ band depths

794

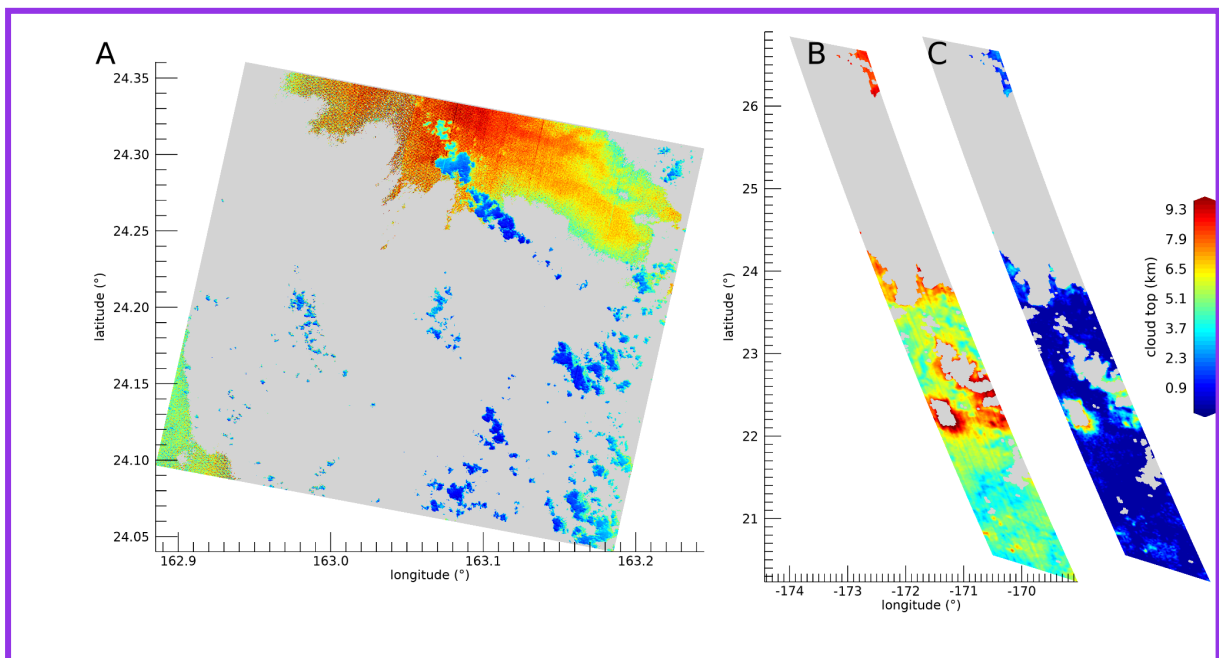
795 Figure 14 shows a comparison maps of cloud top altitude maps obtained applying the O₂
 796 bands' investigation method (Section 3.3.1) to both sample PRISMA and MAJIS cubes. In
 797 this case, PRISMA retrievals (Fig.14A) show two main cloud layers, a higher one between 5
 798 and 97 km (yellow-red colors in the figure, modal value 6.5±1 km) and a lower one between
 799 less than 1 and 43 km (blue-cyan colors, modal value 2.0±1 km). MAJIS cloud tops from O₂
 800 760 nm band (Fig.14B), whose model value lies at 4.8±1 km, are in overall agreement with
 801 the PRISMA upper cloud deck, Taking into account the uncertainties of both datasets, the
 802 majority of altitudes derived from the 760 nm band are in remarkable agreement between
 803 MAJIS (modal value of 11±1 km, Figure 14A) and PRISMA (modal value of 12.5±1.0 km,
 804 Figure 14B), even if the observing angles were very different in the two cases (>60° for
 805 MAJIS, ~12° for PRISMA). On the other hand, the population of lower clouds detected by

806 PRISMA A second lower-altitude population peaking at 9 km is only observed in PRISMA
 807 data, appearing broken in a series of as localized small structures that could remain
 808 unresolved if also present in the MAJIS scene (see Section 2.3.1). A more systematic
 809 discrepancy is obtained when comparing from cloud top altitudes retrieved through the 760
 810 nm and the 1270 nm bands (Fig.14C, shown as reference allowed for MAJIS data only),
 811 since the latter gives systematically lower values cloud tops (most clouds drop below 1.5 km
 812 altitude) whose modal value in MAJIS cube peaks as low as 7.2 ± 1.0 km. This discrepancy
 813 likely reflects the smaller sensitivity of is expected, as this band to higher is more sensitive to
 814 lower altitudes and the non optimal less reliable modeling assumptions already described in
 815 (Section 3.3.1.) and we are neglecting cloud top scattering properties in evaluating the
 816 reflectance in the bottom of the bands. However, such an issue can be resolved with a
 817 more complete proper radiative transfer modeling as suggested by the benchmark presented
 818 in Section 4.2.4.

819



820



821

822 Figure 14: **A**): Map of cloud top altitude retrieved through the O₂ 760 nm band in a PRISMA
823 sequence 09 cube (20240820234657). Non-cloudy pixels or saturated ones, *excluded from*
824 *the calculation*, are shown in grey. **B**): the same as panel A but from a MAJIS data cube
825 C17. **C**): cloud top map for the same data in panel B (offset for clarity) but retrieved from the
826 1270 nm O₂ band. Uncertainties are of the order of 1 km (Section 3.3.1).

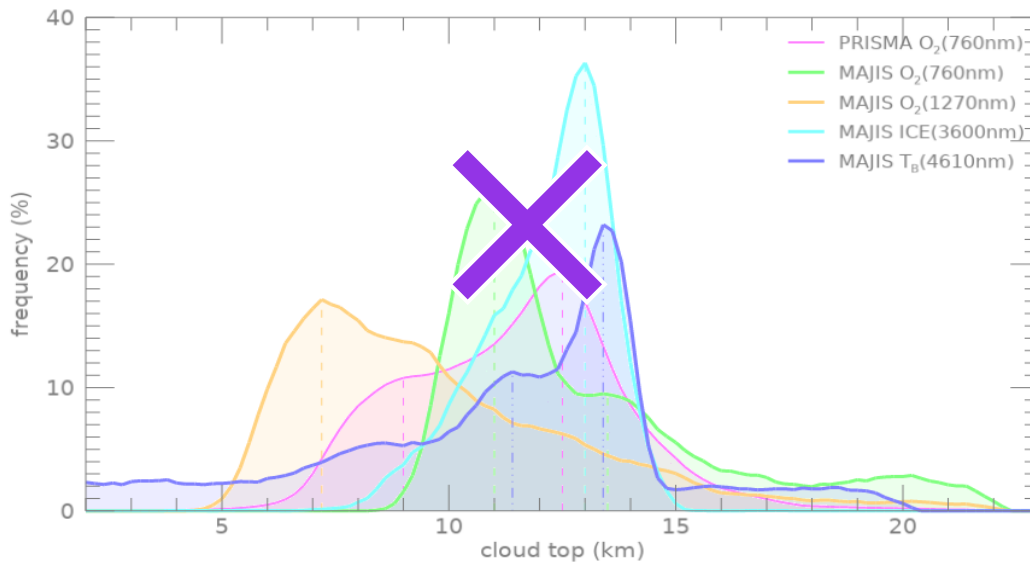
827

828 The ~~counts~~frequency distribution of ~~top~~ cloud ~~top~~ altitudes derived from the same maps in
829 Figure 14 is shown in Figure 15. The altitude ranges of the main cloud deck derived from
830 ~~the O₂ 760 nm band~~ are ~~provides altitudes~~ in good overall agreement between MAJIS and
831 PRISMA (light green and ~~dashed light red~~~~orange dashed magenta~~ curves), characterized by
832 two broad main peaks around 4.811 km and 6.513 km, respectively. ~~A population layered at~~
833 ~~4.5 km is also caught by the distribution of cloud top altitude derived from the 4610 nm~~
834 ~~thermal brightness (liquid water cloud curve in red layer~~ These are also the most frequent
835 altitude values suggested by the thermal emission at 4610 nm (blue curve in Figure 15). The
836 appearance of secondary peaks reflects intrinsic differences in the distribution of clouds in
837 the observed scenes. The displacement between these peaks of the green and blue curves
838 is mainly driven by ~~may reflect a true difference in the cloud populations between the two~~
839 observed scenes, and is further ~~can also be increased by the different spatial/spectral~~
840 resolutions and ~~explained by the expected due to different assumptions underlying the~~
841 ~~respective retrieval methods (e.g. for in the clouds' albedo and emissivity, see Sect.3.3) in~~
842 our qualitative estimate. A much lower distribution, flattened towards the surface, is indicated
843 by the O₂ 1270 nm band, confirming ~~its the scarce usability of this feature~~band to trace cloud
844 layers in a range of altitudes. The cloud heights derived from the 3700 nm ice spectral
845 signature ~~feature~~ (cyan curve) only trace icy pixels of MAJIS C17 cube (i.e., lower panels of
846 Figure 17) and are distributed ~~appear~~, as expected, ~~correctly located~~ above the main cloud
847 deck, with a ~~(peaking around 11 km)~~. The same behaviour ~~is~~ also confirmed by the
848 altitudes distribution of temperatures ~~evaluated through brightness temperatures' estimation~~
849 over the same icy spectra (blue curve, 10.5 km peak). It is worth stressing that the
850 distributions derived from O₂ bands and from ice features do not refer to exactly the same
851 set of spectra, since the signal of "icy spectra" is often saturated at visible wavelengths. The
852 same method, applied to ~~On the other hand, altitudes estimated from cloud temperatures in~~
853 non-icy spectra (red curve), gives altitudes ~~appear~~ significantly biased toward lower levels.
854 This can be mainly ascribed to the fact that the thermal part of the spectrum of thin liquid
855 water clouds observations is affected by an enhanced ~~increased~~ contribution from ~~of the~~
856 ocean thermal emission, ~~coming from the underlying ocean, which affects liquid clouds~~
857 ~~more than icy ones, statistically optically thicker~~. Full radiative transfer calculations would be
858 needed to quantitatively assess this aspect and the assumptions on the specific emissivity of
859 liquid/ice clouds (set to 1 for both in our calculations), but are not performed here as ~~this~~
860 ~~aspect~~ they are beyond the purpose of this preliminary work.

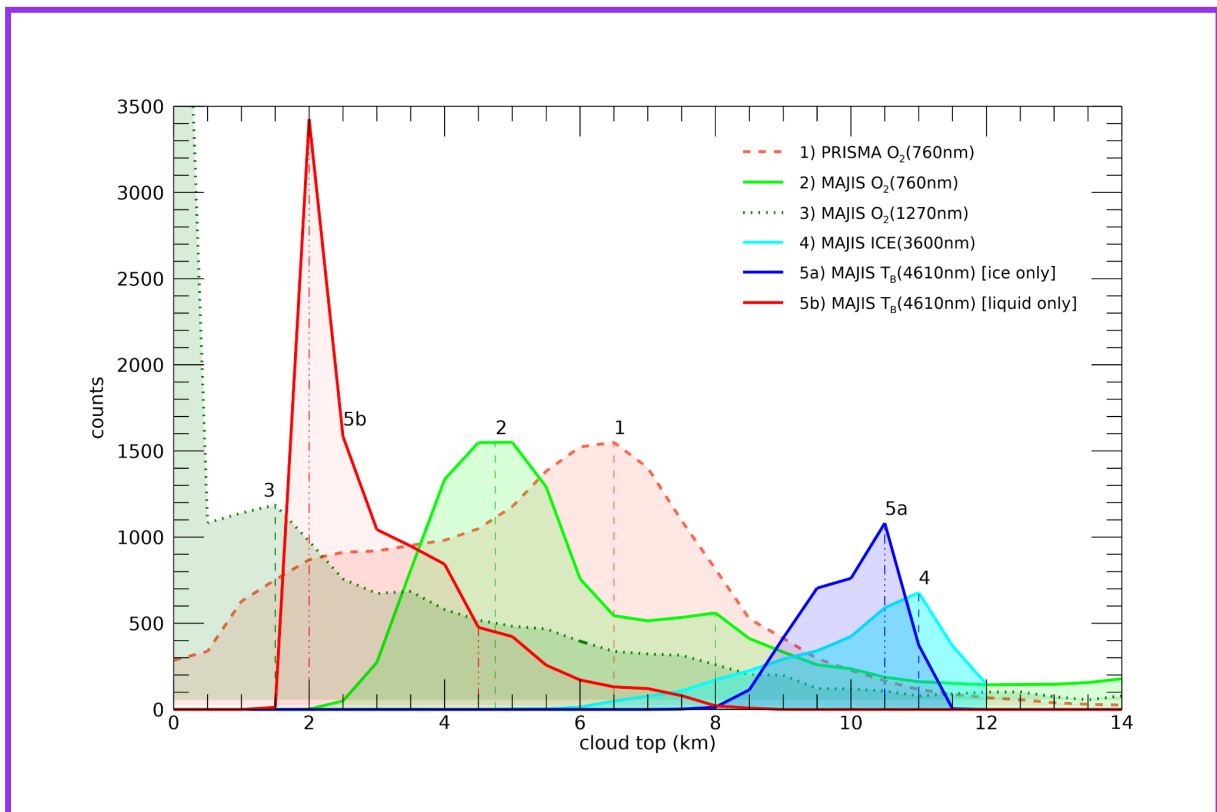
861

862 Indeed, the ~~adopted values of 1 for both quantities imply underestimation of clouds' altitudes~~
863 ~~from the 760 nm O₂ band depth, and overestimation from thermal brightness~~. This suggests
864 that, if proper radiative transfer modeling is considered, convergence of the peaks towards a
865 common regime is possibly achieved. A similar effect is observed in the distribution of
866 altitudes derived from the 1270 nm band depths, which are biased towards low values. The
867 ~~underestimation arising from the neglecting of scattering effects is magnified here, being the~~

868 band even weaker than the 760 nm one. Moreover, non-LTE emission also plays a
 869 non-negligible effect in this band, further biasing the derived altitudes (see Section 3.3.1).
 870 Finally, we compare these distributions with that deriving from the ice temperature estimation
 871 method (Figure 15 cyan curve, see Section 3.3.3). This provides results (discussed in detail
 872 in Section 4.2.3) which are consistent with the other curves and indicates that the altitudes
 873 identified in the peaks of all distributions are likely related to observations containing ice.



874
 875



876
 877

878 Figure 15: Comparison of cloud top altitudes retrieved from PRISMA and MAJIS session 09
 879 and C17 cubes respectively, through different methods. PRISMA counts are normalized to
 880 the maximum value of MAJIS curve 2. Distributions related to the maps in Figure 14A, B, C,
 881 derived from O₂ band depths, related to the maps in Figure 14A, B, C, are shown in pink
 882 (dashed line) magenta, light green (solid line), and dark green (dotted line) orange colors
 883 respectively. Cyan curve refers to ice clouds only (method described in Section 3.3.3 and
 884 discussed in Section 4.2.3), while the distributions obtained from thermal emission at 4610
 885 nm (for cloudy pixels only) are given separately for water ice (in blue) and liquid water (in
 886 red) pixels by the blue curve. The heights of the main distribution peaks are highlighted by
 887 vertical dashed lines. Even if the distributions are evaluated in 0.5 km altitude bins, an
 888 uncertainty of the order of 1 km must be considered.

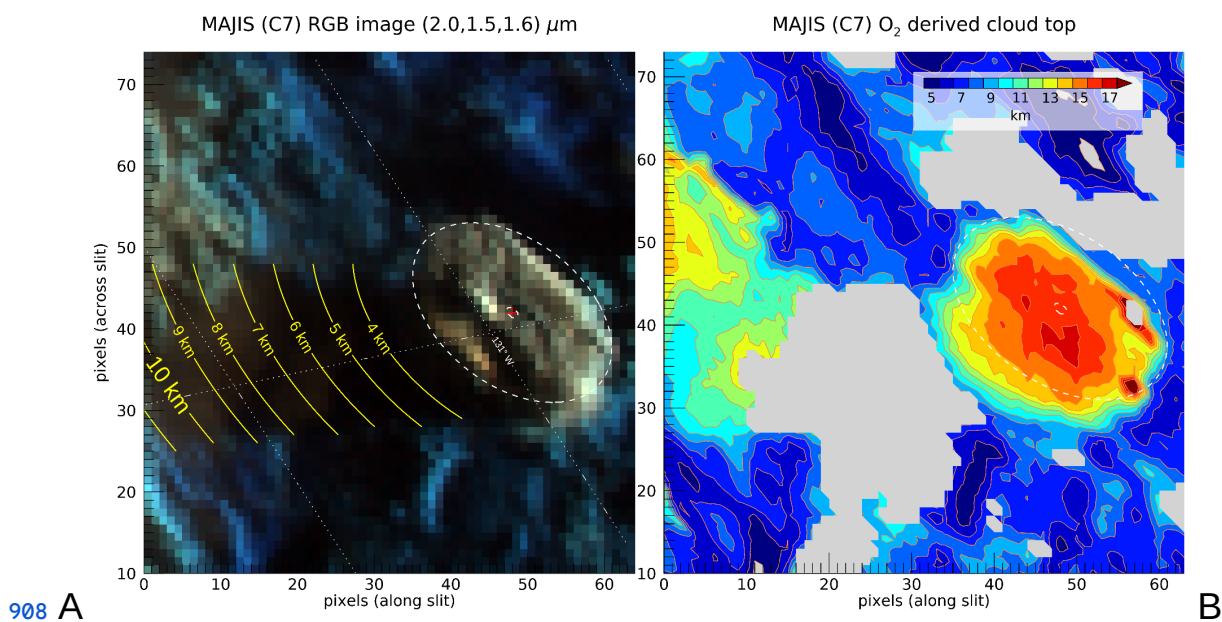
889

890

4.2.2. Altitudes from clouds' shadows

891

892 An example of the results obtained from the method described in Section 3.3.2 is given in
 893 Figure 16, where the shadows projected by high convective anvil clouds are clearly visible in
 894 MAJIS data cube C7. The grazing illumination of the scene (incidence angle ~80°) enables a
 895 vertical resolution of ~0.7 km, inferred from uncertainties of ~0.5° on incidence angles and
 896 2.7 km on shadow length (about twice the horizontal spatial resolution). Within this
 897 framework, the horizontal length of the shadow translates to a top altitude of about 10 km
 898 (see yellow lines). Of course this value is not absolute but only an estimate relative to the
 899 surrounding decks, whose altitudes can be qualitatively inferred through the estimation of the
 900 O₂ 760 nm band depth (see previous section). The O₂-derived elevations are shown in the
 901 map of Figure 16B, where the background structures appear to be located around 511 - 812
 902 km, while the anvil cloud top peaks at ~ 1621 km. This implies a differential height of ~ 10 km
 903 between the anvil and the surrounding clouds, in very good agreement with the estimated
 904 shadow length. Of course, the absolute height of the cloud top can only be derived if
 905 multiple scattering effects are accounted for in the reproduction of the 760 nm O₂ band.
 906 Nevertheless, the shadow analysis provides a quick and independent robust way for
 907 estimating the relative height of isolated structures with respect to their background.



909 Figure 16: A): Example of cloud top altitude estimation based on projected shadow length
 910 in the MAJIS data cube C7. The yellow isolines refer to cloud altitudes, while the white
 911 dashed line approximately indicates the approximate boundary of a detached cloud cloud
 912 boundaries (center indicated by the red dot). The yellow lines show how long the expected
 913 shadow would be in the actual geometry by changing the cloud top altitude. The shadow
 914 length observed in the background image matches a cloud about 10 km tall. B): Comparison
 915 with the cloud top altitudes retrieved in the same area from the O₂ 760 nm band (see
 916 Section 4.2.2), shown for comparison. Gray-filled patches correspond to areas where no O₂
 917 band is measurable. In both panels 'samples' indicate the spatial pixels in the slit, while
 918 'lines' refer to adjacent acquisitions of the slit in the cube.

919
 920
 921

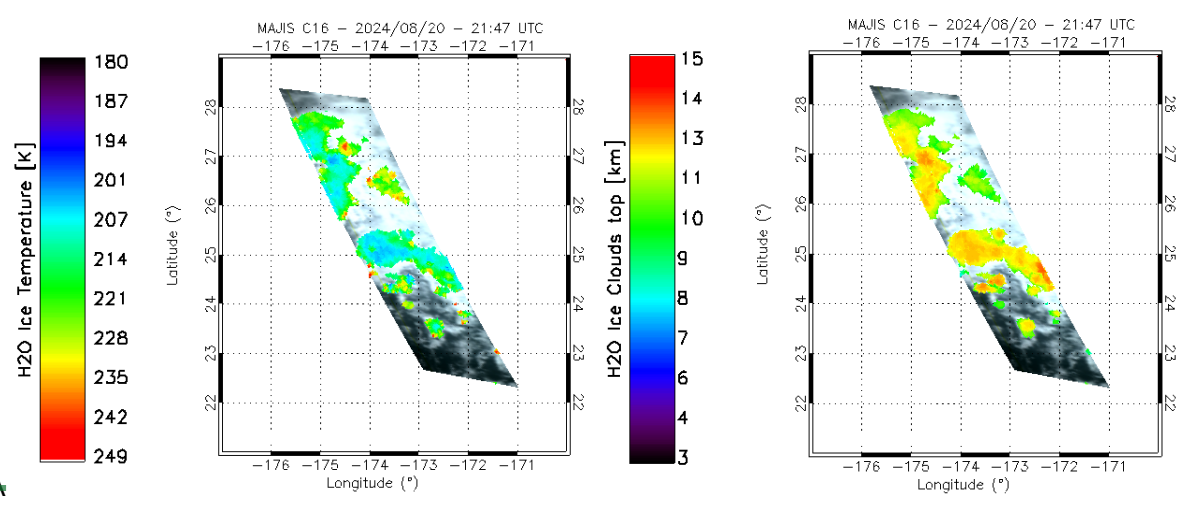
4.2.3. Altitudes from ice temperature

922 In Figure 17 we show two examples of the temperature and altitude maps derived with the
 923 method described in Section 3.3.3, for MAJIS cubes C16 (upper panel-A) and C17 (lower
 924 panel-B).

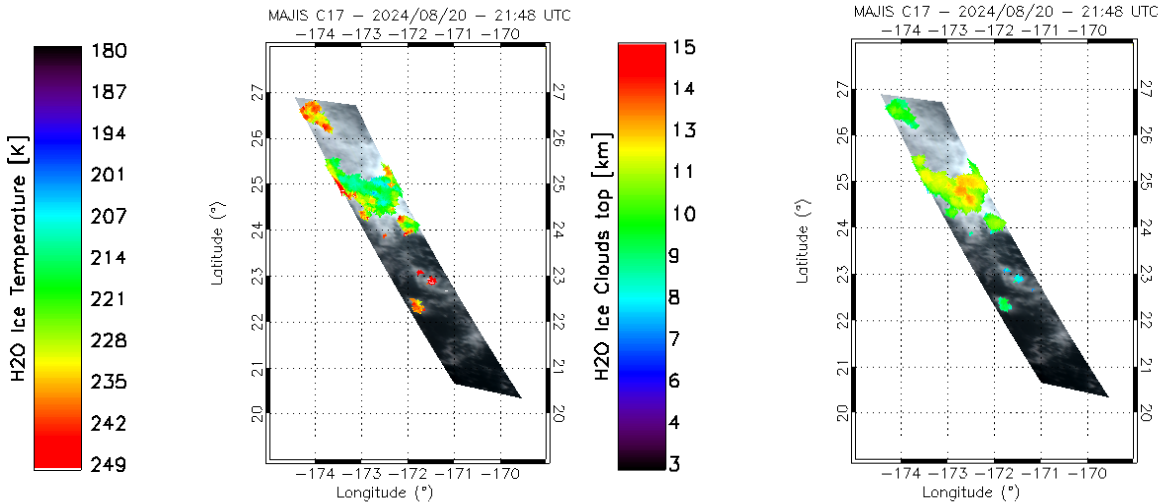
925 Altitudes are derived by assuming that the clouds are in thermal equilibrium with the
 926 surrounding air and reside within the troposphere, where the temperature vertical lapse rate
 927 is positive. Altitudes' errors are of about 1 km (Section 3.3.1) while those related to
 928 temperatures are propagated from the 3700 nm peak uncertainties (Table 4) and result of
 929 about 1 K. Orbit C16 (Figure 17A) shows two main decks, placed respectively at $z \sim 13$ km
 930 and $z \sim 10$ km which can be compared with the maps in Figure 12C and E, where the 1650
 931 nm band depth and K-means clusters are shown. The higher deck at $z \sim 13$ km correlates
 932 with the blue cluster in Figure 12C and the green one in Figure 12E, suggesting increased
 933 opacity and crystallinity at lower temperatures.

934 Similarly, two regimes of temperatures and altitudes are found in orbit C17, with higher
 935 clouds at $z \sim 13$ km ($T \sim 205$ K) and lower ones at $8 < z < 10$ km ($215 < T < 250$ K). As
 936 suggested by the scatterplot in Figure 13D, these two decks are characterized by different
 937 ice properties. Indeed, the short wavelength Fresnel peak cluster (i.e. reduced crystallinity,
 938 Cartwright et al., 2025) shows a larger spread of temperatures, consistent with the lower
 939 clouds discussed here. Instead, the long wavelength Fresnel peak cluster shows overall
 940 lower thermal radiances, and hence temperatures, in agreement with the higher clouds
 941 identified at ~ 13 km (see also Poulet et al., this issue).

942



943 A



944 **B**

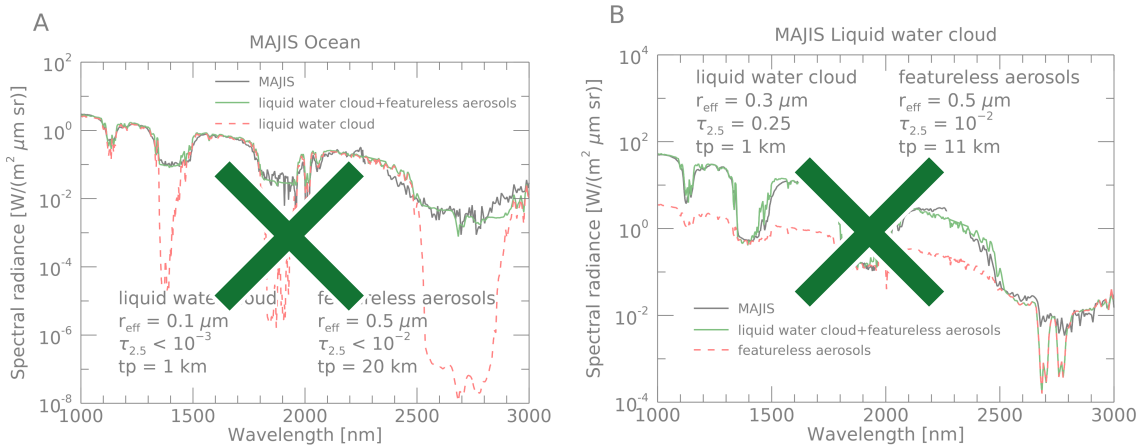
945 **Figure 17:** ice temperature (left) and inferred cloud altitude (right) mapped on MAJIS cube
 946 C16 (upper panels **A**) and C17 (lower panels **B**). Ice is identified with a threshold < 1 on the
 947 ice clouds condition in Table 3.

948

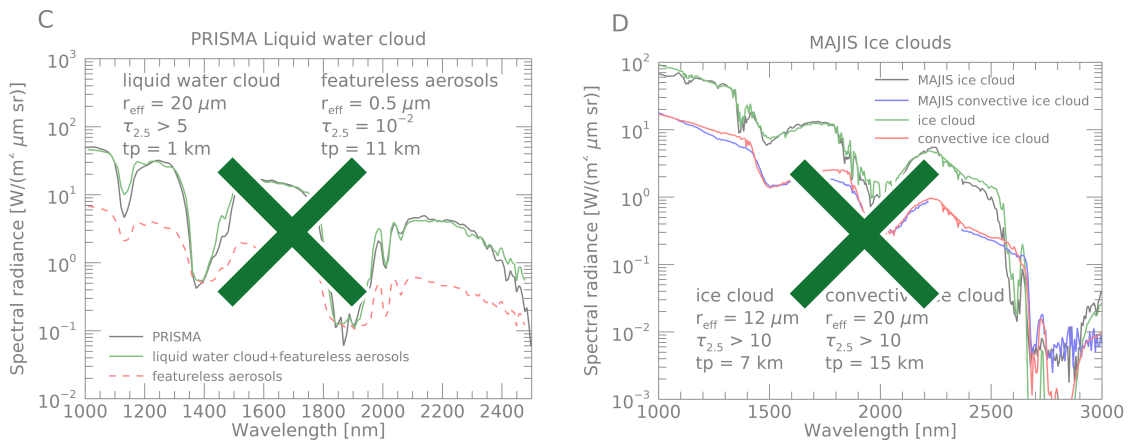
949 **4.2.4. Results from RT modeling**

950

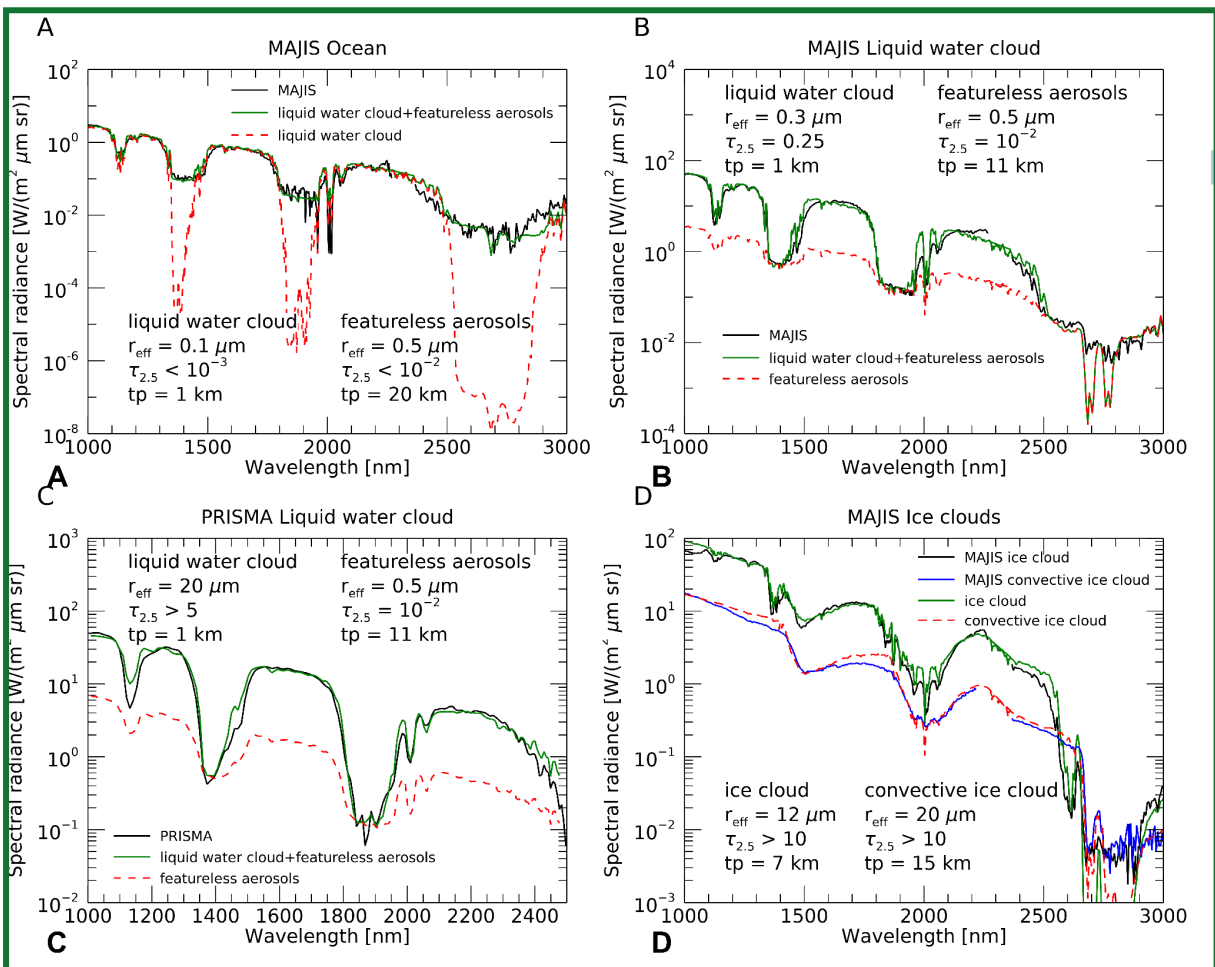
951 For our forward RT modeling (Section 3.3.4) we consider all MAJIS spectra and the PRISMA
 952 liquid water cloud one from Figure 3, as it is the one showing the most evident differences
 953 with respect to its MAJIS counterpart. We also take into account a MAJIS ice cloud spectrum
 954 related to one of the convective structures identified in Figure 11A-C and studied in Section
 955 4.2.2.



956



957



958

959 **Figure 18:** Panel A: MAJIS ocean spectrum from Figure 3 is shown in black, its forward RT
 960 fit is shown in green, while the contribution from the liquid water cloud in the simulation is
 961 given in dashed red. Geometrical and microphysical parameters (r_{eff} is the effective radius in
 962 μm , $\tau_{2.5}$ is the optical depth at $2.5 \mu\text{m}$ and tp is the cloud top in km) of aerosols involved in
 963 the fit are given in the figure. Panels B-C: same as in panel A, but liquid water clouds
 964 observations by MAJIS and PRISMA from Figure 3 are respectively fit. The dashed red lines
 965 here refer to the contribution from the featureless aerosols in the model (i.e. when no liquid
 966 water cloud is considered). D: MAJIS ice clouds forward RT fits (green and dashed red lines)
 967 related to MAJIS ice cloud spectrum from Figure 3 (black) and to a spectrum from the
 968 convective cloud identified in Figure 11C (blue line).

969

970 The best fits obtained with this approach are shown in Figure 18. In general, grain sizes and
971 clouds' altitudes determine the shape and the signal of water absorption bands, while the
972 number density can be tweaked to match the intensity of the continuum. We assume that the
973 clouds are compact in vertical extent and only occupy a single layer of the atmospheric
974 profile. The ocean and liquid water clouds observations require two separate layers placed
975 at different altitudes in the atmosphere (Figure 18A, B and C) suggesting that, as explained
976 in Sections 2.3.1 and 3.1, also the ocean spectra we are investigating are partially
977 obstructed by non-resolved cloudy structures. The lower layer shapes the shoulders of water
978 bands', in which the atmospheric transmission is enough to probe down to the surface, while
979 the upper one is needed to correctly model the intensity of the bands' bottom. Indeed, if
980 optically thick enough, high clouds prevent solar photons from reaching the underneath
981 atmospheric layers, hence reducing the gaseous absorption. Such a differential effect in the
982 models is shown as dashed red lines in Figure 18A, B, C. In the ocean spectrum (Figure
983 18A) the optically thin bottom layer ($z = 1$ km, $\tau < 10^{-3}$) with small grain sizes ($r_{\text{eff}} = 0.1$ μm) is
984 consistent with the average properties of maritime droplets ($0 < z < 2$ km, $5 \times 10^{-4} < \tau < 10^{-3}$,
985 $0.05 < r_{\text{eff}} < 1.5$ μm) commonly observed above the surface of the ocean (Croft et al., 2021;
986 Smirnov et al., 2002; Heintzenberg et al., 2000). On the other hand, the upper thin layer ($\tau <$
987 10^{-2}) has slightly larger particles ($r_{\text{eff}} = 0.5$ μm) and is placed at 20 km, in agreement with the
988 presence of stratospheric background aerosols ($15 < z < 25$ km, $10^{-4} < \tau < 10^{-3}$, $0.1 < r_{\text{eff}} < 1$
989 μm , Voudouri et al., 2023; Thomason et al., 2008). Such a configuration confirms the
990 observation as a partially obstructed scenario.

991 The selected MAJIS and PRISMA liquid water clouds observations (Figure 3 and Figure
992 18B-C) show a good radiometric agreement but differences in water bands' shape that can
993 be explained by changes in the aerosols' microphysical properties. Both observations are
994 characterized by a high altitude, spectrally featureless, thin aerosol layer ($z = 11$ km, $\tau \sim 10^{-2}$)
995 that is required to reproduce the bottom of water bands. This indicates the presence of faint
996 background stratospheric aerosols residing at the tropopause. Instead, the lower liquid water
997 layer ($z = 1$ km) is thin with small grains in the MAJIS case ($\tau = 0.25$, $r_{\text{eff}} = 0.3$ μm)
998 suggesting spray marine boundary layer aerosols (Sun et al., 2023; Zheng et al., 2018; Luo
999 et al., 2014), and thicker with large grains in the PRISMA case ($\tau > 5$, $r_{\text{eff}} = 20$ μm),
1000 consistent with the presence of stratus clouds (Fu et al., 2022; Rossow and Shiffer, 1999;
1001 LeMone, 1988). Hence, different properties ensure the modeling of flatter (MAJIS) and
1002 sharper (PRISMA) bands in the two observations.

1003 The two ice observations (Figure 18D) are reproduced with a single cloud layer and do not
1004 require the lower one. This is because the ice clouds in the models have opacities so high (τ
1005 > 10) that they prevent observing the ocean and the atmospheric layers in between. In such
1006 conditions, the ice cloud in practice acts as a surface with high albedo, accounting for most
1007 of the spectral features in the observations. However, two different clouds' observations are
1008 considered here. The first one (black line in Figure 18D) is related to a small structure
1009 identified around longitude 133° and latitude 22° in Figure 11C. This cloud can be modelled
1010 with ice crystals of the order of 10 μm in radius (green line). The altitude can be reliably
1011 tweaked by studying the depth of gaseous water absorption bands at 1380 nm and 2600 nm,
1012 both identifiable in the observation. This means that the ice cloud is low enough to ensure
1013 some water absorption, before completely shielding the underneath atmosphere. As a result,
1014 our estimate is that it has its top at 7 km. These parameters suggest compatibility with the
1015 presence of a thick cirrus cloud ($6 < z < 13$ km, $\tau > 3$, $10 < r_{\text{eff}} < 60$ μm , Baran, 2009; Zhou et
1016 al., 2017; LeMone, 1988).

1017 The other ice cloud (blue/cyan line in Figure 18D) is selected on the larger convective
 1018 structure identified in Figure 11C. We already expect this to be higher in the atmosphere with
 1019 respect to the other one (Section 4.2.2). Our model (dashed red line) suggests that it is
 1020 characterized by larger crystals (20 μm) and reaches an altitude of at least 15 km, enough to
 1021 prevent water absorption in the 1380 and 2600 nm bands (the model sensitivity to higher
 1022 altitudes is reduced making this estimate a lower limit). These values indicate that in this
 1023 observation MAJIS is probing the upper frozen top of a large convective cloud ($8 < z < 16$
 1024 km, $\tau > 10$, $10 < r_{\text{eff}} < 60 \mu\text{m}$, Dolan et al., 2023; Krishna et al., 2018; van Diedenhoven et al.,
 1025 2018).

1026

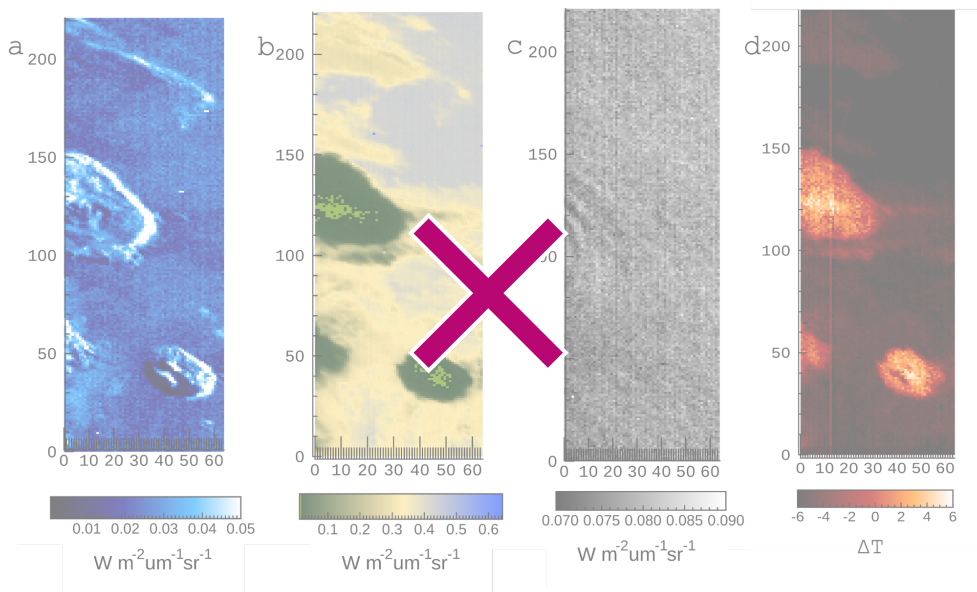
1027

1028 **4.3. Upper atmosphere features**

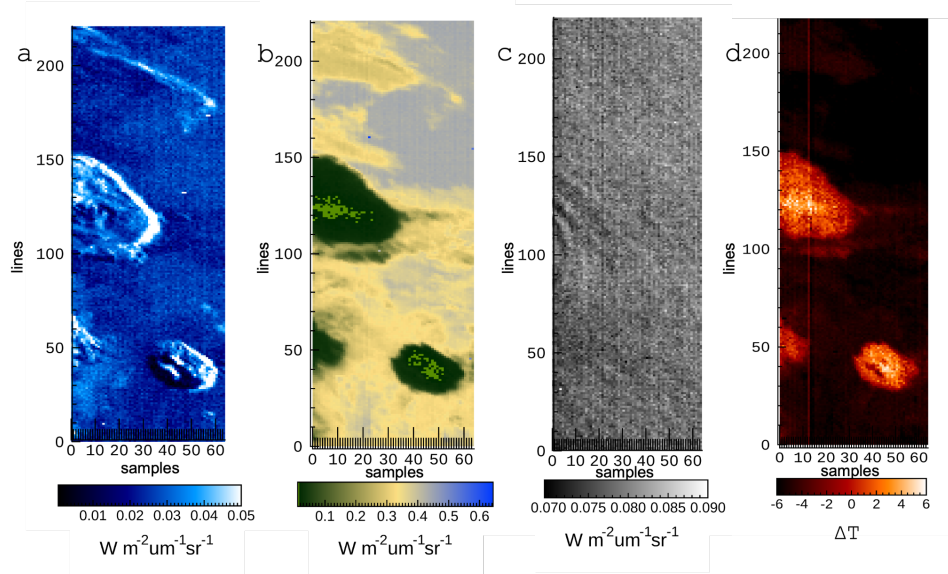
1029

1030 The CO_2 and O_3 emissions introduced in Section 3.4 have been studied in all MAJIS cubes,
 1031 deriving maps like those shown in the examples of Figure 19 and Figure 20. In Figure 19,
 1032 panels A and B show MAJIS cube C7 displayed at 3100 and 4512 nm, whose
 1033 anti-correlation highlights the presence of the convective clouds discussed in Sections 4.1,
 1034 4.2.2 and 4.2.4. Panels C and D, instead, show the radiance of the peak of CO_2 emission at
 1035 4270 nm and the brightness temperature difference between the O_3 emission peak and its
 1036 continuum (Section 3.4). It is evident how wavy patterns can be seen in the CO_2 map and
 1037 are uncorrelated with the clouds beneath. No wave patterns are spotted from the O_3
 1038 emission, whose positive values (and hence the emission) are only detectable above the
 1039 convective structures. This suggests that, while both phenomena are likely happening above
 1040 the clouds' top, waves are generated at different altitudes with respect to those pertaining to
 1041 the O_3 emission. However, the actual heights are not investigated here, since a rigorous
 1042 retrieval accounting for non-LTE effects (required for the assessment of these high-altitude
 1043 emissions) is beyond the scope of the paper.

1044



1045



1046

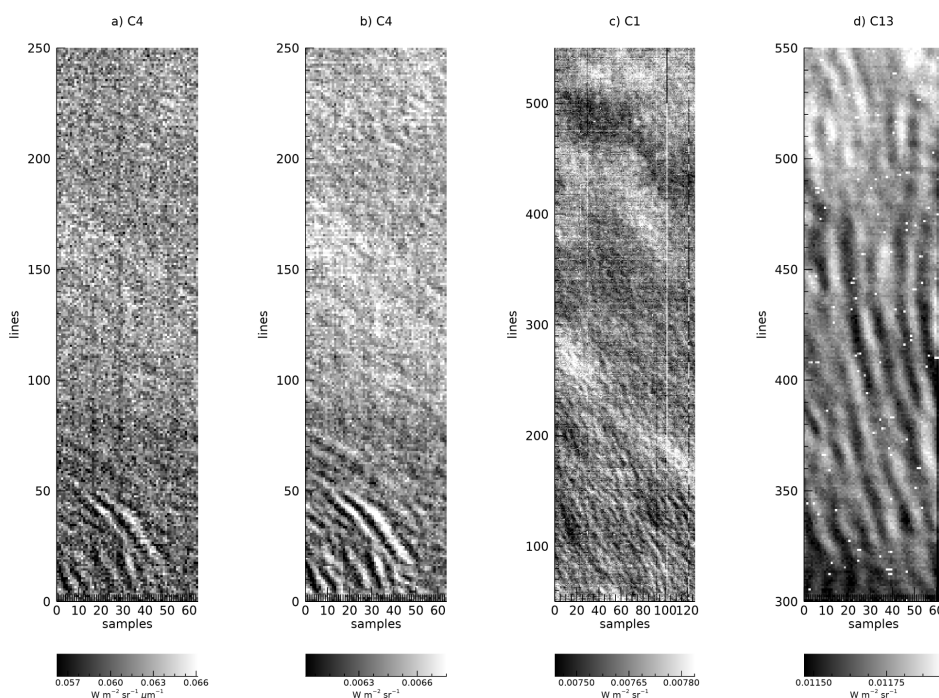
1047

1048 **Figure 19.** A-B: MAJIS cube C7 radiances at 3100 nm and 4512 nm respectively,
 1049 highlighting the anti-correlation between enhanced ice content (A, i.e. larger reflectances of
 1050 the Fresnel peak) and low thermal contribution (B). C: radiance of the CO₂ emission peak at
 1051 4270 nm, in which the gravity wave pattern is identified. D: brightness temperature difference
 1052 (in K) between the O₃ emission peak (4717 nm) and its continuum (4660 nm), showing
 1053 positive values above the clouds. In all maps, 'samples' and 'lines' indicate spatial pixel
 1054 numbers in the direction along and across the instrument slit respectively. ~~the spatial pixels~~
 1055 ~~in the slit, while 'lines' refer to adjacent acquisitions of the slit in the cube.~~ ~~the vertical axis~~
 1056 ~~indicates the number of lines while the horizontal axis indicates the number of samples.~~

1057

1058

1059



1060

1061 **Figure 20.** A circular wave pattern is clearly observed in MAJIS C4 cube at 4270 nm (panel
 1062 a). Panel b shows the enhanced contrast achievable after spectral integration between 4254
 1063 and 4333 nm, which also improves detection of complex wave patterns in several MAJIS
 1064 observations, like in C1 (panel c) and C13 (panel d). Pixel scales are reported in Table 1.

1065

1066 Following the discussion in Section 3.4, in Figure 20 we show the effect of the increased
 1067 contrast that can be achieved through the spectral integration of the CO₂ emission (right
 1068 panel), with respect to the single wavelength investigation (left panel). The integration of
 1069 ~~of course~~ reduces noise hence allowing enhanced accuracy in detecting the wave patterns.
 1070 Indeed, if the radiance integrated in the band is considered, the detectable relative intensity
 1071 drops from 1% to about 0.5%, which ~~of course~~ translates as an **increased/enhanced**
 1072 capability in characterizing the vertical structure of the waves.

1073

1074 4.3.1. Atmospheric waves properties

1075

1076 Examples of wavy structures identified in the MAJIS images at 4270 nm are provided in
 1077 Figure 20. The wave packets have characteristics different from one image to the other in
 1078 terms of orientations and horizontal wavelengths. In some cases, a curved wavefront is
 1079 observed (see Figure 20 B, C, D) as well as a superposition between different packets
 1080 (Figure 20 D).

1081

1082

ID	Latitude (deg)	Packet length (km)	Packet width (km)	Horizontal wvl (km)	Azimuth (deg)
C1	9-10	157.6	36.1	27±7	163
C2	10-14	155	135.2	20±6	160
C4	20.85	107.9	94.7	21±6	162
C5	17.7-18.4	154.1	159.1	16±5	33.5
C6	22.9	74.5	94.8		133
C7	23.4-25.5	84.5	73.8	15±6	155
C13	19-22	134.6	88.1	24±8	123
C16	25-27	174.5	131	28±11	119

1083 **Table 5:** Summary of atmospheric waves parameters (packet length and λ width, horizontal
 1084 wavelength and azimuth) calculated from MAJIS data analysis. Columns indicate: image cube,
 1085 latitude (deg), packet length (km), packet width (km), horizontal wavelength (km), azimuth (deg, see
 1086 Section 3.4.1), respectively.

1087

1088 The values obtained from the method described in Section 3.4.1 are provided in Table 5. In
 1089 the observed waves, the measured wavelengths are in the range ~ 15-40 km, which can be
 1090 considered as short wavelengths. Similar waves can be generated by several sources and
 1091 are usually observed in the stratosphere. According to models, deep convection is the
 1092 principal source of forcing (Fovell et al. 1992; Piani et al. 2000; Lane et al. 2001) and is also
 1093 suggested to be responsible for circular wave fronts (alongside isolated thunderstorm

1094 events, e.g. as observed from the Midcourse Space Experiment, Dewan et al. 1998).
1095 Another source of gravity waves, related to wind flow over mountains, is orography (Fritts
1096 and Alexander 2003; Kim et al. 2003). Depending on the topography, this can generate
1097 waves with horizontal scales from a few to hundreds of kilometers (Nastrom and Fritts, 1992;
1098 Dornbrack et al. 2002; Eckermann et al. 2007). However, as the majority of MAJIS EGA
1099 observations occurred above open sea areas, a possible origin related to a thunderstorm
1100 seems to be more realistic.

1101 For circular waves, we estimate the packets' properties and the time of occurrence of the
1102 related thunderstorms (see Section 3.4.1). We assume storms occurring at an altitude of 15
1103 km and consider cubes C7 and C4 as examples. The minimum and maximum radii, along
1104 with the expansion speed and wavelength derived from the images, are as follows: for cube
1105 C7, these parameters are respectively 35 km, 50 km, about 45 km/h and 15 km; for cube C4
1106 they are, 20 km, 110 km, about 100 km/h and 20 km. In both cases, the
1107 thunderstorm-triggering events appear to occur approximately one hour before the
1108 corresponding observations. ~~From the images we obtain the minimum and maximum radii~~
1109 ~~(35 and 50 km for C7, 20 and 110 km for C4) and wavelengths of 15 and 20 km for C7 and~~
1110 ~~C4 respectively. The minimum/maximum radii and the wavelengths obtained from the~~
1111 ~~images are respectively 35, 50 and 15 km (cube C7) and 20, 110 and 20 km (cube C4). In~~
1112 ~~both cases, the thunderstorm triggering events result to be occurring about 1 h before the~~
1113 ~~respective observations.~~ This is compatible with the NASA Worldview archive, where several
1114 thunderstorms have been registered over the areas observed by MAJIS at around 05:00
1115 local time. In particular, the wave detection in MAJIS C4 acquisition is located about 80 km
1116 far from the coastline, and no significant orographic features are present along the apparent
1117 direction of propagation. For this detection, the hypothesis of thunderstorm-generated waves
1118 is also strengthened by the intense electrical activity confirmed in D'Aversa et al. (this issue),
1119 where a lightning event has been detected in the visible range of MAJIS cube C1 through
1120 the identification of neutral atomic oxygen and nitrogen emission lines.

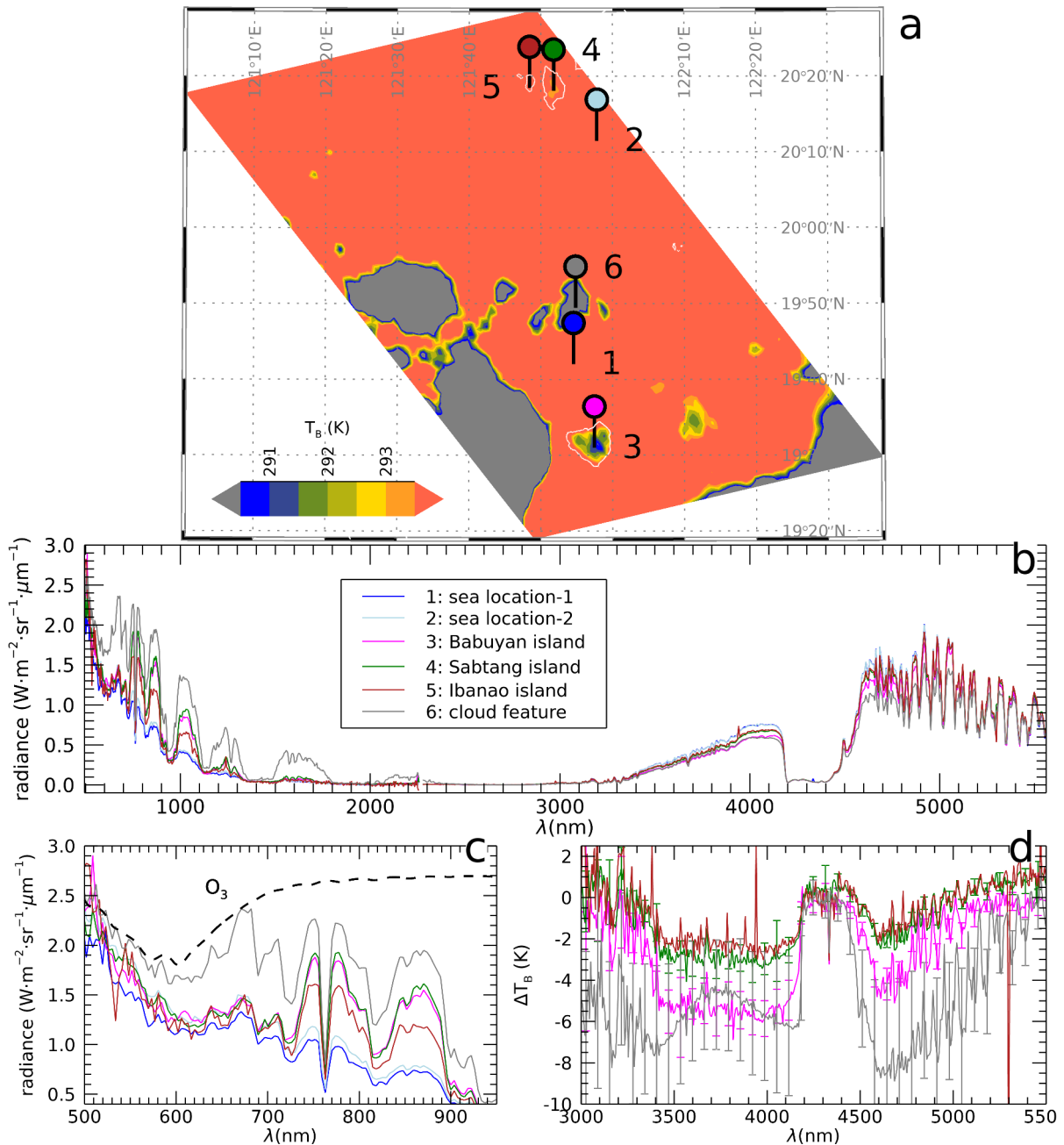
1121

1122 4.4. Land features

1123

1124 The land/ocean-contrast detection method described in Section 3.1 has been applied to all
1125 MAJIS cubes, but only a few land features have been identified. The C1 and C2 cubes,
1126 expected to cover large land areas at nighttime, encountered very thick and extended storm
1127 systems that prevented any surface visibility. Hence, all observable land regions consist of
1128 small islands seen in twilight illumination, colder than the surrounding sea surface but barely
1129 observable at visible wavelengths. Besides the largest example (Figure 7), other islands are
1130 found in the cube C5 (Figure 21): Babuyan (region 3), Sabtang (region 4), and the very small
1131 Ibahos island (about 4 x 2.5 km wide, region 5), all part of the Batanes archipelago. The
1132 nearby Dequey island, even smaller (~0.7x1 km), remains unresolved. With respect to the
1133 ocean, the brightness temperatures measured over land and cloud areas (Figure 21b) are
1134 colder, with differences up to ~6 K and ~8 K respectively. Even if fully located beyond the
1135 terminator (solar incidence angle ~90.8°), a significant signal is detectable also at visible
1136 wavelengths, ascribable to light scattering in the upper illuminated portion of the atmospheric
1137 column, and to multiple scattering effects in the lower part.

1138

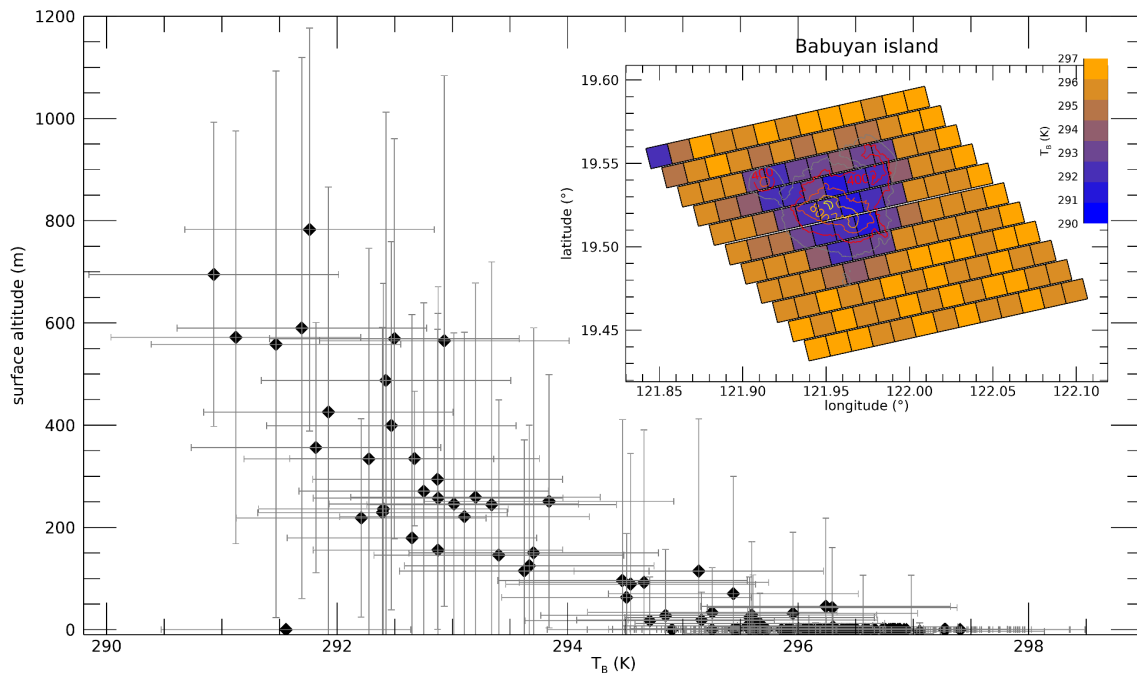


1139

1140 Figure 21: Land spectral features seen in twilight conditions in the MAJIS cube C5. **a)**
 1141 Regions of interest (ROIs, labeled 1 to 6) are selected over a 4610 nm **b)** Brightness
 1142 temperature map. The coldest areas (in gray) are (at 4610 nm) showing colder regions,
 1143 identifiable as thick clouds, while land areas are slightly warmer (grey areas and region 6)
 1144 and small islands: islands of Babuyan, (region 3), Sabtang (region 4) and Ibahos, (region 3,
 1145 4, 5 respectively), but still colder than the surrounding ocean (red-orange area). Coastlines,
 1146 obtained from OpenStreetMap under the Open Database License, are shown as white lines.
 1147 Points labeled 1 and 2 represent the locations for reference ocean spectra. **b)** MAJIS
 1148 full-range spectra over the ROIs selected regions. **c)** Blow-up of the visible spectral part,
 1149 showing H_2O and O_2 absorption bands as well as a broad O_3 absorption (see also Figure 4).
 1150 **d)** Blow-up of the infrared spectral part given as T_B difference with respect to the ocean
 1151 spectrum. Coastlines data from OpenStreetMap, available under the Open Database
 1152 License.

1153

1154 The MAJIS sensitivity to temperature variations can be estimated from the signal fluctuations
1155 over cloud-free ocean regions. The resulting uncertainties in thermal brightness (at 4610 nm)
1156 vary between 0.5 and 1 K, which correspond to about 0.2% and 0.4% of the ~~spectral~~
1157 radiance at 293K. This sensitivity appears sufficient to discriminate significant temperature
1158 variation not only between sea and land surfaces but also between different land regions. As
1159 an example, we show in Figure 22 the variability of MAJIS brightness temperature inside the
1160 Babuyan island, which hosts a volcano of about 1 km in elevation (Babuyan Claro Volcano).
1161 Even if the spatial resolution is limited, a clear trend emerges with respect to the topographic
1162 altitude, suggesting that the MAJIS data are sensitive to the surface altimetric temperature
1163 change.



1164

1165 **Figure 22:** Thermal analysis of Babuyan island, as viewed in MAJIS data cube C5. The
1166 MAJIS-derived brightness temperature (at 4610 nm) is plotted against topographic altitude,
1167 stressing the detection of surface altimetric temperature change. Error bars on the x axis
1168 derived from signal fluctuation over sea surface around the island, while those on y axis
1169 represent the variability of surface altitude inside individual MAJIS pixels. Unit emissivity has
1170 been assumed everywhere. Topographic data are extracted from Google Earth Pro
1171 7.3.6.10441 (accessed September, 03, 2025).

1172

1173 5. Application to Jovian system science

1174

1175 This flyby represents the first acquisition of planetary data by MAJIS. Although the analysis
1176 presented here has been dedicated to Earth science, we can briefly identify and discuss
1177 different links to the MAJIS science that is foreseen at Jupiter and its icy satellites,
1178 highlighting the instrument capabilities in exploring different objects of the solar system.

1179

1180 5.1. From ice clouds to icy surfaces

1181

1182 The detection of terrestrial ice clouds described in Section 4.1 represents the first spectral
1183 observations of water ice performed by MAJIS, and is therefore the first approach to
1184 establish the potential outcomes from observations of Jovian icy satellites, in particular for
1185 Callisto and Ganymede.

1186 The investigation of ice properties possibly provides information on the differential evolution
1187 these bodies underwent in the Jovian system environment. For example, Callisto's surface is
1188 mainly covered by crystalline ice, while significant amorphous ice patches have been
1189 observed on Ganymede (e.g. Tosi et al., 2024, Bockelée-Morvan et al., 2024; Cartwright et
1190 al., 2024). These regions could indicate alteration through radiolysis induced by the
1191 impinging of charged particles on the ice (Khurana et al., 2007), hence providing information
1192 on the mechanisms connecting Jupiter's magnetic field lines and the moons' surfaces.
1193 Moreover, while Callisto is characterized by an overall low ice content on the surface (~
1194 50%) and presents a more ancient and stable scenario (Greeley et al., 2007), Ganymede's
1195 fresh ice patches are indicative of more frequent ice resurfacing and cryo-volcanism events
1196 (Ligier et al., 2019). Smaller ice crystals are observed at the poles, matching the distribution
1197 of the fresher ice deposits and hence acting as a tracer of geologic activity. In this view, the
1198 investigation of ice-related spectral parameters can be used to address many scientific goals
1199 of the JUICE mission (Stephan et al., 2021a; Poulet et al., 2024a).

1200

1201 **5.2. Clouds**

1202

1203 Jupiter's atmosphere is thought to be dominated by the presence of three main cloud decks
1204 residing at different altitudes and mixed by convective processes and atmospheric circulation
1205 (Fletcher et al., 2023). From lower to higher heights these are respectively composed of a
1206 H₂O-NH₃ liquid solution, NH₄SH solid aggregates, and NH₃ ice crystals (Atreya et al., 1999).
1207 In particular, the NH₄SH and NH₃ clouds can be responsible for the chromatic differences in
1208 Jupiter's dark "belts" and bright "zones". Above these structures, hazes composed of
1209 products of the photochemical disruption of CH₄ and NH₃ extend from the upper troposphere
1210 to the stratosphere (e.g. Sindoni et al., 2017; Biagiotti et al., 2025). Such cloud complexity is
1211 not present in Earth's atmosphere where water is the only condensable, aside from a variety
1212 of aerosols of different origin (e.g. maritime, volcanic, smog, stratospheric). Nevertheless,
1213 the study of EGA observations allows a first MAJIS data analysis devoted to disentangling
1214 the spectral information related to different sources, like gases, clouds and, in this case, also
1215 surfaces. In this manuscript we have investigated clouds under different points of view,
1216 including their detection, water vapour phase identification, vertical structure assessment,
1217 and microphysical properties estimation. All these techniques are applicable to Jupiter once
1218 adapted to the different composition and structure of the giant planet. For example, the RT
1219 modeling presented in Section 4.2.4 only dealt with the solar part of the spectrum, which
1220 would only allow the investigation of Jupiter's hazes and the NH₃ deck (e.g. the recent work
1221 of Biagiotti et al., 2025 on JUNO/Jiram data). The exploitation of the full MAJIS spectral
1222 range, including thermal wavelengths, is instead mandatory for characterizing the deeper
1223 NH₄SH (Grassi et al., 2021) and H₂O (Bjoraker et al., 2022) clouds, especially in "hot spot"
1224 regions.

1225 The shadow technique for measuring cloud heights, commonly applied in planetary
1226 high-resolution imaging analysis, is also applicable to Jupiter (e.g. Orton et al., 2017). For
1227 instance, in observations acquired at the bottom of methane bands, Simon et al. (2015) were
1228 able to measure shadows 45 km long, revealing wavy structures less than 1 km in amplitude.
1229 In principle, MAJIS observations of Jupiter atmosphere will allow the application of this

1230 technique to limited cases, mostly near the terminator and in polar regions when observed
1231 from perijove. Maximum spatial resolutions of ~ 120 km/px achievable in these conditions
1232 may enable detecting shadows related to vertical displacements of the order of 10 km.

1233

1234

1235 **5.3. High-altitude emissions**

1236

1237 The use of chemical atmospheric species as tracers for the atmospheric circulation,
1238 including wind measurements and wave detections, is widely applied to the investigation of
1239 both terrestrial (i.e. Hueso et al. 2008; Peralta et al. 2008) and giant planets (i.e.
1240 Müller-Wodarg et al. 2019, Grassi et al., 2020). A similar approach is valid for the upcoming
1241 MAJIS measurements at the Jovian system, whose upper atmospheric dynamical structure
1242 can be investigated through the monitoring of the distribution (in latitude and local time) of
1243 minor widespread species like H_3^+ and hydrocarbons deriving from the photolysis of methane
1244 (see Miller et al. 2020 for a thorough review) as demonstrated from both ground-based (see
1245 for example O'Donoghue et al. 2016) and space-based data analyses (e.g. Moriconi et al.
1246 2020). MAJIS IR channel will allow to spectrally discriminate the CH_4 and H_3^+ contributions in
1247 the range 3000 - 4000 nm, where the two species present strong features (Castagnoli et al.,
1248 2025) identifiable within the fundamental 3300 nm CH_4 absorption band, similarly to the case
1249 of the 4300 nm CO_2 band in Earth's atmosphere (see Section 4.3). The study of CH_4 and H_3^+
1250 (e.g. JWST data analysis, Melin et al., 2024) will give access to upper atmospheric layers
1251 which are hardly probed otherwise. Altitudes from about 200 km above the 1-bar level are
1252 typical of methane emission peak, while above 500 km the H_3^+ emission seems to dominate,
1253 as also shown by recent analyses of JIRAM-Juno data (Migliorini et al. 2023), where the two
1254 species have been spatially separated.

1255

1256 **6. Summary and conclusions**

1257

1258 In this work we compare the observations of the MAJIS spectrometer on board the JUICE
1259 spacecraft, acquired during the Earth gravity assist of 2024 (Section 1), with those registered
1260 by the Italian Space Agency-led PRISMA spectrometer (Section 2). While no exact
1261 temporal-spatial coincidence could be achieved, the comparison allowed testing MAJIS
1262 spectral and radiometric response over ocean and clouds, the main targets observed during
1263 this flyby. Clouds observations have been analyzed for the estimation of altitudes and
1264 microphysical properties exploiting different methods (Section 4.2). Ice has been detected in
1265 most of the observations, allowing a first benchmark of the study of its spectral properties
1266 (Section 4.1) in view of Jupiter's icy satellites' exploration.

1267 High-altitude emissions from CO_2 and O_3 are also observed in MAJIS dataset, revealing the
1268 presence of a significant number of atmospheric gravity waves, whose properties have been
1269 derived (Section 4.3).

1270 While we discuss *ad hoc* spectral indices for the identification at VIS-NIR wavelengths of
1271 different types of surfaces (in view of the next JUICE Earth flyby happening in September
1272 2026) our investigation of land features is limited to the land/ocean temperature contrast or
1273 to the changing surface altimetry (Section 4.4). Indeed, in the MAJIS 2024 EGA data no land
1274 areas have been captured in daylight.

1275 This wide variety of scientific applications is finally put in the context of the Jupiter case,
1276 taking into account the differences between our planet and the gaseous giant's atmosphere
1277 and icy satellites (Section 5).

1278 In conclusion, EGA data provide the first scientific benchmark of MAJIS instrumental
1279 response in a planetary environment, and give the first glimpse of the amount and quality of
1280 spectral information we can expect in the Jovian system.

1281

1282 Author Contributions

1283 Conceptualization, F.O., E.D., A.Mi.; formal analysis, F.O., E.D., A.Mi.; Data Curation, F.O.,
1284 E.D., A.Mi., F.P., Y.L., G.P., A.Z., M.G., E.L., G.S., C.P., S.R., B.S.; investigation, F.O., E.D.,
1285 A.Mi.; methodology, F.O., E.D., A.Mi.; software, F.O., E.D., A.Mi.; supervision, F.O., E.D.,
1286 A.Mi., G.P., F.P., Y.L., G.F., M.C., M.R., B.S., A.M., L.N.F., A.Z., M.G., E.L., G.S., C.P.;
1287 validation, F.O., E.D., A.Mi.; writing—original draft, F.O., E.D., A.Mi.; writing—review &
1288 editing, F.O., E.D., A.Mi., G.P., F.P., L.N.F., A.M.. All authors have read and agreed to this
1289 version of the manuscript.

1290 Code availability

1291 The codes used in this manuscript have been developed by the authors and are available on
1292 request.

1293 Competing interests

1294 The authors declare no competing interests in the production of this manuscript.

1295

1296 Acknowledgements & Data availability

1297

1298 JUICE is a mission under ESA leadership with contributions from its Member States, NASA,
1299 JAXA and the Israel Space Agency. It is the first Large-class mission in ESA's Cosmic Vision
1300 programme. The Italian participation in the JUICE mission is funded by the Italian Space
1301 Agency (ASI). In particular, this work has been developed under the ASI-INAF agreement n.
1302 2023-6-HH.0.

1303 The MAJIS data acquired during the JUICE Moon–Earth flyby in August 2024 are currently
1304 under the mission's cruise-phase proprietary period. These data will be made available
1305 through the ESA Planetary Science Archive following the first Cruise Archive Delivery, which
1306 is currently scheduled for six months after Earth Gravity Assist #3 in 2029.

1307 PRISMA products are generated by IAPS-INAF under a license from ASI Original PRISMA
1308 Product - © Italian Space Agency (ASI) – 2024. ASI retains copyright on the ORIGINAL
1309 Product “PRISMA Product - © Italian Space Agency (ASI) 2024. All rights reserved“.

1310

1311 References

1312

1313 Acton, C.H., 1996. Ancillary data services of NASA's navigation and ancillary infor-
1314 mation facility. *Planet. Space Sci.* 44 (1), 65–70.

1315

1316 Acton, C., Bachman, N., Semenov, B., & Wright, E. (2018). A look towards the future
1317 in the handling of space science mission geometry. *Planetary and Space Science*,
1318 150, 9–12. <https://doi.org/10.1016/j.pss.2017.02.013>

1319

1320 Alexander, M. J., and J. R. Holton. “A Model Study of Zonal Forcing in the Equatorial

1321 Stratosphere by Convectively Induced Gravity Waves.” *Journal of the Atmospheric*
1322 *Sciences* 54, no. 3 (1997): 408 - 419.
1323 [https://doi.org/10.1175/1520-0469\(1997\)054<0408:amsozf>2.0.co;2](https://doi.org/10.1175/1520-0469(1997)054<0408:amsozf>2.0.co;2).
1324
1325 Alexander, M. Joan, and Christopher Barnet. “Using Satellite Observations to
1326 Constrain Parameterizations of Gravity Wave Effects for Global Models.” *Journal of*
1327 *the Atmospheric Sciences* 64, no. 5 (2007): 1652 - 1665.
1328 <https://doi.org/10.1175/jas3897.1>.
1329
1330 Atreya, S.K., M.H. Wong, T.C. Owen, et al. “A Comparison of the Atmospheres of
1331 Jupiter and Saturn: Deep Atmospheric Composition, Cloud Structure, Vertical Mixing,
1332 and Origin.” *Planetary and Space Science* 47, nos. 10–11 (1999): 1243 - 1262.
1333 [https://doi.org/10.1016/s0032-0633\(99\)00047-1](https://doi.org/10.1016/s0032-0633(99)00047-1).
1334
1335 Baldrige, A.M., S.J. Hook, C.I. Grove, and G. Rivera. “The ASTER Spectral Library
1336 Version 2.0.” *Remote Sensing of Environment* 113, no. 4 (2009): 711 - 715.
1337 <https://doi.org/10.1016/j.rse.2008.11.007>.
1338
1339 Baran, Anthony J. “A Review of the Light Scattering Properties of Cirrus.” *Journal of*
1340 *Quantitative Spectroscopy and Radiative Transfer* 110, nos. 14–16 (2009): 1239 -
1341 1260. <https://doi.org/10.1016/j.jqsrt.2009.02.026>.
1342
1343 Bekki, S., and F. Lefevre. “Stratospheric Ozone: History and Concepts and
1344 Interactions with Climate.” *The European Physical Journal Conferences* 1 (2009): 113
1345 - 136. <https://doi.org/10.1140/epjconf/e2009-00914-y>.
1346
1347 ~~Berk, A., Conforti, P., Kennett, R., Perkins, T., Hawes, F., & van den Bosch, J. (2014).~~
1348 ~~MODTRAN6: a major upgrade of the MODTRAN radiative transfer code. Proc. SPIE~~
1349 ~~9088, Algorithms and Technologies for Multispectral, Hyperspectral, and Ultraspectral~~
1350 ~~Imagery XX, 90880H. doi:10.1117/12.2050433.~~
1351
1352 Biagiotti, F, D Grassi, G Liuzzi, et al. “Evidence of Pure Ammonia Clouds in Jupiter’s
1353 Northern Temperate Domain from Juno/JIRAM Infrared Spectral Data.” *Monthly*
1354 *Notices of the Royal Astronomical Society* 538, no. 3 (2025): 1535 - 1564.
1355 <https://doi.org/10.1093/mnras/staf381>.
1356
1357 Bjoraker, Gordon L., Michael H. Wong, Imke de Pater, Tilak Hewagama, and Máté

1358 Ádámkóvics. "The Spatial Variation of Water Clouds, NH₃, and H₂O on Jupiter Using
1359 Keck Data at 5 Microns." *Remote Sensing* 14, no. 18 (2022): 4567.
1360 <https://doi.org/10.3390/rs14184567>.
1361

1362 Bockelée-Morvan, D., et al., 2024. Composition and thermal properties of
1363 Ganymede's surface from JWST/NIRSpec and MIRI observations. *A&A*, 681.
1364

1365 Bovensmann, H., J. P. Burrows, M. Buchwitz, et al. "SCIAMACHY: Mission
1366 Objectives and Measurement Modes." *Journal of the Atmospheric Sciences* 56, no. 2
1367 (1999): 127 - 150.
1368 [https://doi.org/10.1175/1520-0469\(1999\)056<0127:smoamm>2.0.co;2](https://doi.org/10.1175/1520-0469(1999)056<0127:smoamm>2.0.co;2).
1369

1370 Butz, A., S. Guerlet, O. Hasekamp, et al. "Toward Accurate CO₂ and CH₄
1371 Observations from GOSAT." *Geophysical Research Letters* 38, no. 14 (2011).
1372 <https://doi.org/10.1029/2011gl047888>.
1373

1374 Cartwright, Richard J., Charles A. Hibbitts, Bryan J. Holler, et al. "Jwst Reveals
1375 Spectral Tracers of Recent Surface Modification on Europa." *The Planetary Science
1376 Journal* 6, no. 5 (2025): 125. <https://doi.org/10.3847/psj/adcab9>.
1377

1378 Cartwright, R.J., et al., 2025. Revealing Callisto's Carbon-rich Surface and CO₂
1379 Atmosphere with JWST. *Planetary Science Journal*, 5, 60.
1380

1381 Cassini, Lorenzo, Guido Masiello, Sergio De Souza-Machado, Manuel
1382 López-Puertas, Larrabee Strow, Giuliano Liuzzi, Christopher Hepplewhite, Tiziano
1383 Maestri, Michele Martinazzo, Carmine Serio, "Updates to 4.3um CO₂ NLTE modeling
1384 for nadir hyperspectral infrared sounders," Proc. SPIE 13668, Remote Sensing of
1385 Clouds and the Atmosphere XXX, 1366809 (29 October 2025);
1386 <https://doi.org/10.1117/12.3069902>
1387

1388 Castagnoli, Chiara, Bianca M. Dinelli, Francesca Altieri, et al. "Characterization and
1389 Sensitivity Analysis of JIRAM Spectra for Optimizing CH₄ and H₃⁺ Retrieval." *The
1390 Planetary Science Journal* 6, no. 4 (2025): 93. <https://doi.org/10.3847/psj/adbff8>.
1391

1392 Clark, Roger N., Dale P. Cruikshank, Ralf Jaumann, et al. "The Surface Composition
1393 of Iapetus: Mapping Results from Cassini VIMS." *Icarus* 218, no. 2 (2012): 831 - 860.
1394 <https://doi.org/10.1016/j.icarus.2012.01.008>.

1395
1396
1397
1398
1399
1400
1401
1402
1403
1404
1405
1406
1407
1408
1409
1410
1411
1412
1413
1414
1415
1416
1417
1418
1419
1420
1421
1422
1423
1424
1425
1426
1427
1428
1429
1430

Coradini, A., F. Capaccioni, P. Drossart, A. Semery, G. Arnold, and U. Schade.
"VIRTIS: The Imaging Spectrometer of the Rosetta Mission." *Advances in Space
Research* 24, no. 9 (1999): 1095 - 1104.
[https://doi.org/10.1016/s0273-1177\(99\)80203-8](https://doi.org/10.1016/s0273-1177(99)80203-8).

Cox, C., and Munk, W., "Measurement of the Roughness of the Sea Surface from
Photographs of the Sun's Glitter," *J. Opt. Soc. Am.* **44**, 838-850 (1954)
<https://doi.org/10.1364/JOSA.44.000838>

D'Aversa, Emiliano, Fabrizio Oliva, Francesca Altieri, et al. "Vertical Distribution of
Dust in the Martian Atmosphere: OMEGA/MEx Limb Observations." *Icarus* 371
(January 2022): 114702. <https://doi.org/10.1016/j.icarus.2021.114702>.

D'Aversa, E., et al.: Spectroscopic detection of terrestrial lightning from space by
JUICE-MAJIS during Earth Gravity Assist, *Ann. Geophys.*, submitted to this issue.

Dewan, E. M., and R. E. Good. "Saturation and the 'Universal' Spectrum for Vertical
Profiles of Horizontal Scalar Winds in the Atmosphere." *Journal of Geophysical
Research: Atmospheres* 91, no. D2 (1986): 2742 - 2748.
<https://doi.org/10.1029/jd091id02p02742>.

Dewan, E. M., R. H. Picard, R. R. O'Neil, et al. "MSX Satellite Observations of
Thunderstorm-generated Gravity Waves in Mid-wave Infrared Images of the Upper
Stratosphere." *Geophysical Research Letters* 25, no. 7 (1998): 939 - 942.
<https://doi.org/10.1029/98gl00640>.

Dolan, Brenda, Pavlos Kollias, Susan C. van den Heever, et al. "Time Resolved
Reflectivity Measurements of Convective Clouds." *Geophysical Research Letters* 50,
no. 22 (2023). <https://doi.org/10.1029/2023gl105723>.

Dörnbrack, Andreas, Thomas Birner, Andreas Fix, et al. "Evidence for Inertia Gravity
Waves Forming Polar Stratospheric Clouds over Scandinavia." *Journal of
Geophysical Research: Atmospheres* 107, no. D20 (2002).
<https://doi.org/10.1029/2001jd000452>.

1431 Drossart, Pierre, Giuseppe Piccioni, Angioletta Coradini, et al. "VIRTIS Imaging
1432 Spectrometer for the ESA/Venus Express Mission." *SPIE Proceedings* 5543
1433 (November 2004): 175. <https://doi.org/10.1117/12.557427>.
1434

1435 Eckermann, Stephen D., Jun Ma, Dong L. Wu, and Dave Broutman. "A
1436 Three-dimensional Mountain Wave Imaged in Satellite Radiance throughout the
1437 Stratosphere: Evidence of the Effects of Directional Wind Shear." *Quarterly Journal of*
1438 *the Royal Meteorological Society* 133, no. 629 (2007): 1959 - 1975.
1439 <https://doi.org/10.1002/qj.187>.
1440

1441 Efremenko, Dmitry, and Alexander Kokhanovsky. *Foundations of Atmospheric*
1442 *Remote Sensing*. Springer Nature, 2021.
1443

1444 Ehrlich, A., E. Bierwirth, M. Wendisch, et al. "Cloud Phase Identification of Arctic
1445 Boundary-Layer Clouds from Airborne Spectral Reflection Measurements: Test of
1446 Three Approaches." *Atmospheric Chemistry and Physics* 8, no. 24 (2008): 7493 -
1447 7505. <https://doi.org/10.5194/acp-8-7493-2008>.
1448

1449 Eldering, Annmarie, Thomas E. Taylor, Christopher W. O'Dell, and Ryan Pavlick.
1450 "The OCO-3 Mission: Measurement Objectives and Expected Performance Based on
1451 1 Year of Simulated Data." *Atmospheric Measurement Techniques* 12, no. 4 (2019):
1452 2341 - 2370. <https://doi.org/10.5194/amt-12-2341-2019>.
1453

1454 Filacchione, Gianrico, Emiliano D'Aversa, Fabrizio Capaccioni, et al. "Saturn's Icy
1455 Satellites Investigated by Cassini-VIMS. IV. Daytime Temperature Maps." *Icarus* 271
1456 (June 2016): 292 - 313. <https://doi.org/10.1016/j.icarus.2016.02.019>.
1457

1458 Filacchione, G., Capaccioni, F., Ciarniello, M., et al., 2012. Saturn's icy satellites and
1459 rings investigated by cassini-VIMS: III—Radial compositional variability. *Icarus*
1460 220, 1064–1096.
1461

1462 Fink, Uwe, and Harold P. Larson. "Temperature Dependence of the Water-Ice
1463 Spectrum between 1 and 4 Microns: Application to Europa, Ganymede and Saturn's
1464 Rings." *Icarus* 24, no. 4 (1975): 411 - 420.
1465 [https://doi.org/10.1016/0019-1035\(75\)90058-5](https://doi.org/10.1016/0019-1035(75)90058-5).
1466

1467 Fletcher, L.N., et al., 2023. Jupiter Science Enabled by ESA's Jupiter Icy Moons

1468 Explorer. *Space Science Review*, vol. 219, n. 53, 2023.

1469

1470 Fovell, R., D. Durran, and J. R. Holton. "Numerical Simulations of Convectively
1471 Generated Stratospheric Gravity Waves." *Journal of the Atmospheric Sciences* 49,
1472 no. 16 (1992): 1427 - 1442.
1473 [https://doi.org/10.1175/1520-0469\(1992\)049<1427:nsocgs>2.0.co;2](https://doi.org/10.1175/1520-0469(1992)049<1427:nsocgs>2.0.co;2).

1474

1475 Fritts, David C., and M. Joan Alexander. "Gravity Wave Dynamics and Effects in the
1476 Middle Atmosphere." *Reviews of Geophysics* 41, no. 1 (2003).
1477 <https://doi.org/10.1029/2001rg000106>.

1478

1479 Fu, Dongwei, Larry Di Girolamo, Robert M. Rauber, et al. "An Evaluation of the Liquid
1480 Cloud Droplet Effective Radius Derived from MODIS, Airborne Remote Sensing, and
1481 in Situ Measurements from CAMP2Ex." *Atmospheric Chemistry and Physics* 22, no.
1482 12 (2022): 8259 - 8285. <https://doi.org/10.5194/acp-22-8259-2022>.

1483

1484 Geddes, A., and H. Bösch. "Tropospheric Aerosol Profile Information from
1485 High-Resolution Oxygen A-Band Measurements from Space." *Atmospheric
1486 Measurement Techniques* 8, no. 2 (2015): 859 - 874.
1487 <https://doi.org/10.5194/amt-8-859-2015>.

1488

1489 Gordon, I.E., L.S. Rothman, R.J. Hargreaves, et al. "The HITRAN2020 Molecular
1490 Spectroscopic Database." *Journal of Quantitative Spectroscopy and Radiative
1491 Transfer* 277 (January 2022): 107949. <https://doi.org/10.1016/j.jqsrt.2021.107949>.

1492

1493 Gorshchev, V., A. Serdyuchenko, M. Weber, W. Chehade, and J. P. Burrows. "High
1494 Spectral Resolution Ozone Absorption Cross-Sections – Part 1: Measurements, Data
1495 Analysis and Comparison with Previous Measurements around 293 K." *Atmospheric
1496 Measurement Techniques* 7, no. 2 (2014): 609 - 624.
1497 <https://doi.org/10.5194/amt-7-609-2014>.

1498

1499

1500

1501 Grassi, Davide, A Mura, G Sindoni, et al. "On the Clouds and Ammonia in Jupiter's
1502 Upper Troposphere from Juno JIRAM Reflectivity Observations." *Monthly Notices of
1503 the Royal Astronomical Society* 503, no. 4 (2021): 4892 - 4907.
1504 <https://doi.org/10.1093/mnras/stab740>.

1505

1506 Grassi, D., et al., 2020. On the Spatial Distribution of Minor Species in Jupiter's
1507 Troposphere as Inferred From Juno JIRAM Data. *JGR Planets*, 125, 4.

1508

1509 Greeley, R., C.F. Chyba, J.W. Head III, W.B. McKinnon, R.T. Pappalardo, and P.H.
1510 Figueredo. "The Geology of Europa." In *Jupiter: The Planet, Satellites and*
1511 *Magnetosphere*, edited by F. Bagenal, T. Dowling, and W. McKinnon. Cambridge
1512 University Press, 2007.

1513

1514 Grundy, W. M., and B. Schmitt. "The Temperature-dependent Near-infrared
1515 Absorption Spectrum of Hexagonal H₂O Ice." *Journal of Geophysical Research:*
1516 *Planets* 103, no. E11 (1998): 25809 - 25822. <https://doi.org/10.1029/98je00738>.

1517

1518

1519 Guerlet, S., Lauzanne, N., Armante, R., Poulet, F., and Langevin, Y.: MAJIS/JUICE
1520 performances in the infrared during Earth fly-by: comparisons with IASI
1521 measurements and sensitivity to trace species, *Ann. Geophys.*, submitted to this
1522 issue.

1523

1524

1525 Haffoud, Paolo, François Poulet, Mathieu Vincendon, et al. "Calibration of MAJIS
1526 (Moons And Jupiter Imaging Spectrometer). III. Spectral Calibration." *Review of*
1527 *Scientific Instruments* 95, no. 3 (2024). <https://doi.org/10.1063/5.0188944>.

1528

1529 Hale, George M., and Marvin R. Query. "Optical Constants of Water in the 200 Nm to
1530 200 Mm Wavelength Region." *Applied Optics* 12, no. 3 (1973): 555.

1531 <https://doi.org/10.1364/ao.12.000555>.

1532

1533 Hamilton, Kevin. "Comprehensive Meteorological Modelling of the Middle
1534 Atmosphere: A Tutorial Review." *Journal of Atmospheric and Terrestrial Physics* 58,
1535 no. 14 (1996): 1591 - 1627. [https://doi.org/10.1016/0021-9169\(96\)00028-1](https://doi.org/10.1016/0021-9169(96)00028-1).

1536

1537 Heintzenberg, J., D. C. Covert, and R. Van Dingenen. "Size Distribution and
1538 Chemical Composition of Marine Aerosols: A Compilation and Review." *Tellus B:*
1539 *Chemical and Physical Meteorology* 52, no. 4 (2000): 1104.

1540 <https://doi.org/10.3402/tellusb.v52i4.17090>.

1541
1542
1543
1544
1545
1546
1547
1548
1549
1550
1551
1552
1553
1554
1555
1556
1557
1558
1559
1560
1561
1562
1563
1564
1565
1566
1567
1568
1569
1570
1571
1572
1573
1574
1575
1576
1577

Hines, C. O. "Internal Atmospheric Gravity Waves at Ionospheric Heights." *Canadian Journal of Physics* 38, no. 11 (1960): 1441 - 1481. <https://doi.org/10.1139/p60-150>.

Hueso, R., A. Sánchez-Lavega, G. Piccioni, et al. "Morphology and Dynamics of Venus Oxygen Airglow from Venus Express/Visible and Infrared Thermal Imaging Spectrometer Observations." *Journal of Geophysical Research: Planets* 113, no. E5 (2008). <https://doi.org/10.1029/2008je003081>.

Hueso, R., et al., JUICE-JANUS observations of Earth in preparation for the JANUS investigation of Jupiter's atmosphere. *Ann. Geophys.*, submitted to this issue.

Hurley, J., P.G.J. Irwin, A. Adriani, et al. "Analysis of Rosetta/VIRTIS Spectra of Earth Using Observations from ENVISAT/AATSR, TERRA/MODIS and ENVISAT/SCIAMACHY, and Radiative-Transfer Simulations." *Planetary and Space Science* 90 (January 2014): 37 - 59. <https://doi.org/10.1016/j.pss.2013.06.012>.

Kim, Young-Joon, Stephen D. Eckermann, and Hye-Yeong Chun. "An Overview of the Past, Present and Future of Gravity-wave Drag Parametrization for Numerical Climate and Weather Prediction Models." *Atmosphere-Ocean* 41, no. 1 (2003): 65 - 98. <https://doi.org/10.3137/ao.410105>.

Kitamura, Rei, Laurent Pilon, and Mirosław Jonasz. "Optical Constants of Silica Glass from Extreme Ultraviolet to Far Infrared at near Room Temperature." *Applied Optics* 46, no. 33 (2007): 8118. <https://doi.org/10.1364/ao.46.008118>.

Krisna, Trismono C., Manfred Wendisch, André Ehrlich, et al. "Comparing Airborne and Satellite Retrievals of Cloud Optical Thickness and Particle Effective Radius Using a Spectral Radiance Ratio Technique: Two Case Studies for Cirrus and Deep Convective Clouds." *Atmospheric Chemistry and Physics* 18, no. 7 (2018): 4439 - 4462. <https://doi.org/10.5194/acp-18-4439-2018>.

Kuang, Zhiming, Jack Margolis, Geoffrey Toon, David Crisp, and Yuk Yung. "Spaceborne Measurements of Atmospheric CO₂ by High-resolution NIR Spectrometry of Reflected Sunlight: An Introductory Study." *Geophysical Research Letters* 29, no. 15 (2002). <https://doi.org/10.1029/2001gl014298>.

1578 Kurucz, R.L., (1995), The solar irradiance by computation, Proc 17th Annual
1579 Conference Transmission Models, Phillips Laboratory, Hanscom AFB,
1580 PL-TR-95-2060. G.P. Anderson, et al. Eds. PP 333-334.
1581
1582 Kurucz, R.L., et al. (1984), Solar Flux atlas from 296 to 1300 nm, National Solar
1583 Observatory Atlas No. 1. NOAO, Sunspot, NM.
1584
1585 Khurana, K.K., et al., 2007. The origin of Ganymedes' polar caps. *Icarus*, 191, 1,
1586 193-202. <https://doi.org/10.1016/j.icarus.2007.04.022>
1587
1588 Langevin, Y., F. Poulet, G. Piccioni, et al. "Calibration of MAJIS (Moons and Jupiter
1589 Imaging Spectrometer). IV. Radiometric Calibration (Invited)." *Review of Scientific*
1590 *Instruments* 95, no. 11 (2024). <https://doi.org/10.1063/5.0202702>.
1591
1592 Langevin, Y., Rodriguez, S., Poulet, F., Guerlet, S., Armante, R., Agostini, L.,
1593 D'Aversa, E., Royer, C., Fletcher, L., Oliva, F., Seignovert, B., Stephan, K., and Tosi,
1594 F.: Post-launch spectral and radiometric performances of MAJIS, the VIS–NIR
1595 imaging spectrometer of JUICE, *Ann. Geophys.*, submitted to this issue.
1596
1597 LeMone, Margaret A. "International Cloud Atlas: Manual on the Observation of
1598 Clouds and Other Meteors." In *International Cloud Atlas*. World Meteorological
1599 Organization, 1988.
1600
1601 Ligier, N., C. Paranicas, J. Carter, et al. "Surface Composition and Properties of
1602 Ganymede: Updates from Ground-Based Observations with the near-Infrared
1603 Imaging Spectrometer SINFONI/VLT/ESO." *Icarus* 333 (November 2019): 496 - 515.
1604 <https://doi.org/10.1016/j.icarus.2019.06.013>.
1605
1606 ~~Ettore Lopinto, E., Luca Fasano, L., Francesco Longo, F., Giancarlo Varacalli, G.,~~
1607 ~~Patrizia Sacco, P., Leandro Chiarantini, L., Francesco Sarti, F., Luigi Agrimano, L.,~~
1608 ~~Francesca Santoro, F., Sergio Cogliati, S., Roberto Colombo, R., Mariano Bresciani,~~
1609 ~~M., Claudia Giardino, C., Federica Braga, F. (2021).~~ Current Status and Future
1610 Perspectives of the PRISMA Mission at the Turn of One Year in Operational Usage
1611 2021 IEEE International Geoscience and Remote Sensing Symposium IGARSS
1612 <https://doi.org/10.1109/IGARSS47720.2021.9553301>
1613

1614 Luo, Tao, Renmin Yuan, and Zhien Wang. "On Factors Controlling Marine Boundary
1615 Layer Aerosol Optical Depth." *Journal of Geophysical Research: Atmospheres* 119,
1616 no. 6 (2014): 3321 - 3334. <https://doi.org/10.1002/2013jd020936>.

1617

1618 Mastrapa, R, M Bernstein, S Sandford, T Roush, D Cruikshank, and C Ore. "Optical
1619 Constants of Amorphous and Crystalline H₂O Ice in the near Infrared from 1.1 to 2.6
1620 μm ." *Icarus* 197, no. 1 (2008): 307 - 320.
1621 <https://doi.org/10.1016/j.icarus.2008.04.008>.

1622

1623 Mastrapa, R. M., S. A. Sandford, T. L. Roush, D. P. Cruikshank, and C. M. Dalle Ore.
1624 "Optical Constant of Amorphous and Crystalline H₂O Ice: 2.5-22 Mm (4000-455
1625 Cm⁻¹) Optical Constants of H₂O Ice." *The Astrophysical Journal* 701, no. 2 (2009):
1626 1347 - 1356. <https://doi.org/10.1088/0004-637x/701/2/1347>.

1627

1628 Melin, H., O'Donoghue, J., Moore, L., Stallard, T. S., Fletcher, L. N., Roman, M. T.,
1629 Harkett, J., King, O. R. T., Thomas, E. M., Wang, R., Tiranti, P. I., Knowles, K. L., de
1630 Pater, I., Fouchet, T., Fry, P. H., Wong, M. H., Holler, B. J., Hueso, R., James, M. K.,
1631 ... Showalter, M. R. (2024). Ionospheric irregularities at Jupiter observed by JWST.
1632 *Nature Astronomy*, 8(8), 1000–1007. <https://doi.org/10.1038/s41550-024-02305-9>.

1633

1634 Migliorini, A., B. M. Dinelli, C. Castagnoli, et al. "First Observations of CH₄ and
1635 Spatially Resolved Emission Layers at Jupiter Equator, as Seen by JIRAM/Juno."
1636 *Journal of Geophysical Research: Planets* 128, no. 3 (2023).
1637 <https://doi.org/10.1029/2022je007509>.

1638

1639 Miller, Steve, Jonathan Tennyson, Thomas R. Geballe, and Tom Stallard. "Thirty
1640 Years of H₃⁺ Astronomy." *Reviews of Modern Physics* 92, no. 3 (2020).
1641 <https://doi.org/10.1103/revmodphys.92.035003>.

1642

1643 Moriconi, M. L., A. Migliorini, F. Altieri, et al. "Turbulence Power Spectra in Regions
1644 Surrounding Jupiter's South Polar Cyclones from Juno/JIRAM." *Journal of*
1645 *Geophysical Research: Planets* 125, no. 7 (2020).
1646 <https://doi.org/10.1029/2019je006096>.

1647

1648 Müller-Wodarg, I. C. F., T. T. Koskinen, L. Moore, et al. "Atmospheric Waves and

1649 Their Possible Effect on the Thermal Structure of Saturn's Thermosphere."
1650 *Geophysical Research Letters* 46, no. 5 (2019): 2372 - 2380.
1651 <https://doi.org/10.1029/2018gl081124>.
1652
1653 Nakajima, Takashi Y., Haruma Ishida, Takashi M. Nagao, et al. "Theoretical Basis of
1654 the Algorithms and Early Phase Results of the GCOM-C (Shikisai) SGLI Cloud
1655 Products." *Progress in Earth and Planetary Science* 6, no. 1 (2019).
1656 <https://doi.org/10.1186/s40645-019-0295-9>.
1657
1658 Nastrom, Gregory D., and David C. Fritts. "Sources of Mesoscale Variability of
1659 Gravity Waves. Part i: Topographic Excitation." *Journal of the Atmospheric Sciences*
1660 49, no. 2 (1992): 101 - 110.
1661 [https://doi.org/10.1175/1520-0469\(1992\)049<0101:somvog>2.0.co;2](https://doi.org/10.1175/1520-0469(1992)049<0101:somvog>2.0.co;2).
1662
1663 Newnham, David A., and John Ballard. "Visible Absorption Cross Sections and
1664 Integrated Absorption Intensities of Molecular Oxygen (O₂ and O₄)." *Journal of*
1665 *Geophysical Research: Atmospheres* 103, no. D22 (1998): 28801 - 28815.
1666 <https://doi.org/10.1029/98jd02799>.
1667
1668 O'Donoghue, J., L. Moore, T. S. Stallard, and H. Melin. "Heating of Jupiter's Upper
1669 Atmosphere above the Great Red Spot." *Nature* 536, no. 7615 (2016): 190 - 192.
1670 <https://doi.org/10.1038/nature18940>.
1671
1672 Oliva, F., A. Adriani, M.L. Moriconi, G.L. Liberti, E. D'Aversa, and G. Filacchione.
1673 "Clouds and Hazes Vertical Structure of a Saturn's Giant Vortex from Cassini/VIMS-V
1674 Data Analysis." *Icarus* 278 (November 2016): 215 - 237.
1675 <https://doi.org/10.1016/j.icarus.2016.06.021>.
1676
1677 Oliva, F., A. Geminale, E. D'Aversa, et al. "Properties of a Martian Local Dust Storm
1678 in Atlantis Chaos from OMEGA/MEX Data." *Icarus* 300 (January 2018): 1 - 11.
1679 <https://doi.org/10.1016/j.icarus.2017.07.034>.
1680
1681 Oliva, F., G. Piccioni, E. D'Aversa, et al. "Earth as an Exoplanet: VIRTIS-M/Venus
1682 Express Data Analysis." *EPSC Abstracts* 11 (2017).
1683
1684 Orton, G.S., et al., 2017. The first close-up images of Jupiter's polar regions: Results
1685 from the Juno mission JunoCam instrument. *Geophysical Research Letters*, 44, 10,

1686 4599-4606.

1687

1688 Peralta, J., R. Hueso, A. Sánchez-Lavega, G. Piccioni, O. Lanciano, and P. Drossart.

1689 “Characterization of Mesoscale Gravity Waves in the Upper and Lower Clouds of

1690 Venus from VEX-VIRTIS Images.” *Journal of Geophysical Research: Planets* 113, no.

1691 E5 (2008). <https://doi.org/10.1029/2008je003185>.

1692

1693 Piani, C., D. Durran, M. J. Alexander, and J. R. Holton. “A Numerical Study of

1694 Three-Dimensional Gravity Waves Triggered by Deep Tropical Convection and Their

1695 Role in the Dynamics of the QBO.” *Journal of the Atmospheric Sciences* 57, no. 22

1696 (2000): 3689 - 3702.

1697 [https://doi.org/10.1175/1520-0469\(2000\)057<3689:ansotd>2.0.co;2](https://doi.org/10.1175/1520-0469(2000)057<3689:ansotd>2.0.co;2).

1698

1699 Piccioni, Giuseppe, Alessandro Bini, Giulio Bugetti, et al. “Scientific Goals and

1700 Technical Challenges of the MAJIS Imaging Spectrometer for the JUICE Mission.”

1701 *2019 IEEE 5th International Workshop on Metrology for AeroSpace*

1702 (*MetroAeroSpace*), IEEE, June 2019, 318 - 323.

1703 <https://doi.org/10.1109/metroaerospace.2019.8869566>.

1704

1705 S. Pignatti *et al.*, “The PRISMA hyperspectral mission: Science activities and

1706 opportunities for agriculture and land monitoring,” *2013 IEEE International*

1707 *Geoscience and Remote Sensing Symposium - IGARSS*, Melbourne, VIC, Australia,

1708 2013, pp. 4558-4561, doi: 10.1109/IGARSS.2013.6723850.

1709

1710 Poulet, F., G. Piccioni, Y. Langevin, et al. “Moons and Jupiter Imaging Spectrometer

1711 (MAJIS) on Jupiter Icy Moons Explorer (JUICE).” *Space Science Reviews* 220, no. 3

1712 (2024a). <https://doi.org/10.1007/s11214-024-01057-2>.

1713

1714 Poulet, F., Piccioni, G., Langevin, Y., et al. ESA/JUICE encounters Earth/Moon in

1715 2024: overview of the Moons And Jupiter Imaging Spectrometer (MAJIS)

1716 observations. *Ann. Geophys.*, submitted to this issue

1717

1718 Poulet, F., Langevin, Y., and Piccioni, G.: Calibration of the Moons And Jupiter

1719 Imaging Spectrometer (MAJIS): Introduction to the special collection and summary of

1720 the performances, *Rev. Sci. Instrum.*, 95, 071601, <https://doi.org/10.1063/5.0209679>,

1721 2024b

1722

1723 Rossow, William B., and Robert A. Schiffer. "Advances in Understanding Clouds from
1724 ISCCP." *Bulletin of the American Meteorological Society* 80, no. 11 (1999): 2261 -
1725 2287. [https://doi.org/10.1175/1520-0477\(1999\)080<2261:aiucfi>2.0.co;2](https://doi.org/10.1175/1520-0477(1999)080<2261:aiucfi>2.0.co;2).
1726

1727 Seignovert, B., Poulet, F., Langevin, Y., D'Aversa, E., Ligier, N., Mesbout, M., Leyrat,
1728 C., Le Mouélic, S., Stephan, K., Palumbo, P., Agostini, L., Pensa, L., Le Deit, L.,
1729 Cornet, T., Belgacem, I., Costa, M., and Escalante Lopez, A.: MAJIS onboard
1730 geometric calibration during 1320 the early cruise phase, *Ann. Geophys.*, submitted
1731 to this issue.

1732

1733 Serdyuchenko, A., Gorshelev, V., Weber, M., Chehade, W., and Burrows, J. P.: High
1734 spectral resolution ozone absorption cross-sections – Part 2: Temperature
1735 dependence, *Atmos. Meas. Tech.*, 7, 625–636,
1736 <https://doi.org/10.5194/amt-7-625-2014>, 2014.

1737

1738 Simon, A. A., L. Li, and D. C. Reuter. "Small-scale Waves on Jupiter: A Reanalysis of
1739 New Horizons, Voyager, and Galileo Data." *Geophysical Research Letters* 42, no. 8
1740 (2015): 2612 - 2618. <https://doi.org/10.1002/2015gl063433>.

1741

1742 Sindoni, G., D. Grassi, A. Adriani, et al. "Characterization of the White Ovals on
1743 Jupiter's Southern Hemisphere Using the First Data by the Juno/JIRAM Instrument."
1744 *Geophysical Research Letters* 44, no. 10 (2017): 4660 - 4668.
1745 <https://doi.org/10.1002/2017gl072940>.

1746

1747 Smirnov, Alexander, Brent N. Holben, Yoram J. Kaufman, et al. "Optical Properties of
1748 Atmospheric Aerosol in Maritime Environments." *Journal of the Atmospheric*
1749 *Sciences* 59, no. 3 (2002): 501 - 523.
1750 [https://doi.org/10.1175/1520-0469\(2002\)059<0501:opoaai>2.0.co;2](https://doi.org/10.1175/1520-0469(2002)059<0501:opoaai>2.0.co;2).

1751

1752 Smith, K.M, and D.A Newnham. "Near-Infrared Absorption Spectroscopy of Oxygen
1753 and Nitrogen Gas Mixtures." *Chemical Physics Letters* 308, nos. 1–2 (1999): 1 - 6.
1754 [https://doi.org/10.1016/s0009-2614\(99\)00584-9](https://doi.org/10.1016/s0009-2614(99)00584-9).

1755

1756 Stephan, Katrin, Mauro Ciarniello, Olivier Poch, Bernard Schmitt, David Haack, and
1757 Andrea Raponi. "VIS-NIR/SWIR Spectral Properties of H₂O Ice Depending on
1758 Particle Size and Surface Temperature." *Minerals* 11, no. 12 (2021): 1328.
1759 <https://doi.org/10.3390/min11121328>.

1760
1761 Stephan, Katrin, T. Roatsch, F. Tosi, et al. "Regions of Interest on Ganymede's and
1762 Callisto's Surfaces as Potential Targets for ESA's JUICE Mission." *Planetary and*
1763 *Space Science* 208 (November 2021a): 105324.
1764 <https://doi.org/10.1016/j.pss.2021.105324>.
1765
1766 Stevens, Michael H., Christoph R. Englert, John M. Harlander, et al. "Retrieval of
1767 Lower Thermospheric Temperatures from O2 A Band Emission: The MIGHTI
1768 Experiment on ICON." *Space Science Reviews* 214, no. 1 (2017).
1769 <https://doi.org/10.1007/s11214-017-0434-9>.
1770
1771 Sun, Kangwen, Guangyao Dai, Songhua Wu, et al. *Correlation between Marine*
1772 *Aerosol Optical Properties and Wind Fields over Remote Oceans with Use of*
1773 *Spaceborne Lidar Observations*. Copernicus GmbH, 2023.
1774 <https://doi.org/10.5194/egusphere-2023-433>.
1775
1776 Taylor, M.J., and M.A. Hapgood. "Identification of a Thunderstorm as a Source of
1777 Short Period Gravity Waves in the Upper Atmospheric Nightglow Emissions."
1778 *Planetary and Space Science* 36, no. 10 (1988): 975 - 985.
1779 [https://doi.org/10.1016/0032-0633\(88\)90035-9](https://doi.org/10.1016/0032-0633(88)90035-9).
1780
1781 Thomason, L. W., S. P. Burton, B.-P. Luo, and T. Peter. "SAGE II Measurements of
1782 Stratospheric Aerosol Properties at Non-Volcanic Levels." *Atmospheric Chemistry*
1783 *and Physics* 8, no. 4 (2008): 983 - 995. <https://doi.org/10.5194/acp-8-983-2008>.
1784
1785 Tosi, Federico, Thomas Roatsch, André Galli, et al. "Characterization of the Surfaces
1786 and Near-Surface Atmospheres of Ganymede, Europa and Callisto by JUICE."
1787 *Space Science Reviews* 220, no. 5 (2024).
1788 <https://doi.org/10.1007/s11214-024-01089-8>.
1789
1790 van Diedenhoven, Bastiaan, Ann M. Fridlind, Brian Cairns, Andrew S. Ackerman, and
1791 John E. Yorks. "Vertical Variation of Ice Particle Size in Convective Cloud Tops."
1792 *Geophysical Research Letters* 43, no. 9 (2016): 4586 - 4593.
1793 <https://doi.org/10.1002/2016gl068548>.
1794
1795 Veefkind, J.P., I. Aben, K. McMullan, et al. "TROPOMI on the ESA Sentinel-5
1796 Precursor: A GMES Mission for Global Observations of the Atmospheric Composition

1797 for Climate, Air Quality and Ozone Layer Applications.” *Remote Sensing of*
1798 *Environment* 120 (May 2012): 70 - 83. <https://doi.org/10.1016/j.rse.2011.09.027>.
1799

1800 Voudouri, Kalliopi Artemis, Konstantinos Michailidis, Maria-Elissavet Koukouli, et al.
1801 “Investigating a Persistent Stratospheric Aerosol Layer Observed over Southern
1802 Europe during 2019.” *Remote Sensing* 15, no. 22 (2023): 5394.
1803 <https://doi.org/10.3390/rs15225394>.
1804

1805 Warren, Stephen G., and Richard E. Brandt. “Optical Constants of Ice from the
1806 Ultraviolet to the Microwave: A Revised Compilation.” *Journal of Geophysical*
1807 *Research: Atmospheres* 113, no. D14 (2008). <https://doi.org/10.1029/2007jd009744>.
1808

1809 Wei, Lesi, Huazhe Shang, Jian Xu, et al. “Cloud Top Pressure Retrieval Using
1810 Polarized and Oxygen A-Band Measurements from GF5 and PARASOL Satellites.”
1811 *Advances in Atmospheric Sciences* 41, no. 4 (2024): 680 - 700.
1812 <https://doi.org/10.1007/s00376-023-2382-5>.
1813

1814 Zheng, Guangjie, Yang Wang, Allison C. Aiken, et al. “Marine Boundary Layer
1815 Aerosol in the Eastern North Atlantic: Seasonal Variations and Key Controlling
1816 Processes.” *Atmospheric Chemistry and Physics* 18, no. 23 (2018): 17615 - 17635.
1817 <https://doi.org/10.5194/acp-18-17615-2018>.
1818

1819 Zhou, Yongbo, Xuejin Sun, Tero Mielonen, et al. “Cirrus Cloud Optical Thickness and
1820 Effective Diameter Retrieved by MODIS: Impacts of Single Habit Assumption, 3-d
1821 Radiative Effects, and Cloud Inhomogeneity.” *Journal of Geophysical Research:*
1822 *Atmospheres* 123, no. 2 (2018): 1195 - 1210. <https://doi.org/10.1002/2017jd027232>.
1823

1824 Zinner, T., Hausmann, P., Ewald, F., Bugliaro, L., Emde, C., Mayer, B.,
1825 “Ground-based imaging remote sensing of ice clouds: uncertainties caused by
1826 sensor, method and atmosphere.” *Atmospheric Measurements Techniques*, Volume
1827 9, issue 9, 4615–4632, (2016) <https://doi.org/10.5194/amt-9-4615-2016>
1828